Dissertation

submitted to the

Combined Faculty for Natural Sciences and for Mathematics

of the Ruperto Carola University of Heidelberg, Germany

for the degree of

Doctor of Natural Sciences

Presented by

M.Sc. (Molecular Biomedicine) Jingjing Shi

Born in: Henan, China

Oral examination: 19.03.2021

Identification of a functional Tie-Wnt signalling circuit controlling liver homeostasis and regeneration

Referees:

Prof. Dr. Ursula Klingmüller

Prof. Dr. Hellmut G. Augustin

Die vorliegende Arbeit wurde in der Abteilung „Vaskuläre Onkologie und Metastasierung“ am Deutschen Krebsforschungszentrum (DKFZ) in Heidelberg zwischen Mai 2015 und Dezember 2020 durchgeführt.

ACKNOWLEDGEMENT

Life is like a video game in which one keeps fighting with the monsters and overcoming obstacles. One might fall and has to start all over again but will also collect many treasures and gain strength. Getting the PhD is definitely not an easy one and without the people that helped and supported me towards my aim, the completion of this dissertation would not have been possible.

First of all, I would like to thank my supervisor, **Prof. Dr. Hellmut G. Augustin**, for giving me the opportunity to work on this exciting project. There have been so many ups and downs and you have always been patient and supportive, giving me the chance to explore and grow. Thanks so much for your patience and your guidance though this tough journey.

Furthermore, I would like to thank **Prof. Dr. Ursula Klingmüller** for giving me the opportunity to accomplish my doctoral thesis at the combined faculty of Natural Sciences and Mathematics of the Ruperto Carola University of Heidelberg and the German Cancer Research Centre. Thanks for being part of my Thesis Advisory Committee as well as the Doctoral Defence Examination Commission. Together with **Prof. Junhao Hu**, my external TAC member, you gave great feedback and suggestions during the past years. Many thanks to **Prof. Dr. Michael Boutros** for providing technical support, scientific feedback to the project and for chairing my doctoral examination. I would like to thank also **Dr. Haikun Liu** for being a role model for many young Chinese scientists and for taking part in my defence committee as an examiner.

I am thankful to the Helmholtz International Graduate School for Cancer Research for supporting me through my PhD research at the DKFZ. I would like to thank for the great support provided by all the facilities at DKFZ: The Protein Analysis Unit and the High Throughput Sequencing Unit of the Genomics and Proteomics Core Facility, the Flow Cytometry Core Facility, the Light Microscopy Core Facility, and the Laboratory Animal Facility. A sincere thanks to my external collaborators, **Shani Ben-Moshe** and **Dr. Shalev Itzkovitz** from the Weizmann Institute, **Dr. Renata Blatnik** and **Dr. Thomas Ruppert** from ZMBH, **Marziyeh Komeili** and **Prof. Dr. Christine Schaeffer** for your great support.

Many thanks to **Ki**, **Moritz** and **Guanxiong** for your great help with experiments. You were always there to help no matter day or night, working days or weekends. Thanks to **Ashik** and **Mahak** who were so caring and understanding, being like family to me. And thanks to **Nico** and **Moritz** for correcting my thesis. Thanks also to **Maria Riedel** and **Carleen Spegg** for the technical support throughout the project, and to **Petra, Anja, Ines, Maike, Daniela** and **Barbara** for administrative support.

Some special words go to my lab mate **Donato**, the special one. It is hard to define what you are to me: mentor, friend and foe, brother (both older and younger)… Life with you is tough but never boring. You are the one who always challenged me and pushed me to the limits. You are also the one that always has a solution and I know I can rely on. I learned the most from you and I hope you are also proud of me.

The whole A190 team is a big family to me, always welcoming and caring. Everyone, old and new members, makes the team wonderful. Through the scientific discussions, your technical support, or personal suggestions, everyone has contributed in one way or another to the project and to make me a better scientist. Moreover, life outside the lab would be so boring without you. The happiness and sadness, the fear and relief, the frictions and understanding, every moment we shared is a colourful piece of memory: The skiing vacation in Innsbruck, the Bachelor party in Copenhagen, the Indian adventure, the girls' trip to Hamburg, also lab retreats, breakfast brunches, birthday parties and millions of other events. A heartful thanks to all of you that accompanied me through the journey: **Laura, Anja R, Silvia, Eva G, Stephanie K, Janina, Elisa, Tina, Courtney, Lise, Claudia, Beate, Paula, Stephanie P, Stephanie G, Xiaowen, Miki, Cata, Dennis, Anja G, Shub, Donato, Ashik, Mahak, Nico, Ki, Moritz, Guanxiong, Dimi, Kshitij, Martin T, Martin A, Martin P, Maria, Carleen, Benni, Celine, Eva B, Claudine, Jessy, Stella …**

Thanks to all my friends who have been with me through all the years. We are not always in contact but I know you will always be there for me. Thanks for cheering me up during my frustrations. Thanks for understanding my sadness. Thanks for inspiring me when I was feeling lost. You are the sunshine of the dark days. **Xianjin, Liang Yuan, Yudong, Ruifan, Jinhui, Qi, Pingping, Junlin, Sakeena, Eilin, Guanghua, Bosen, Bingyuan…** Thanks!

The biggest thanks go to my family, who are ever so supportive and understanding. I know that you hide your worries and concerns and give me the freedom to explore. But you will always back me up when I needed. You always gave me more than what I asked. You are the source of my motivation and I hope you are always proud of me! **谢谢爸爸妈妈和弟弟，爷爷奶奶，姑姑姑父！谢谢你们一直以来无条件的支持和理解，在我需要的时候你们都在。你们总是把担忧放在心里，处处站在我的角度为我着想，希望我能少些后顾之忧。你们希望我飞得高，同时又担心我飞的累。谢谢你们无时无刻的付出，我爱你们！**

TABLE OF CONTENTS

LIST OF FIGURES

LIST OF TABLES

ZUSAMMENFASSUNG

Einzelzell-Transkriptomanalysen (scRNAseq) von Hepatozyten und Leberendothelzellen (L-EC) haben das Verständnis der räumlichen Architektur der Leberstruktur und -funktion revolutioniert (Halpern et al., 2018; Halpern et al., 2017). Die räumliche Ausrichtung von L-EC und Hepatozyten ist für die Leberfunktion in Bezug auf Gesundheit und Krankheit entscheidend, da L-EC eine instruktive Gatekeeper-Funktion für benachbarte Hepatozyten haben (Ding et al., 2010; Hu et al., 2014; Koch et al., 2017; Lorenz et al., 2018), zum Beispiel bei der Wnt-abhängigen Aufrechterhaltung der metabolischen Zonierung (Rocha et al., 2015; Wang et al., 2015). Die Weiterentwicklung der Leberbiologie über die „Transkript-zentrische“ Sichtweise von scRNAseq-Analysen hinaus wird derzeit durch die begrenzte Auflösung von Proteomik und genomweiten Techniken zur Analyse posttranslationaler Modifikationen eingeschränkt (Marx, 2019; Needham et al., 2019). Durch die Kombination einer räumlichen Zellsortierungsmethode mit Transkriptom- und quantitativen Proteom-/ Phosphoproteom-Analysen, wurde das Expressionsmuster von Leberendothelzellen funktionell und räumlich aufgelöst und einen mechanistischen Einblick in die Zonierung von vaskulären Signalmechanismen geliefert. Die Phosphorylierung von Rezeptortyrosin Kinasen (RTK) wurde bevorzugt im Bereich der Zentralvene nachgewiesen, was durch eine atypischen Anreicherung von Tyrosin-Phosphorylierungen gekennzeichnet war. Prototypisch konnte der Phosphorylierungsgradient der vaskulären RTK Tie1 durch Antikörperblockade validiert werden. Tie1-Blockade führte hierbei zu einer schnellen perizentralen Dysregulation des L-EC-Transkriptoms. Insbesondere konnte eine Tie1-abhängige Expression von Wnt9b in L-EC identifiziert werden sowie eine reziproke Regulation durch FoxO1- und STAT3-Transkriptionsfaktoren. Die Antikörper-vermittelte oder genetische Inaktivierung von Tie1 in L-EC führte zu einer verringerten Leberregeneration nach partieller Hepatektomie (Leberteilresektion), was mit einer reduzierten Wnt-Ligand- und Wnt-Zielgen-Expression (z.B. von Axin2, Sox9, Tbx3 und Lgr5) einherging. Zusammengenommen hat die Studie beispiellose Einblicke in die räumliche Organisation der L-EC-Signalübertragung geliefert und eine vaskuläre Tie1-Wnt-Signalachse als Regulator der Leberfunktion entdeckt. Die angewandte räumliche Sortiertechnik, gefolgt von einer Phosphoproteomanalyse, kann als universell anpassbare Strategie für die räumliche Phosphoproteomanalyse von scRNAseq-definierten relevanten zellulären (Sub-) Populationen eingesetzt werden.

SUMMARY

Single cell RNA sequencing (scRNAseq) analyses of hepatocytes and liver endothelial cells (L-EC) have revolutionized the understanding of the spatial architecture of liver structure and function (Halpern et al., 2018; Halpern et al., 2017). The spatial alignment of L-EC and hepatocytes is pivotal for liver function in health and disease given that L-EC act as instructive gatekeeper of nearby hepatocytes (Ding et al., 2010; Hu et al., 2014; Koch et al., 2017; Lorenz et al., 2018) including the maintenance of liver metabolic zonation in a Wnt-dependent manner(Rocha et al., 2015; Wang et al., 2015). Advancing liver biology beyond the 'transcript-centric' view of scRNAseq analyses is presently restricted by the limited resolution of proteomics and genome-wide techniques to analyse post-translational modifications (Marx, 2019; Needham et al., 2019). By combining spatial cell sorting methodology with transcriptomic and quantitative proteomic/phosphoproteomic analyses, the first functionally and spatially-resolved proteome landscape of the liver endothelium was presented in this study, yielding deep mechanistic insight into zonated vascular signalling mechanisms. Phosphorylation of receptor tyrosine kinases (RTK) was detected preferentially in the central vein area resulting in an atypical enrichment of tyrosine phosphorylation. Prototypic biological validation of the identified strong phosphorylation gradient of the vascular RTK Tie1 by antibody blockade resulted in the rapid peri-central dysregulation of the L-EC transcriptome. Notably, the expression of Wnt9b in L-EC was discovered as Tie receptor controlled with reciprocal regulation by FoxO1 and STAT3 transcription factors. Genetic inactivation of Tie1 in L-EC or antibody blockade resulted in reduced liver regeneration following partial hepatectomy with reduced Wnt ligand and Wnt target gene expression, including *Axin2*, *Sox9*, *Tbx3* and *Lgr5*. Taken together, the study has yielded unparalleled insight into the spatial organization of L-EC signalling and discovered a vascular Tie-Wnt signalling axis as regulator of liver function. The employed spatial sorting technique followed by phosphoproteomic analysis may be employed as a universally adaptable strategy for the spatial phosphoproteomic analysis of scRNAseq-defined relevant cellular (sub)-populations.

1. INTRODUCTION

1.1 General features of the liver

The liver is the metabolic centre of the body that maintains the physiological homeostasis and performs diverse functions including the modulation of glucose levels, detoxification of xenobiotics, immunological surveillance of pathogens, metabolism of lipids, and biosynthesis of plasma proteins and hormones. Most of these functions are performed by the parenchymal cells – hepatocytes, with the support of the non-parenchymal cells (NPCs) including liver endothelial cells (L-ECs), hepatic stellate cells (HSCs), cholangiocytes, Kupffer cells and additional immune cells (Gebhardt, 1992). To best coordinate the function of the liver, these cells are architecturally organized in the fundamental structural unit – the liver lobule (Figure 1). Lobules are hexagonal shaped columns with portal nodes at the corners and the central vein in the middle. The liver receives a unique dual blood supply. Oxygenated blood enters through the hepatic artery and blood from the gut, rich in nutrients and bacterial endotoxin, enters through the hepatic portal vein. Blood enters the lobules from the portal nodes, merges into the liver sinusoids, and flows towards the draining central vein. Hepatocytes are arranged in anastomosing cell plates of single cell thickness which span the porto-venous axis along the sinusoids. Bile acids secreted by hepatocytes are transported by the bile canaliculi in the opposite direction to the blood flow (Ben-Moshe and Itzkovitz, 2019; Valle-Encinas and Dale, 2020).

1.1.1 Development of the liver

Liver diverticulum formation and budding is a highly conserved process in vertebrates. Hepatic specification starts in mice at embryonic day E8.25, and by E8.75 the liver diverticulum starts to form through thickening of the ventral domain of the foregut and septum transversum. Endothelial cells (ECs) which are essential for liver budding, are already found at this stage in the surrounding of the thickened hepatic endoderm. At E9.0, the hepatic endoderm forms a pseudostratified epithelium called hepatoblasts, which express marker genes like alpha-fetoprotein (AFP) and albumin (ALB). Subsequently, hepatoblasts delaminate, proliferate and migrate into the septum transversum to the form the liver bud. Additionally, hematopoietic progenitors also start to migrate into the liver bud at this stage to establish the fetal haematopoiesis (Gordillo et al., 2015).

Hepatoblasts are epithelial progenitor cells of the liver that will differentiate into hepatocytes and cholangiocytes starting at E13.5. Hepatoblasts located away from the portal area differentiate into hepatocytes and a monolayer of hepatoblasts surrounding the portal vein forms the ductal plate, which are the cholangiocytes precursors. These cells have higher expression of CK19 than their neighbouring cells and progress into a bilayer. Later, CK19 expression becomes restricted to cholangiocytes that will eventually form tubules at E17.5 in mice (Gordillo et al., 2015).

Formation of the complex liver vasculature network accompanies liver parenchymal development. At early embryonic stage E9.5, before the formation of functional blood vessels, endothelial cells have been shown to promote the outgrowth of hepatic progenitors from the liver bud. The hepatic vasculature forms

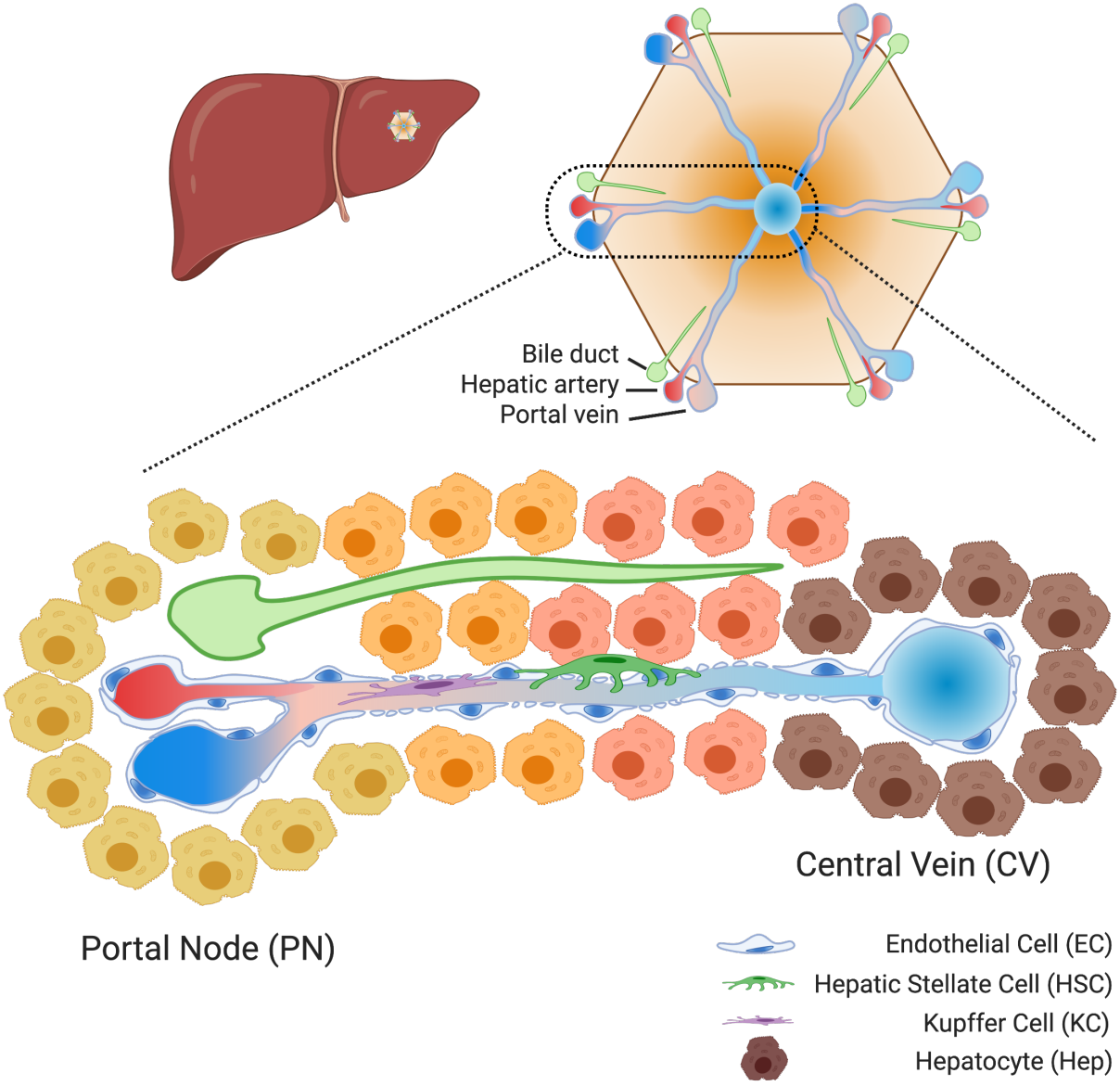

Figure 1. Structure of the liver lobule. The lobules are hexagonal shaped columns, with the portal nodes at the corners and central vein in the middle. The liver receives a unique dual blood supply from hepatic artery and portal vein. The blood enters the lobules from the portal nodes, merges into the liver sinusoids, and flows towards the draining central vein. The hepatocytes (light to dark brown) are arranged in anastomosing cell plates. The bile acids secreted by the hepatocytes are transported by the bile canaliculi in the opposite direction to the blood flow. Hepatic stellate cells (HSC, dark green) are the liver pericytes that covered the vessel. The Kupffer cells (KC, purple) are hepatic macrophages that located inner the vessels. Graphic created with Biorender.com.

through both, angiogenesis and vasculogenesis. One of the major fetal venous systems, namely vitelline veins, is involved in the formation of the efferent venous system. By contrast, the umbilical vein is the major afferent vessel of the liver, which will collapse and disappear after birth, and will be replaced by the portal veins. The hepatic artery system formation starts later and is initiated along the intrahepatic portal vein and expands to the periphery (Si-Tayeb et al., 2010).

1.1.2 Hepatocyte zonation

Between gestation days E9.5 and E15, the primary function of the fetal liver is haematopoiesis. Starting from E13, hepatoblasts start to differentiate and mature, which continues through birth and the liver gradually acquires its metabolizing capacity during this process (Moscovitz and Aleksunes, 2013). The functions of the liver are not performed uniformly along the lobule radial axis, mainly due to its unique vasculature system. In adult liver, around 75% of the afferent blood drains from the intestine, mixed with only 25% highly oxygenated arterial blood, generating a rather a hypoxic environment in the liver. As hepatocytes respire, the oxygen concentration further decreases along the sinusoid towards the central vein. Indeed, peri-portal hepatocytes were found to have more and larger mitochondria in comparison to peri-central hepatocytes. Thus, many energetically demanding tasks, including the continuous translation of secreted proteins, glyconeogenesis, β-oxidation of fatty acids, cholesterol biosynthesis, amino acid breakdown and ureogenesis, are performed by peri-portal hepatocytes. In contrast, glycolysis, liponeogenesis, ketogenesis, alcohol detoxification, bile acid synthesis and glutamine synthesis are performed by peri-central hepatocytes (Gebhardt, 1992).

In addition to the polarized division of metabolic processes, transcriptome analysis of hepatocytes on the single-cell level hinted on spatially distributed metabolic cascades that work in a production line pattern, where the intermediate metabolites are transferred from upstream cell layers to the next downstream layer, for example in case of the neutral bile acid biosynthesis cascade and the secretion of insulin growth factors. Furthermore, metabolites produced by peri-portal hepatocytes, such as glucose and glutamate, can be recycled within the liver by peri-central hepatocytes. Taken together, the functional zonation of hepatocytes does not only represent the spatial distribution of labour, but is a highly intercalated, orchestrated organization to meet the metabolic demand of the body.

1.2 The development of vascular system

The vascular system carries oxygen, nutrients, hormones, as well as immune cells and other molecules to all tissues of the body. Reflecting the limited diffusion distance of oxygen in tissues, almost every cell is within 100-150 μm of the nearest capillary with few exceptions like in the cartilage. Therefore, the vascular system can be viewed as a disseminated organ with a large surface area (Augustin and Koh, 2017). The vascular network is spatially organized in a hierarchical fashion that is necessary to deliver adequate nutrients to the tissues and the vascular wall is composed of endothelial cells (EC) and mural cells, embedded in the extracellular matrix (ECM) (Jain, 2003). The blood vessels and the heart are the first

organs to form and function during development in mammals and the vasculature continues to remodel as the organs function. The vasculature forms by both, vasculogenesis – the *de novo* vessel formation from angioblasts or stem cells, and angiogenesis – sprouting, bridging and intussusceptive growth from existing vessels, which involves the following timely overlapping processes: vessel formation, stabilization, branching, remodelling and pruning (Jain, 2003). ECs can originate from hemangioblasts that are present in various organs during embryonic development, from bone marrow-derived stem cells or from pre-existing resident ECs in the organs. Similarly, mural cells originate from multiple sources, including the local and distal mesenchyme (Jain, 2003; Singhal et al., 2020). Common progenitors can differentiate into ECs or mural cells depending on the presence of different growth factors, and ECs can also transdifferentiate into mural cells under certain circumstances (Jain, 2003).

1.2.1 The formation of blood vessels

Sprouting angiogenesis is facilized by hypoxia, which leads to the upregulation of genes involved in vessel formation, patterning and maturation. Among the molecular and cellular events involved in the vessel formation process, vascular endothelial growth factor (VEGF) signalling represents a key driver. VEGF-A is induced by hypoxia and is the prototypic member of this ligand family including VEGF-B, VEGF-C, VEGF-D, and placenta growth factor (PlGF) (Jain, 2003). Several isoforms of VEGF-A are generated through alternative splicing or proteolytic processing and have different heparin binding affinities for heparan sulfate proteoglycans (HPSGs) in the ECM. The diffusible and HSPG-bound VEGF-A thus forms a gradient that induces migration of tip cell and the proliferation of neighbouring stalk cells. In addition, VEGF-A also induces the expression of delta-like ligand 4 (DLL-4) in tip cells, which activates Notch receptors in neighbouring stalk cells, leading to the downregulation of VEGFR-2 expression in these cells, which in turn serves as a dampening mechanism to prevent excess angiogenesis (Chung and Ferrara, 2011). Other fine-tuning mechanisms include the expression of Jagged-1, antagonizing Dll4-Notch signalling in stalk cells to maintain the tip cell responsiveness to VEGF-A, as well as the stalk cell expression of VEGFR-1, which is a decoy ligand that neutralizes VEGF-A. Hypoxia also induces the expression of nitric oxide synthase and angiopoietin-2 (Angpt2), both facilitating the VEGF-A signalling. Nitric oxide, the product of nitric oxide synthase, leads to vessel dilation and leakiness in response to VEGF. Angpt2, a context-dependent ligand of Tie2 receptor, facilitates sprout formation in the presence of VEGF (Chung and Ferrara, 2011; Jain, 2003).

1.2.2 Arterial-venous specification

The formation of a hierarchical tree with specific inflow/outflow compartments is a prerequisite to a functional vascular network. Vessels are specified into arteries, capillaries, veins and lymphatics as they develop, which involves a large set of transcription factors (TF), for instance, ETS domain–binding factor (ETS), GATA-binding factor (GATA), Krüppel-like factor (KLF), Homeobox (HOX), sex-determining region Y box (SOX), and Forkhead box (FOX) families of transcription factors (Niklason and Dai, 2018).

Signalling pathways involved in arterial specification are quite well studied. Among these, the Notch pathway is indispensable. Notch signalling is a highly conserved pathway present in most spieces which requires direct contact of neighbouring cells as both receptors and ligands are transmembrane proteins. In vertebrates, there are four Notch receptors (Notch 1-4) and five ligands (Jagged-1, Jagged-2, DLL-1, DLL-3, and DLL-4). Ligand binding triggers the cleavage of the Notch receptors and the Notch intracellular domain (NICD) goes into the nucleus and promotes downstream gene expression of arterial specific transcription factors such as *Hes1, Hes2, Hey1* and *Hey2* (Niklason and Dai, 2018). Several other signalling pathways crosstalk with Notch signalling, including VEGF signalling, which activates the phosphatidylinositol 3-kinase (PI3K)/Akt pathway and the extracellular signal regulated kinase/mitogen-activated protein kinase (ERK/MAPK) pathway. It has been shown that strong stimulation of ERK signalling promotes arterial differentiation, whereas activation of the PI3K/Akt pathway facilitates venous differentiation. In addition, several core transcriptional programs are essential to the cell fate determination, such as the SoxF family of transcription factors, Sox7, Sox17 and Sox18 (Niklason and Dai, 2018).

In contrast to arterial specification, vein formation is much less well understood. It was initially thought that the venous cell fate is default if Notch signalling is not activated until the discovery of COUP-TFII. In the absence of COUP-TFII, arterial markers appear in the venous circulation, indicating that the venous identity is dependent on the activation of COUP-TFII. In addition, COUP-TFII could also inhibit the expression of Nrp1 and Foxc1, upstream regulators of Notch, thus suppressing the Notch activation, supporting the notion of default venous fate. Upstream regulators of COUP-TFII are less known. Angpt1/Tie2 activation and epigenetic regulations are among the few identified factors (Niklason and Dai, 2018).

1.2.3 Lymphatic specification

In addition to the blood vasculature, the lymphatic system is the other major circulatory system that is composed of a blind-ended network of vessels. It plays important roles in the maintenance of tissue fluid homeostasis, fat metabolism and immune surveillance (Semo et al., 2016). The embryonic development of the lymphatic system occurs after the blood system, with the earliest specification of endothelial cells to lymphatic lineage at mouse embryonic day (E) 9.5. The prevalent view for the venous origin of lymphatic endothelial cells can be traced back to more than 100 years ago postulated by Sabin (Sabin, 1902). The earliest transcription factor involved in the lymphatic specification is probably SOX18, which in cooperation with the venous marker COUP-TFII, activates the expression of PROX1 in the endothelial cells of the cardinal veins. PROX1 is the key transcription factor for lymphatic differentiation as well as the maintenance of their identity (Jha et al., 2018). It is specifically expressed in a subpopulation of ECs around E9.5 and the PROX1-positive ECs later bud off to give rise to primitive lymph sacs (Semo et al., 2016).

Another crucial pathway involved in lymphatic development is VEGF signalling. Instead of VEGF-A/VEGFR2 in blood vessels, the VEGF-C/VEGFR3 axis is the major player here, which stimulates the migration of lymphatic endothelial cells out of the veins (Potente and Makinen, 2017). Early developing blood vessels also express significant levels of VEGFR3, which declines during the period of lymphatic budding. With a few exceptions, the expression of VEGFR3 is restricted to lymphatic vessels in adulthood (Semo et al., 2016). In addition to its role in arterial specification of blood vessels, Notch signalling has also been shown to negatively regulate lymphangiogenesis. Activation of Notch1 by Jagged1 represses the COUP-TFII/PROX1 axis, which helps to maintain venous identity (Semo et al., 2016). Not surprisingly, BMP and Wnt signalling that are involved in many differentiation processes during embryogenesis, have also been shown to be involved in lymphatic cell fate determination (Semo et al., 2016).

1.2.4 Vessel maturation

Although much less investigated, the maturation of the nascent vasculature is as important as the sprouting of new vessels. Vessel maturation includes, among other processes, recruitment of mural cells, generation of extracellular matrix, specialization of vessel wall, vessel pruning and regression that are not linear stepwise processes, but rather intercalate each other (Jain, 2003).

Platelet-derived growth factor (PDGF)/PDGF receptor (PDGFR)-β signalling is one of the best characterized pathways that play crucial role in mural cell recruitment. ECs secret PDGFB in response to VEGF and promote the proliferation and migration of PDGFR-β expressing vascular smooth muscle cells (vSMC) and pericytes during vessel maturation (Jain, 2003). Sphingosine-1-phosphate (S1P)/S1P receptor 1 (S1PR1, also known as endothelial differentiation gene 1 [EDG1]), on the other hand, represent another essential pathway that regulates vascular integrity. In contrast to PDGF signalling, the ligand S1P, a product of the membrane sphingolipid metabolism, is secreted by a variety of cells including ECs, erythrocytes and platelets into the circulation. ECs abundantly express S1PR1, a member of the G protein-coupled S1P receptor family. Activation of S1PR1 antagonizes VEGFR2 mediated sprouting angiogenesis and promotes the formation of adherent junctions and cell-extracellular matrix adhesion (Cartier and Hla, 2019). The transforming growth factor beta (TGF-β) signalling pathway is involved in many cellular processes, including, among others, cell growth and differentiation, homeostasis, senescence, apoptosis as well as angiogenesis and vessel maturation. TGF-β1 is a multifunctional cytokine that is ubiquitously expressed by different cell types including ECs and mural cells. Depending on its concentration and the microenvironment, it can be either proangiogenic or antiangiogenic, likely by counter-balancing downstream activation of ALK1 or ALK5. TGF-β1/ALK1/endoglin pathway promotes endothelial cell proliferation and migration, and TGF-β1/ALK5 is involved in maintenance of vessel stabilization. TGF-β1 can also promote vessel maturation by inducing differentiation of mesenchymal cells to mural cells and by stimulating ECM production of ECs and mural cells (Goumans et al., 2009; Jain, 2003). Compared to TGF signalling, angiopoietin (Angpt)/Tie signalling is much more EC specific, as both of the receptors Tie1

and Tie2 are almost exclusively expressed by EC. Angpt1 is the agonist ligand of Tie2 that promotes vessel stabilization and inhibits vascular leakiness whereas Angpt2 is a context-dependent antagonist ligand that can compete with Angpt1 for Tie2 binding (Augustin et al., 2009).

1.2.5 Vessel pruning and regression

The mature hierarchically-structured vascular network is not only the results of cell growth, but also of vascular pruning, the physiological regression of a subset of microvessels within a growing vasculature or even regression of a complete vascular bed (Korn and Augustin, 2015). The best studied example is the mouse postnatal retinal vasculature, where the vessel density at the sprouting front is much higher than in the mature network, which reflects trimming of the overshooting vessels. A four-step model for regression has been proposed, including branch selection, lumen stenosis, EC retraction and resolution (Franco et al., 2015). Vessel regression is a prevalent process for patterning in multiple organs, including the complete regression of the hyaloid vessels during retinal development, the repetitive regression of the newly formed corpus luteum during ovarian cycles, and the gradual regression of the newly formed breast capillary plexuses after lactation (Korn and Augustin, 2015).

The pruning of the vessels can be a combined result of passive survival factor withdrawal and active signalling. EC apoptosis is the primary mechanism of vessel regression in some conditions. For example, withdrawal of VEGF during angiogenesis, drastic metabolic demand changes (e.g. in the lactating breast) or therapeutic tumour targeting can trigger EC apoptosis leading to vessel regression. In other processes, apoptosis could be only a secondary effect, like the disintegrated EC from the vascular bed as the consequence of EC migration away from the regression fragment. In addition, vessel regression is, under certain circumstances, solely a consequence of migration, independent of apoptosis, for instance, during remodelling of redundant loop-forming or parallel vessel segments in the zebrafish midbrain or during mouse embryonic development (Korn and Augustin, 2015).

The primary forces driving vessel pruning and regression include hemodynamic forces, oxygenation and VEGF signalling. Disrupted heart function and impaired blood flow in some mouse mutants lead to impaired vascular remodelling of the yolk sac and eventually to lethality of the embryo. In the same line, pharmacological induction of vasoconstriction or vessel obstruction could promote pruning in zebrafish and mouse retina. On the other hand, stimulation of blood flow can protect vessels from regression, indicating the dependence on hemodynamic forces for vessel pruning. Not surprisingly, tissue oxygenation is another important driver for vessel pruning as it is for sprouting. Hyperoxia suppresses VEGF expression, thus triggering EC apoptosis and vessel regression due to reduced survival signalling (Korn and Augustin, 2015).

1.3 Organotypic vasculature

Although the blood vasculature can be viewed altogether as a single organ and the blood endothelial cells can be hierarchical specified to arterial, venous and capillary EC, the vascular beds in different organs have evolved different features to adapt to specific tissue functions. They are not just passive conduits to circulate oxygen, nutrients and waste, but also actively involved in controlling organ development and homeostasis (Augustin and Koh, 2017). Histologically, blood vessels can be classified as arteries, arterioles, capillaries, venules and veins. While arterial, venous and lymphatic ECs share a conserved morphology as well as molecular characteristics for each type, high heterogeneity has been observed for capillary ECs, both inter-tissue and within the tissue. Morphologically, capillary ECs can be specified into continuous, fenestrated and sinusoidal capillaries. Recent advancement of single cell biology has yield an unprecedent amount of data and unveiled tissue- and organ-specific molecular signatures of EC (Augustin and Koh, 2017; Kalucka et al., 2020).

1.3.1 Morphologically distinct capillaries

Continuous capillaries are characterized by their intercellular tight junctions which restrict the permeability of large molecules and pathogens into the organ. A typical continuous vascular bed is found in the brain. Surrounded by pericytes and astrocytes, the brain endothelium forms a particular tight layer named the blood-brain barrier (BBB) (Augustin and Koh, 2017). An important player in the formation and the maintenance of the BBB is G protein–coupled receptor 124 (GRP124), which is a co-activator of Wnt7a and Wnt7b, thus activating the canonical Wnt signalling (Anderson et al., 2011; Cullen et al., 2011; Zhou and Nathans, 2014). Another continuous vascular bed is the ECs forming the blood-gas barrier in the lung. Lung capillary EC form an ultra-thin cell layer. Together with the alveolar epithelial cells and their intermediate basement membrane, they assemble a sophisticated barrier of less than 2 μm to ensure maximal gas exchange in the lung (Mammoto and Mammoto, 2019).

Fenestrated capillaries are typically found in endocrine glands, including the pineal, pituitary and thyroid glands. These EC are characterized by their intracellular pores penetrating the EC lining, which accelerate the exchange of water and also facilitate the transport of newly secreted hormones and other low-molecular weight hydrophilic molecules. Glomerular EC in the kidney form another prototypic fenestrated endothelium. The efficient filtration of serum into the Bowman's space is realized by the compact loops formed by the glomerular capillaries that allow a maximal contact of blood flow to the filtration unit. Signalling pathways implicated in the development and maintenance of the glomerular include VEGF/VEGFR2 and Angpt1/Tie2 signalling (Augustin and Koh, 2017).

Compared to fenestrated endothelium, sinusoidal endothelium is more permeable due to the gaps, instead of pores in the fenestrated endothelium, between ECs and the inadequate coverage of supporting mural cells and basal lamina. Thus, sinusoidal EC are in direct contact with parenchymal cells, allowing

free exchange of water and solutes, including large molecules like plasma proteins (Augustin and Koh, 2017). A prototypic sinusoidal endothelium is found in the bone marrow. After entering the marrow, arterial vessels divide into arterioles and further into capillaries which span throughout the bone marrow and supply sinusoids, that are radially distributed around the draining central sinus and interconnected by intersinusoidal capillaries. Together, the bone marrow vasculature provides a niche environment for hematopoietic stem cell homing and differentiation and an entrance for blood cell production. Further sinusoidal vascular beds can be found in the liver, spleen, as well as in some endocrine organs (Augustin and Koh, 2017; Kopp et al., 2005).

1.3.2 Single cell resolution of EC heterogeneity

The technical advancement in single cell biology, most significantly single-cell RNA sequencing (scRNAseq) has enabled the high-throughput profiling of thousands of cells, thus yielding unprecedented new resources to uncover previously poorly characterized cell populations and the spatial and functional heterogeneity of the same cell type *in vivo*. Han *et al* and The Tabula Muris Consortium have profiled hundreds of thousands of cells from a large collection of tissues in Mus musculus and generated databases includes tissue-specific cell lineages as well as cross-tissue cell types including stromal cells and immune cells (Han et al., 2018; Tabula Muris et al., 2018). Apart from that these studies enabled discovery and definition of new cell types, these data could also help to delineate the interaction between different cell populations. However, as these studies were not primarily targeting EC, a systematic analysis of organotypic EC was beyond the scope.

More recently, the Carmeliet lab has focused on EC and generated an atlas from 11 tissues (Kalucka et al., 2020). They have recovered the transcriptome from more than 32,000 ECs, from which 78 distinct EC populations have been identified, including (a) traditional artery, capillary, vein and lymphatic EC, (b) tissue-restricted EC populations, (c) unexpected and highly specialized EC phenotypes such as interferon-activated EC, angiogenic EC and proliferating EC. Unexpectedly, artery, capillary, vein and lymphatic EC from each vascular bed grouped together in cross tissue analyses, indicating that one EC population transcriptomically resembles more another EC population from the same tissue than the same EC population from another tissue. Consistently, all EC subclusters also grouped per tissue, rather than per vessel type, by hierarchical clustering, implying that EC heterogeneity is more driven by the tissue microenvironment. In addition, from functionally or anatomically related tissues (brain/testis, liver/spleen, small intestine/colon, and skeletal muscle/heart), the molecular signatures of the ECs are more resembling each other than to less related tissues (Kalucka et al., 2020). Notably, the authors revealed that the vast majority of the screened molecular markers for artery, vein and lymphatic ECs were shared across all tissues, whereas capillary ECs exhibited much more tissue-type-dependent phenotypic variation. This is, however, not surprising considering that capillary EC account for the majority among the different vascular cell types by number, contributing large surface area and are in contact with the tissue

parenchymal cells. In line with this, the identified specialized EC phenotypes are almost exclusively capillary ECs, reminiscent of their tissue specific functions. For instance, angiogenic and proliferating ECs in otherwise healthy tissues (liver and spleen) could represent the high regenerative potential after partial organ excision, especially well-known for the liver, in which ECs play vital role in orchestrating the regenerative process. The *Aqp7*+ capillary EC in the intestine, as another example, might potentially represent an alternative mechanism for glycerol transport from enterocytes into the portal vein (Kalucka et al., 2020).

1.4 The unique liver vasculature

1.4.1 The blood vasculature of the liver

A unique feature of the liver blood vasculature is its dual blood supply. Only 20% of the blood is well oxygenated and delivered by the hepatic artery. The rest is venous blood from the intestine, pancreas, spleen and gall bladder. Both the hepatic portal vein and the hepatic artery enter the liver at the hilus, where lymphatics and efferent bile ducts leave the organ. The vessels then further branch to supply the lobes of the liver. The branches of the hepatic artery and portal vein, together with the bile duct and lymphatic vessels, travel through the liver parenchyma in the portal tracts. Further repeated branching forms the microvasculature, where terminal portal venules and hepatic arterioles merge into sinusoids, which are organized as an extensive anastomotic network and form the exchanging interface with parenchymal cells (McCuskey, 2014). In fact, every hepatocyte is in contact with at least one sinusoidal endothelial cell. Hepatic arterioles also supply the peribiliary plexus of capillaries nourishing the bile ducts and then drain into sinusoids or occasionally into portal venules. After passing the sinusoids, blood is collected in the terminal hepatic venules (central veins) and drains via hepatic veins. This route represents an independent course of the portal tract, which leaves the liver on the dorsal surface to join the inferior vena cava (McCuskey, 2014).

The organization of microvascular unit is integrated into the functional unit of the liver, the liver lobule. In the classic model, the central vein is the central axis and portal tracts distribute along the peripheral boundary. There are considerable sinusoidal anastomoses between adjacent lobules. Therefore, the blood collected by each central venule is from several portal venules. Within each lobule, the organization of the sinusoids is also heterogeneous. Near portal tracts, sinusoids are arranged in interconnecting polygonal networks; farther away, the sinusoids become organized as parallel vessels that terminate in central veins, with short inter-sinusoidal sinusoids connecting adjacent parallel sinusoids. Morphologically, the liver sinusoidal endothelial cells (LSEC) are highly fenestrated EC. A distinct feature of LSEC is their sieve plates consisting 10-100 aggregated fenestrations (Figure 2) (McCuskey, 2014).

While the metabolic zonation of hepatocytes has been long recognized, the heterogeneity of EC is less well explored. Recent advancement in single cell technology has greatly expanded our understanding. It

has been estimated that around 35% of genes expressed by L-EC are spatially zonated along the portal-central axis. Moreover, a panel of specific surface markers and transcription factors for peri-central and peri-portal L-EC has been reported (Halpern et al., 2018). Identification of zonated markers also enables spatial sorting of the heterogenous L-EC into distinct bulk populations, which paves the way for future interrogation of the cellular functions (Halpern et al., 2018). Another study has confirmed the spatial heterogeneity of L-EC, and further identified a small subpopulation of proliferating EC in the liver, in concordance with its high regenerative potential (Kalucka et al., 2020).

1.4.2 The lymphatic vasculature of the liver

Similar to other organs, the lymphatics in the liver function as a tissue drainage system and participate in the immunological surveillance. In contrast to the blood vasculature, lymphatics in the liver are much less interrogated, partially because of the sparsity of lymphatic endothelial cells (~0.8% of all ECs in the liver) and the invisibility on histological sections, which is unproportionate to the fact the 25-50% of the lymph flowing through the thoracic duct is produced in the liver (Kalucka et al., 2020; Ohtani and Ohtani, 2014).

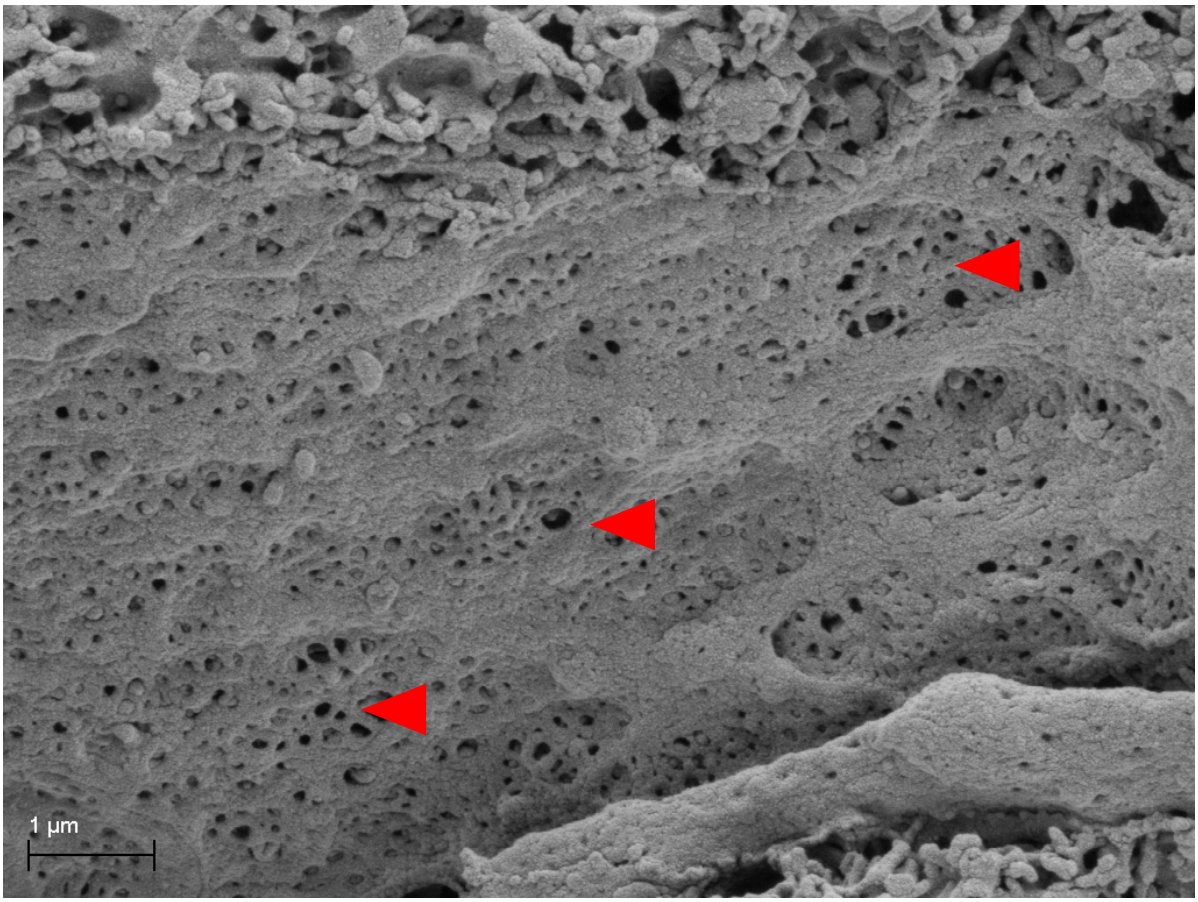

Figure 2. Electron microscopy of liver sinusoidal fenestration. Arrow heads indicate some of the sieve plates. Scale bar: 1 µM. By courtesy of Dr. Inverso.

As almost all the blood flows through the highly permeable sinusoids and the protein concentration of hepatic lymph is about 80 % of the plasma protein concentrations, hepatic lymph is thought to originated from plasma filtered through the fenestrae of L-SECs into the space of Disse, which is the interstitial space between hepatocytes and L-SEC. Fluid in the space of Disse primarily flows towards the space of Mall, which the space between the stroma of the portal tract and the outermost hepatocytes, known as the limiting plate (Tanaka and Iwakiri, 2016). The space of Disse and space of Mall are thought to be directly connected by channels consisting of collagen fibres penetrating through the limiting plate. From the space of Mall, the lymph enters the interstitium of the portal tract and then lymphatic capillaries (Tanaka and Iwakiri, 2016). Strictly speaking, the space of Disse and the space of Mall are not lymphatic vessels, but are considered to be the pre-lymphatic space (Trutmann and Sasse, 1994). In expansion of this view, the sublobular space, bordered by the liver parenchyma and the connective tissue around the sublobular veins, can also be considered as pre-lymphatic space (Trutmann and Sasse, 1994). Another indispensable component for the lymph circulation in the liver is the extracellular matrix network, which provides support to the parenchyma and at the same time, connects the interstitial spaces for lymph flow (Trutmann and Sasse, 1994). Thus, altogether, the liver can be considered in its whole as a "lymphatic organ". The expression of PROX1 by hepatocytes and LYVE1 by L-SEC, both prototypic lymphatic markers, further support this view.

1.5 Angpt-Tie pathway

As mentioned in the previous sections, Angpt/Tie signalling represents a major EC specific signalling system that is involved in multiple processes including vascular sprouting, maturation, remodelling and homeostasis. There are two receptors in this family, namely Tie1 and Tie2, which stands for tyrosine kinase with immunoglobulin and EGF homology domains 1 and 2 (Fagiani and Christofori, 2013). Tie2 was initially designated as Tek, identified in a search for protein tyrosine kinases expressed during murine cardiogenesis (Dumont et al., 1992). The first ligand, Angpt1, was identified a few years later by a secretion-trap cloning approach (Davis et al., 1996). Subsequently, Angpt2, and the mouse and human orthologues Angpt3 and Angpt4, were identified (Fagiani and Christofori, 2013). Both of the receptors are almost exclusively expressed by blood and lymphatic endothelial ECs, with a few exceptions such as haematopoietic cells and in case of Tie2, a subset of monocytes. While Angpt2's expression is primarily EC specific, Angpt1 is expressed by different non-EC cell types including perivascular smooth muscle cells (SMC), pericytes and fibroblast, as well as some tumour cells (Augustin et al., 2009; Saharinen et al., 2017a). In contrast, Angpt3 and Angpt4 are much less investigated. Although they are orthologues, species-specific effects have been observed. Angpt3 can be induced by hypoxia, and both Angpt3 and Angpt4 have been shown to be involved in angiogenesis and vascular remodelling (Saharinen et al., 2017a).

1.5.1 Structure basis of the Angpt ligands and Tie receptors

The sequence and structure of Tie1 and Tie2 are highly similar. Tie1 and Tie2 share 76% identity in the intracellular domain and 30% in the extracellular domain in their primary amino acid sequence. They are both single transmembrane domain proteins sharing the same domain structure. Their extracellular structure contains, from N-terminus, two immnunoglobulin (Ig) motifs, three EGF homology domains, followed by another immunoglobulin motif, and three fibronectin type III (FN III)-like repeats. The intracellular domain contains a split tyrosine kinase (TK) domain at the C-terminus (Figure 3a) (Fagiani and Christofori, 2013).

Angiopoietins are a family of secreted glycoproteins that bind primarily to Tie2 receptor. They consist of an N-terminal super-clustering domain (SCD), a central coiled-coil domain (CCD), a linker region and a C-terminal fibrinogen-related domain (FReD) (Figure 3b). Angpt1 and Angpt2 can form dimers, trimers and tetramers via their CCD and Angpt1 can further assembles into higher order multimers via its SCD. The receptor binding domain is the FReD. Upon binding to Angpt1 tetramers or higher order multimers, Tie2 receptors dimerize and cluster together, bringing their kinase domains in close proximity to allow their trans-phosphorylation (Fagiani and Christofori, 2013). While Angpt1 exists normally in higher order multimeric form, Angpt2 forms dimers and has weak context-dependent Tie2 agonistic function and can

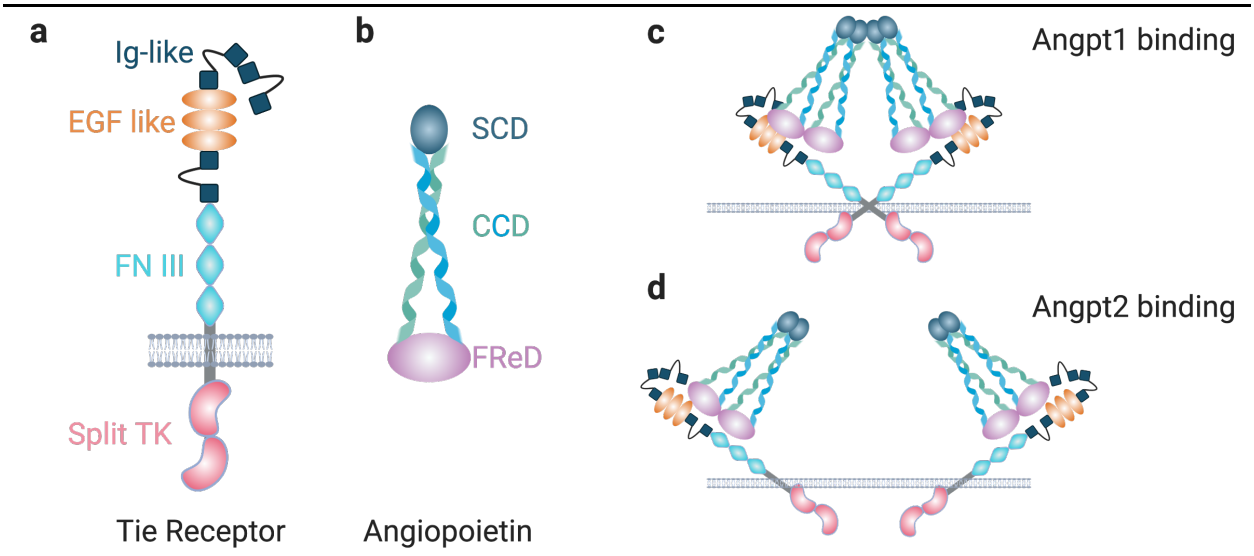

Figure 3. Structure of Tie receptor and Angiopoietin and their binding motif. (a) Tie receptor contains from N-terminus two immnunoglobulin (Ig) like motifs, three EGF homology domains, another Ig-like motif, three fibronectin type III (FN III)-like repeats, a single transmembrane domain and an intracellular split tyrosine kinase (TK) domain at the C-terminus. **(b)** Angpt consists of an N-terminal super-clustering domain (SCD), a central coiled-coil domain (CCD), a linker region, and a C-terminal fibrinogen-related domain (FReD). (c and d) ligand binding motifs for Tie2 receptor. Multimeric Angpt1 can span the ligand binding domains (LBD) of neighbouring Tie2, leading to the receptor dimerization (c), while dimeric Angpt2 cannot (d). Graphic created with Biorender.com.

antagonize Angpt1-mediated Tie2 activation. The functional difference of Angpt1 and Angpt2 may reside in their intrinsic multimeric forming ability and the structure of Tie2 dimers. Tie2 dimerization is mediatedby the formation of an intermolecular β-sheet between the FNIII domains and the ligand binding domain (LBD) consisting of Ig-like and EGF domains. The recently resolved Tie2 crystal structure revealed that the LBDs are located about 300 Å apart from each other in Tie2 dimers, which indicates that multimeric Angpt1 can span these sites, whereas dimeric Angpt2 cannot, which might at least partially explain their functional difference (Figure 3c and d) (Leppanen et al., 2017; Moore et al., 2017; Saharinen et al., 2017b).

1.5.2 Angiopoietin signalling

The angiopoietin ligands bind to the receptor Tie2 and initiate down-stream signalling depending on the context. Angpt1 is constitutively secreted by perivascular cells and its expression is elevated in response to hypoxia, VEGF-A and PDGF-B. Binding to Tie2 induces receptor clustering and auto-phosphorylation at specific tyrosine residues, which leads to the ligand/receptor complex translocation to cell-cell contacts and to formation of trans-endothelial complexes with neighbouring EC. This trans-complex also contains vascular endothelial phospho-Tyr phosphatase (VE-PTP; also known as PTPRB), which signals through AKT. Activated Tie2 binds to the p85 subunit of PI3K, which also activates AKT signalling. Positive downstream regulation of survivin and eNOS and negative regulation of caspase 9 and BAD contribute to the pro-survival effect of Tie2 signalling. Furthermore, activated AKT phosphorylates the transcription factor FOXO1, which leads to its nuclear exclusion and subsequent degradation, and, thus, to down-regulation of FOXO1 targets including Angpt2 (Augustin et al., 2009; Khan et al., 2014; Saharinen et al., 2017a). In addition to PI3K, Tie2 can also recruit growth factor receptor-bound protein (GRB)-2, GRB-7, GRB-14, and protein tyrosine phosphatase nonreceptor type 11 (SHP-2), and mediates via recruiting SOS1 the MAPK signalling (Jones et al., 1999). Through SOS1 and PI3Ks, Tie2 can regulate the activation of RAC1, RHOA, CDC42, and focal adhesion kinase (FAK)-1 that promote cytoskeletal reorganization and migration (Hashiramoto et al., 2007). Tie2 also interacts with A20 binding inhibitor of NF-kappaB activation-2 (ABIN-2), which inhibits NF-κB activity and mediates anti-apoptotic and anti-inflammatory effect (Hughes et al., 2003; Tadros et al., 2003). In addition, Tie2 activation also induces the phosphorylation of STAT1, STAT3, and STAT5A/5B, which then translocate into the nucleus and induce the expression of p21, a potent cell cycle inhibitor, thus mediating endothelial quiescence (Korpelainen et al., 1999).

Angpt2, on the other hand, is a context dependent Tie2 antagonist, which is restrictively expressed by ECs and stored in their Weibel-Palade bodies. The most compelling evidence for the antagonist role of Angpt2 comes from genetic studies. While Angpt2 is dispensable for embryonic development, overexpression of Angpt2 phenocopied Angpt1- or Tie2-deficient mice (Augustin et al., 2009). Angpt2 levels are significantly induced during vascular remodelling, in response to hypoxia, angiogenic or inflammatory stimulation, e.g. VEGF or tumour necrosis factor (TNF). During development, Angpt2 works in synergic with VEGF to

promote sprouting angiogenesis. During inflammation, Angpt2 is release from Weibel-Palade bodies, which attenuates Angpt1-Tie2 signalling, resulting in increased FOXO1 activity and in turn in enhanced Angpt2 expression. In non-inflamed endothelium and some vascular beds that have low levels of Angpt1, Angpt2 acts as a weak agonist for Tie2 (Saharinen et al., 2017a).

Apart from binding to Tie2, Angpt1 and Angpt2 can also interact with integrins in the presence as well as absence of Tie receptors. For example, α5β1 integrin can form heterocomplexes with Tie2 at cellular junctions and regulates the endothelial cell response to Angpt1. In non-endothelial cells, Angpt1 has been shown to interact with αvβ5 integrin in retinal astrocytes, and Angpt2 with α5β1 in some tumour cells and with α3β1 in vascular pericytes. It has been suggested that low Tie2 expression could potentiate the interaction between Angpt2 and integrin in the tip cells of angiogenic sprouts, and this interaction can also promote endothelial destabilization (Saharinen et al., 2017a).

1.5.3 The "orphan" receptor Tie1

Whereas Tie2 integrates the signalling from Angpt1 and Angpt2, the function of its co-receptor Tie1 remains more elusive (Saharinen et al., 2017a). Tie1 can form heterocomplexes with Tie2 on the cell surface through the interaction of their FN3 extracellular domains, which can be differently modulated by Angpt1 and Angpt2 (Leppanen et al., 2017; Seegar et al., 2010). Surface presented Tie1 can be processed by metalloprotease in response to several stimuli, such as phorbol-12-myristate-13-acetate (PMA), vascular endothelial growth factor (VEGF), TNF-α and shear stress changes, which results in the shedding of the extracellular domain (Augustin et al., 2009). The Tie1 endodomain remains associated with the plasma membrane, where it can either form heterocomplexes with Tie2 or it can be further processed by a γ-secretase and is subsequently degraded by the proteasome (Marron et al., 2007).

Genetic knockout studies have shown that global Tie1 deletion leads to embryonic lethality during late gestation as a consequence of microvascular rupture, localized haemorrhage and severe edema (Puri et al., 1995; Sato et al., 1995). Observations in Tie1 hypomorphic mice demonstrated a dosage-dependent effect particularly on the lymphatic vasculature (Qu et al., 2010). During postnatal retinal angiogenesis, Tie1 has been shown to counterbalance Tie2 cell surface presentation in tip cells and to sustain Tie2 signalling in stalk cells, indicating a context-dependent role of Tie1 in modulating Tie2 functions (Savant et al., 2015). *In vivo* studies suggest a major role of Tie1 in supporting the agonistic function of both Angpt1 and Angpt2 in homeostatic conditions. Consistently, when Tie1 is shed from inflamed endothelium, Angpt2 loses its agonistic functions and turns into an antagonist (Kim et al., 2016; Korhonen et al., 2016). Recently, Xu *et al.* have identified the first ligand of Tie1, LECT2, and have highlighted its importance in liver fibrosis progression (Xu et al., 2019). In addition, in a search for cell-surface protein-protein interactions, Tie1 was shown to specifically interact with high-affinity nerve growth factor receptor (NTRK1, or TrkA), in the presence and/or absence of nerve growth factor (NGF) (Wojtowicz et al., 2020) (Wojtowicz 2020). The functional relevance of this interaction has not yet been established. The

expression of TrkA in neuronal tissue (Amatu et al., 2019) and of Tie1 on endothelial cells could support a trans-cell interaction, which might be involved in vessel-guided neuronal patterning during development, and points towards a possible Tie2-independent function of Tie1.

1.6 Wnt signalling pathway in maintaining liver homeostasis and pathogenesis

Wnt signalling is a conserved pathway throughout the animal kingdom and controls a myriad of cellular processes in development and adult life. In mammals, 19 Wnt ligands have been identified. They represent a family of short ranging morphogens (Clevers and Nusse, 2012). Bioactive Wnts need to be glycosylated and palmitoylated by the enzyme porcupine, which renders Wnts relatively insoluble. The secretion requires the cargo receptor Wntless (also known as Evi) to mediate the trafficking between the Golgi apparatus and the cell membrane. Frizzled proteins are the primary receptors for Wnt ligands. The Frizzled family consist 10 different members in mammals. They share a conserved extracellular cysteine-rich domain, which is followed by a domain containing seven presumptive transmembrane segments (Wang et al., 2016). It is intuitive to assume that different Wnt/Frizzled combinations would initiate different signalling routes and, thus, contribute to the signalling complexity and specificity. However, the binding selectivity of Wnt/Frizzled and the coupled downstream signalling remain largely unknown so far (Dijksterhuis et al., 2014). Further, the selective involvement of co-ligands and co-receptors can also influence the signalling outcome, adding another dimension of complexity (Dijksterhuis et al., 2014). Depending on downstream mediators, there are canonical Wnt/β-catenin signalling, noncanonical Wnt/calcium and noncanonical PCP pathways, and some other recently identified β-catenin-independent Wnt pathways (Russell and Monga, 2018).

1.6.1 Canonical Wnt/β-catenin signalling

β-catenin is the major transducer of Wnt signalling. Its protein level is kept low by default in the absence of Wnt ligands. β-catenin is degraded by the so-called destruction complex, which consists of Axin, adenomatous polyposis coli (APC), glycogen synthase kinase (GSK) 3β, and casein kinase 1α (CK1α). Axin functions as a scaffolding protein, bringing together the other components and mediating sequential phosphorylation events on β-catenin. Phosphorylated β-catenin is recognized by β-transducin repeat-containing protein (βTRCP), which is part of an E3 ubiquitin ligase complex, triggering the ubiquitination and subsequent degradation of β-catenin. In the vicinity of Wnt secreting cells, the binding of Wnt to its Frizzled receptor and the co-receptor, low-density lipoprotein receptor-related protein (LRP) 5 or 6, leads to the recruitment of the scaffolding protein Dishevelled (Dvl) and to the phosphorylation of LRP5/6. Phosphorylated LRP5/6 then recruits Axin to the cytoplasmic membrane, which leads to the subsequent disruption of the destruction complex, resulting in the stabilization and accumulation of β-catenin. Subsequently, the non-phosphorylated form of β-catenin translocates to the nucleus and promotes the expression of target genes via formation of complexes with T cell factor/lymphoid enhancer factor (TCF/LEF) transcription factors (Russell and Monga, 2018). R-spondins (Rspo) are another family of

secreted cysteine-rich glycoproteins, which functions as co-ligands of Wnts and can potentiate canonical Wnt/β-catenin signalling. Binding of R-spondins to their receptors, leucine-rich repeat-containing G protein–coupled receptor-4 (LGR4) and LGR5, enhances the Wnt-dependent phosphorylation of LRP6 (Raslan and Yoon, 2019). In addition, Rspo inhibits the transmembrane E3 ubiquitin ligases zinc and ring finger 3 (ZNRF3) and its homolog ring finger protein 43 (RNF43), which target Frizzled and LRP6 for ubiquitination and proteasomal degradation (Hao et al., 2012; Koo et al., 2012).

1.6.2 Noncanonical Wnt signalling

While the Wnt1 classical ligands, including Wnt2, Wnt3, Wnt3a, and Wnt8a, function via the canonical Wnt/β-catenin signalling pathway, some other Wnts initiate β-catenin-independent signalling, including Wnt4, Wnt5a, Wnt5b, Wnt6, Wnt7a, and Wnt11 (Chae and Bothwell, 2018). The noncanonical Wnt ligands bind to Frizzled-2, Frizzled-7 or receptor tyrosine kinase-like orphan receptor 2 (Ror2) and induce the Wnt/calcium pathway or the PCP pathway. The formation of a complex containing Frizzled, Dvl and G proteins activates phospholipase C (PLC). PLC subsequently cleaves phosphatidylinositol 4,5 biphosphate (PIP_2) into diacylglycerol ([DAG], activating protein kinase C [PKC]) and inositol 1,4,5-triphosphate ([IP3], which increases intracellular calcium levels). Elevated calcium levels activate calcium/calmodulin-dependent kinase II (CaMKII) and calcineurin (CaN), which regulate cell migration and proliferation (Russell and Monga, 2018). In the PCP pathway, the initial complex is composed of Ror2, Frizzled and Dvl, and can trigger the activation of Rho-family small GTPases, which subsequently activate Rho-associated protein kinase (ROCK) and c-Jun N-terminal kinase (JNK) to regulate cell polarity and migration (Russell and Monga, 2018).

There are also some Wnts that are reported to initiate both canonical and noncanonical signalling, for instance, Wnt9b. Lan *et al* and Jin *et al* have reported that Wnt9b and Rspo2 functionally cooperate and potentiate noncanonical Wnt/β-catenin signalling in regulating facial morphogenesis in mice (Jin et al., 2020; Jin et al., 2012; Lan et al., 2006). Karner et al have shown that Wnt9b-mediated canonical signalling can respond in distinct ways depending on the cellular environment and thus balances progenitor cell expansion and differentiation during kidney development (Karner et al., 2011). On the other hand, the same group has identified earlier the involvement of Wnt9b in the regulation of planar cell polarity and kidney tubule morphogenesis (Karner et al., 2009). Wnt9b, together with other noncanonical Wnts, has been shown to antagonize Wnt3a-induced β-catenin/TCF activity in a reversibly-immortalized hepatic progenitor cell line (iHPx) (Fan et al., 2017).

1.6.3 Wnt signalling in the liver

Wnt signalling cascades are involved in almost every facet of liver biology. During development, Wnt signalling, as in many other organs, is crucial for the differentiation and positional patterning of cells. β-catenin deficiency leads to embryonic lethality due to gastrulation defects (Russell and Monga, 2018).

In adult liver, Wnt2, Wnt9b and Rspo3, predominantly secreted by peri-central L-ECs, are major determinants of hepatic zonation (Leibing et al., 2018; Rocha et al., 2015). Conditional deletion of Rspo3 leads to a drastic reduction of Wnt target gene expression (Axin2 and Lgr5) as well as to the loss of pericentral marker glutamine synthetase (GS) expression (Rocha et al., 2015). Similarly, LSEC specific ablation of Wnt secretion also results in reduced target gene expression and also to a reduced liver-to-body weight ratio (Leibing et al., 2018). It has been estimated that about half of hepatocyte expressed genes are zonated, from which approximately one-third are Wnt targets, which concordantly also exhibit expression patterns consistent with Wnt regulation: Wnt-activated genes are mostly peri-centrally zonated and Wnt-repressed genes are peri-portally zonated (Ben-Moshe and Itzkovitz, 2019). Another feature of the liver is its remarkable regenerative potential. Wang *et al.* showed that peri-centrally located Axin2-positive diploid hepatocytes subserves the homeostatic hepatocyte renewal (Wang et al., 2015). In addition, the protein level of β-catenin is enhanced within minutes after partial hepatectomy and the expression of Wnts is enhanced several fold at 12 h post-surgery (Monga et al., 2001; Preziosi et al., 2018). When Wnt secretion is abrogated, a notable delay in liver regeneration is observed, as demonstrated by reduced PCNA and cyclin-D1 expression (Preziosi et al., 2018).

1.7 Aim of the study

Due to its crucial function and the unique vascular system, the liver is a prototypic organ to understand the intravascular heterogeneity. Recent developments in single cell biology have enabled the dissection of the complex transcriptomic heterogeneity of hepatocytes as well as L-EC along the axis of the liver lobule from the portal to the central vein, revealing that a great proportion of genes are differentially expressed (Halpern et al., 2018; Halpern et al., 2017).

While gene expression correlates for most molecules strongly with protein abundance, protein function and eventual biological outcome is regulated in multi-layered processes of post-translational modifications (PTM), which are not reflected in the current scRNAseq-defined spatial organization and biochemical division of labour in the liver. This lack of information hampers our current understanding of fundamental biological features of the liver. For example, while the strongly localized expression of short-range acting L-EC-derived Wnt ligands in the central vein area is well-known (Rocha et al., 2015; Wang et al., 2015), the molecular determinants of this process are yet to be elucidated. These considerations highlighted the critical need of an multiomic approach able to cover both gene expression information in terms of transcriptome and proteome and a functional readout well represented by a broad phosphoproteomic analysis. Moreover, the acquired data need to be integrated and correlated to the complex morphological structure of specific tissues in order to study the tissue heterogeneity.

As proteomics and even more so phosphoproteomics are still beyond the boundaries of single cell resolution, the overall goal of this project is to establish a comprehensive multi-omics platform, specifically designed to perform transcriptomic, proteomic and phosphoproteomic analysis of the endothelial cells while preserving the spatial information of the analysed tissue. Starting from the spatial-sort methodology of the liver EC established in our lab, I focused on three specific aims: i) To establish a cell isolation procedure that allows to isolate a large number of L-EC from mice and at the same time preserve the phosphorylation status of the endothelium in order to provide the first *in vivo* phosphoproteome of a vascular endothelium with spatial resolution and define a phosphorylation signature of the different traits of the liver vasculature; ii) to define expression parameters that allow quantification of gene expression and protein phosphorylation along the liver sinusoid with the goal to provide a comparative zonation of both gene expression and protein activation. iii) to select an array of different data visualization modalities that allow an intuitive comparison of different datasets to liver vasculature morphology.

All together I could establish a complete work flow including cell isolation and processing, data analysis and integration and finally dataset visualization for a multiomic and spatially resolved characterization of the liver endothelium.

Moreover, I applied the multiomic approach to screen for candidate EC molecules responsible for shaping the endothelial cell zonation along the hepatic sinusoid. In particular, I identified localized phosphorylation of tyrosine kinases and further zoomed in on candidate molecules able to regulate the

production of the EC derived Wnt ligands, especially Wnt9b, which was among the most zonated genes, and the localized expression is required for the maintenance of the hepatocyte metabolic zonation and is essential to an efficient liver regeneration. The endothelial specific RTK Tie1 was identified in the screening approach and I further aimed to characterize the downstream signalling events linking to Wnt production. In addition, as the pathways downstream of Tie1 signalling remains largely unexplored and the ectodomain shedding has been implicated in multiple studies for a functional role, the last aim of the study is to generate *in vitro* and *in vivo* tools to facility the characterization of the functional relevance of Tie1 shedding.

2. RESULTS *

2.1 Study design and methodology

A crucial step for high-throughput sequencing is the pre-amplification step, which is also a limiting factor for deep coverage of the proteome by mass spectrometry (MS) and even more so is for PTM, especially phosphorylation. Due to the reversible and substoichiometric nature of the signalling events, phosphorylated peptides represent only a very small fraction in the digested protein extract, rendering phosphoproteomic analyses remaining challenging (Needham et al., 2019). Most studies targeting the phosphoproteome require a pre-enrichment step of phosphopeptides. Population enrichment methods include, among others, immobilized metal affinity chromatography (IMAC) and metal-oxide affinity chromatography (MOAC), which apply a positively charged chromatography matrix that binds to negatively charged phosphate moieties (Fila and Honys, 2012; Qiu et al., 2020). These methods intrinsically have a prerequisite for large input amount. For example, at least 0.1 mg protein extract was required for the Fe^{3+}-IMAC column (Potel et al., 2018). And empirically, 0.4 mg input is required to obtain optimal result, which is challenging for rare cell (sub)population *in vivo*.

Technically, single-cell proteomics, and even more so single-cell phosphoproteomics, are still in their infancy. To overcome these technical limitations, spatial fluorescence-activated cell sorting (FACS), later referred briefly as spatial sorting, was established together with Dr. Inverso based on the scRNAseq-defined gradual increase of cKit expression along the portal-central liver lobule axis (Halpern et al., 2018). L-EC from different lobular position: portal node (PN), peri-portal (PP), peri-central (PC) and central vein (CV) could be isolated (Figure 4a), enabling bulk analyses of L-EC functions, while retaining spatial information.

Considering the low protein abundance of L-EC and the high input requirement for phosphoproteome analysis, to obtain sufficient material, L-EC from 30 C57BL/6N mice were pooled towards this end as one biological replicate. In total, four biological samples were included for parallel transcriptomic, proteomic and phosphoproteomic analyses. (Figure 4b). With the support of multiple collaborators, I processed the samples for RNAseq and mass spectrometry and performed data processing, quantification, analysis and result interpretation.

** The experiments of this PhD thesis were in close collaboration with and under direct supervision of Dr. Donato Inverso, a postdoctoral fellow in the laboratory. Moreover, some of the experiments and analyses were performed with the assistance of collaborators at DKFZ (Martin Schneider, Dr. Dominic Helm and others at Genomics and Proteomics Core Facility; Dr. Tianzuo Zhan at Division of Signalling and Functional Genomics), Heidelberg University (Dr. Renata Blatnik, Dr. Thomas Ruppert and others at the Core Facility for Mass Spectrometry & Proteomics at the ZMBH) as well as external collaborators at Strasbourg University, France (Marziyeh Komeili and Dr. Christine Schaeffer-Reiss) and at the Weizmann Institute in Rehovot, Israel (Shani Ben-Moshe and Dr. Shalev Itzkovitz). Eli Lilly Pharmaceuticals in Indianapolis, USA (Dr. Sudhakar Chintarlapalli) made critical reagents available that were essential for some of the experiments. I performed all experiments summarized in this PhD thesis. Some contributions of collaborators are included solely to reflect the comprehensiveness of the study. Yet, this is acknowledged in the text or in the figure legends throughout the Results section.*

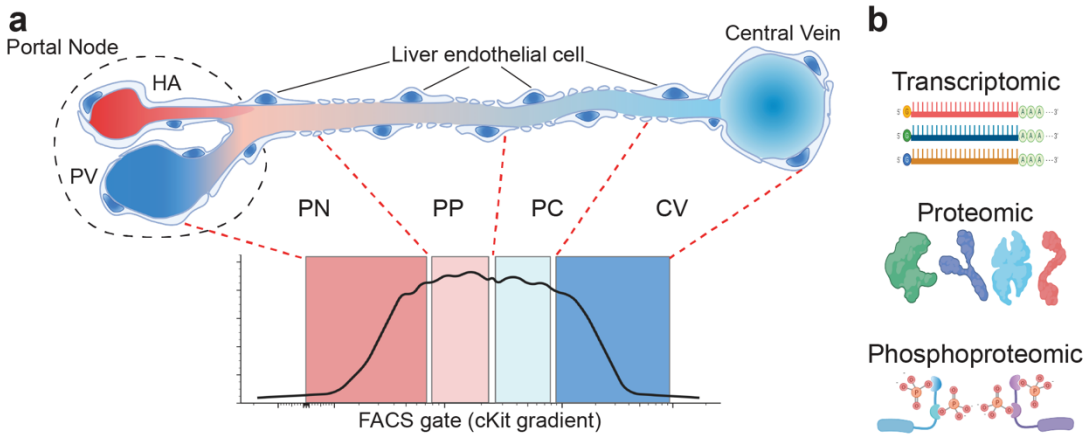

Figure 4. Overview of the spatial sort strategy. (a) FACS gating strategy based on cKit staining and the corresponding L-EC populations. **(b)** Spatially sorted L-EC can be pooled for measurements that require large input material, such as the RNAseq, mass spectrometry and phosphopeptide enrichment. Graphic created with Biorender.com.

2.1.1 Liver endothelial cell isolation and sorting strategy

It has been reported that tissue dissociation and FACS can trigger transcriptomic changes (Denisenko et al., 2020; van den Brink et al., 2017), which could, hence, also impact protein and PTM levels. Further, flow shear stress induced gene expression as a consequence of the perfusion step for liver cell isolation was observed for Klf2 and Klf4 (data from Dr. Inverso, not shown). To minimize these effects, 40 µg/ml Liberase™ was supplemented to the liver digestion medium and the perfusion rate was reduced to optimize the tissue dissociation protocol (Mederacke et al., 2015). Moreover, pre-purification of L-EC with CD146 magnetic beads was performed before sorting to reduce the processing time. As demonstrated in Figure 5a (work of Dr. Inverso), the purity of L-EC after beads enrichment reached approximately 95% of the live singlets of liver non parenchymal cells (NPC), which dramatically reduced the sorting time. These ultrapure L-EC were eventually sorted into four consecutive populations based on the intensity of cKit staining, which was further controlled by co-staining with CD141, which is another peri-central zonated gene (Figure 5b, work of Dr. Inverso).

2.1.2 Overview of the multi-omic results

First of all, as the quality control of the multi-omic data sets, the total number of genes, proteins, and peptides were compared between different zones (Figure 6a). The total numbers were comparable among the zones, indicating that the technical variance was well controlled.

The cDNA libraries from the spatial sorting samples were sequenced by the High Throughput Sequencing Unit of the Genomics and Proteomics Core Facility in DKFZ and I processed the demultiplexed FASTQ files by applying the established workflow “HTseq Workflow RNAseq using STAR Featurecounts Single Read” on the DKFZ internal Galaxy instance (Afgan et al., 2018). TPM was calculated accordingly and a total of 28.727 genes were identified, with approximately 20.000 per zone (Figure a and b). The discrepancy

between total number of genes and identified genes per zone suggests an almost full coverage of the L-EC transcriptome.

For label free MS based proteome analysis, protein samples from spatial sorting were processed, measured and quantified by the Protein Analysis Unit and the High Throughput Sequencing Unit of the Genomics and Proteomics Core Facility at DKFZ. Almost 5,000 proteins were identified in each zone, comparable to the totally identified number (5,015) of proteins across all zones. This is not surprising considering that for mass spectrometry the dynamic range is the rate limiting factor, due to the saturation by abundant peptides while low expressed proteins are not covered.

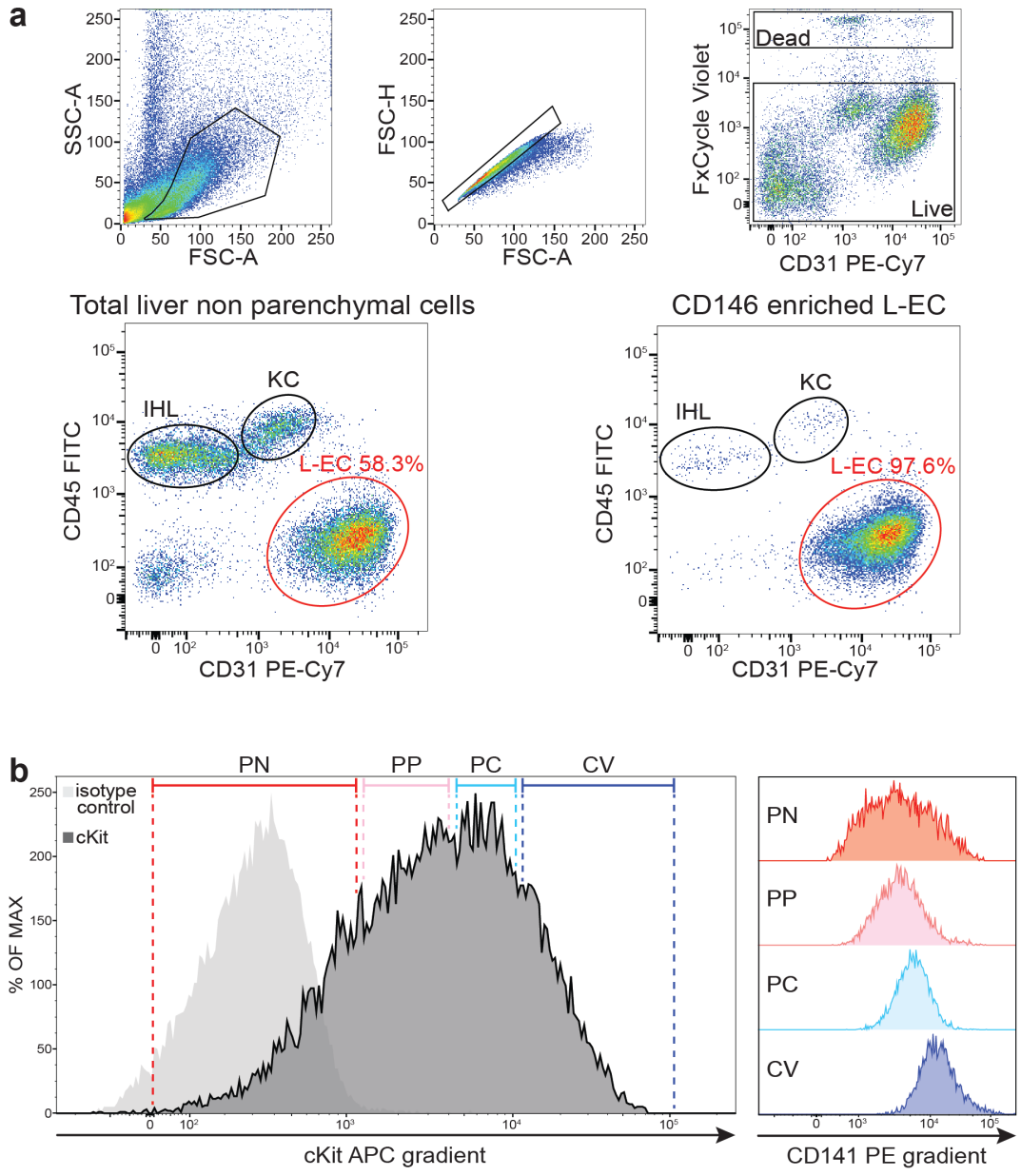

Figure 5. FACS gating strategy. (a) Gating strategy for CD146 magnet beads pre-enriched L-EC population. (b) Spatial sort of L-EC primarily based on cKit and controlled by CD141. By courtesy of Dr. Inverso.

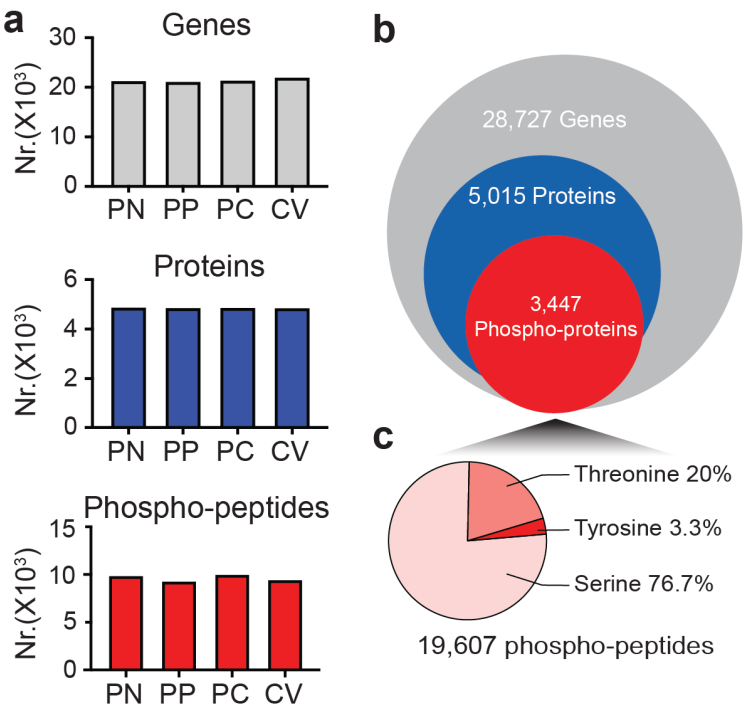

Figure 6. Overview of the multi-omic results. (a) Total number of detected genes (grey), proteins (blue) and phospho-sites (red) in each zone/sorting gate. (b) Cumulative data including all the samples. For phosphoproteome, the class I peptides were mapped to the corresponding protein. (c) The distribution of the three quantified phosphosites.

For the phosphoproteome analysis, with the support of the Core Facility for Mass Spectrometry & Proteomics (CFMP) at ZMBH, a stable isotope dimethyl labelling approach was selected to best facilitate the result quantification (Hsu and Chen, 2016), as multi-steps of processing, especially phosphopeptide enrichment, intrinsically generates variation. To be specific, I pooled a fraction of each sample as an internal control and processed in parallel with the samples for digestion, desalting, isotope labelling of the peptides. The samples were dimethyl labelled as “light” and internal control as “medium”. Subsequently, the internal control was equally spiked into each sample, allowing normalization of the variation generated in the following steps. Phosphopeptide enrichment was performed by M. Komeili, formerly at University of Strasbourg, with the AssayMap Bravo platform. LC-MS/MS analysis and peptide identification and quantification were performed by the Protein Analysis Unit of the Genomics and Proteomics Core Facility at DKFZ. Less than 10,000 phosphopeptides were identified in each zone, while the total number across all zone (19,607) was twice more. Such discrepancy could hint towards highly dynamic post-translational regulations along the lobular axis. Considering only class I peptides, which are defined by at least 0.75 localization probability, the identified phosphopeptides could be mapped to 3,447 different proteins (Figure 6b). These proteins do not completely overlap with the label free MS identified proteins, mainly for the two reasons: (i) proteins that are abundant but not/lowly phosphorylated will not be detected in the phosphoproteomic analysis; (ii) the enrichment step for phosphopeptides removed peptides skewed the relative abundances from peptides of high abundance and low phosphorylation towards lowly abundant, but highly phosphorylated peptides.

2.1.3 Analysis of non-EC contaminants in RNAseq and mass spectrometry

In order to assure that the selected FACS gates were greatly enriched for EC and, moreover, that there were no zonation confounding effects due to non-EC contamination, the fraction of non-EC markers in the RNA and protein samples was estimated with bioinformatic support from S. Ben-Moshe.

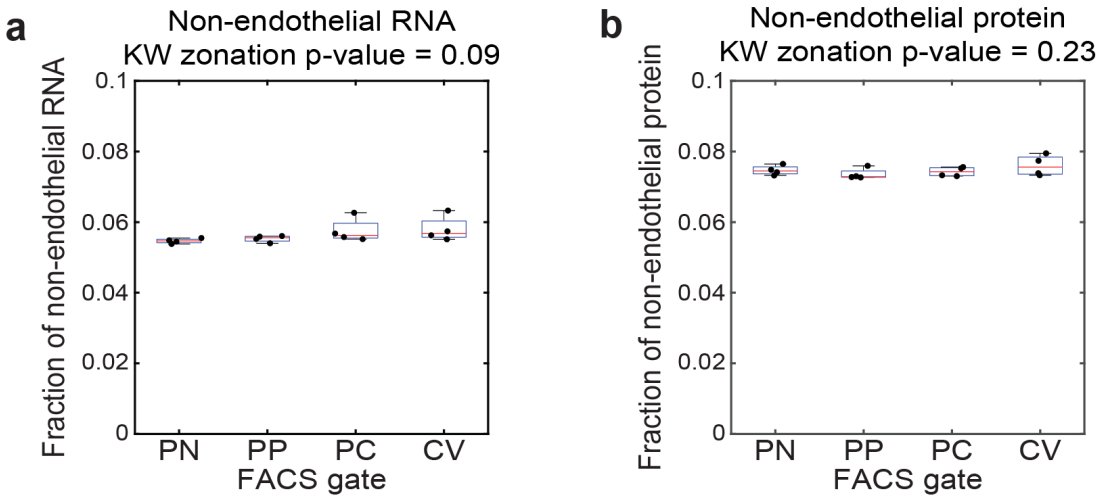

Figure 7. Contamination control of non-EC liver cell populations. Fraction of contaminants in each gate for RNAseq **(a)** and mass spectrometry **(b)** data. By courtesy of S. Ben-Moshe.

To this end, a list of previously published transcriptomes of different liver cell types was compiled. Liver immune cell types and EC expression were taken from Halpern et al. (2018). The hepatocyte transcriptome was retrieved from Halpern et al. (2017). Cholangiocyte data were extracted from averaging expression data of single cholangiocytes resulting from single cell sequencing of mouse healthy liver as reported by Xiong et al. (2019). Hepatic stellate cell and fibroblast expression data were taken from Dobie et al. (2019). Expression data were normalized to the sum of each cell type, resulting in the expression fraction of each gene in each of the cell types' transcriptomes.

The 5,000 most highly expressed genes from each cell type were pooled to a set of 11,617 unique genes. These genes were further filtered and were considered as non-EC markers if the fraction of the gene in EC was less than $1x10^{-5}$ and if the ratio between the expression in at least one non-EC type and EC was 10-fold or higher. A special case was the hepatocyte, which is substantially larger than EC and higher in RNA content. Hepatocyte markers therefore passed our filter if the expression ratio between hepatocyte and EC was 2-fold or higher. In total, 2,626 genes passed this filter. And the fraction of these non-EC markers out of the total expression for each FACS gates was calculated.

A total of 2,275 non-EC marker genes could be detected in the EC RNA data. The fractions across the zones ranged between 0.055 and 0.063, clearly demonstrating EC predominance. Next, Kruskal Wallis tests was performed to check whether there was a statistically significant difference in the fraction of non-EC across the four different FACS gates. Kruskal Wallis test on the sum of these genes across the different FACS gates was insignificant (p-value = 0.089), indicating that there was no difference in fraction of non-EC along the different sorted populations (Figure 7a). Therefore, the obtained L-EC heterogenous expression patterns along the portal-central axis was unlikely due to the contaminant.

Similarly, 219 non-EC marker genes were found in the label free MS data, with fractions across the zones ranging between 0.073 and 0.080, and no significant differences between the zones (Kruskal Wallis p-value = 0.235, Figure 7b). Taken together, these results demonstrated that the spatial sorting strategy yielded highly purified L-EC with neglectable contamination from non-EC populations and the differential expression across the zones is reliable without confounding effect from the contaminants.

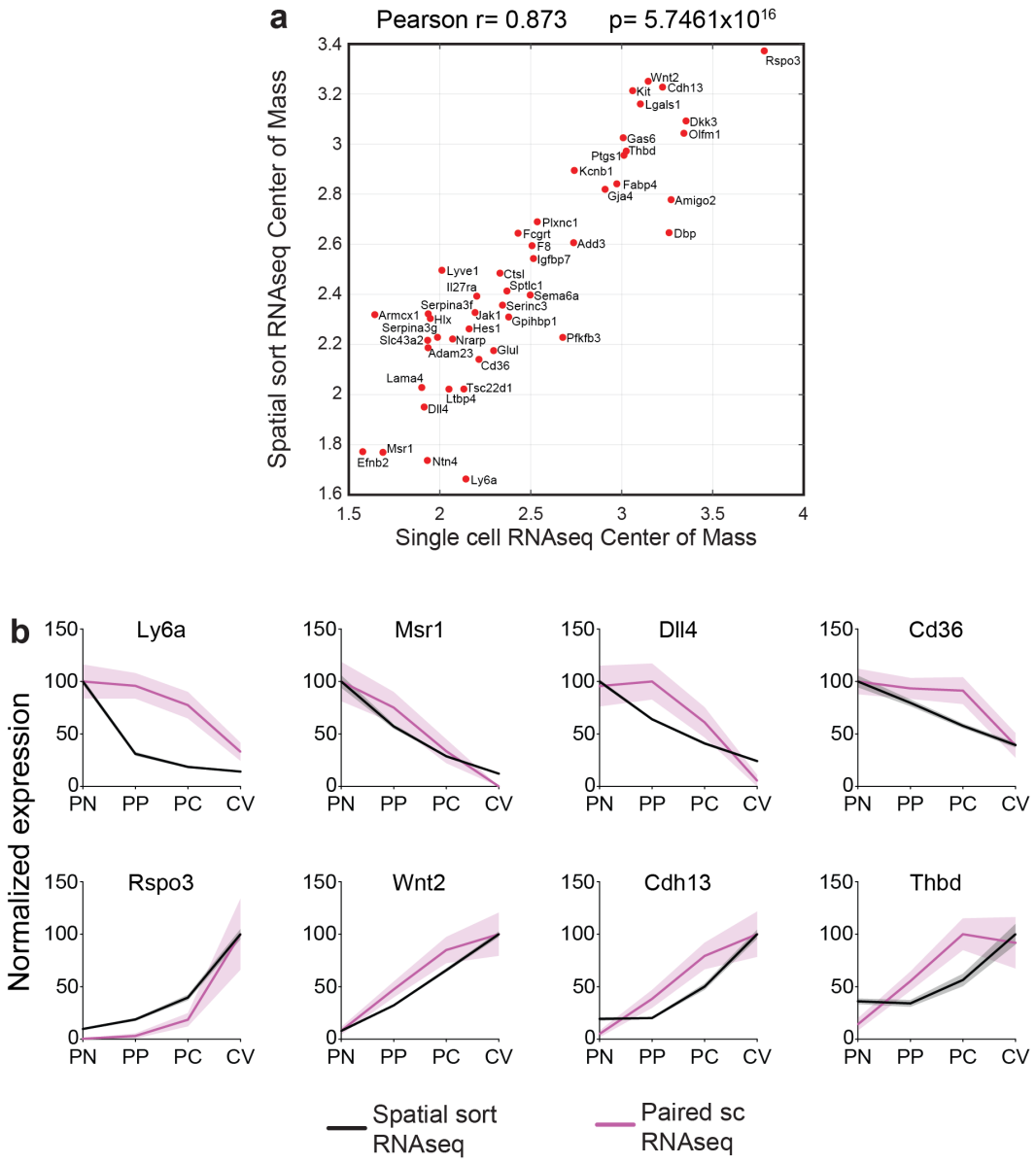

Figure 8. Spatial sort RNAseq to scRNAseq correlation. (a) RNA expression Centre-of-Mass (CoM) from single cell (X axis) and spatial sort (Y axis) RNAseq of the 48 genes significantly zonated in both datasets. **(b)** Expression profiles of representative portal (top row) and central (bottom row) zonated mRNA from scRNAseq (magenta line) and spatial RNAseq (black line). Expression is normalized to the maximum; patches represent SEM. Results generated with bioinformatic support from S. Ben-Moshe.

2.1.4 Correlation of spatial sort RNAseq and published scRNAseq

To further demonstrate the robustness of the spatial sort approach, the spatial sort RNAseq results were compared with the published scRNAseq data with bioinformatic support from S. Ben-Moshe (Halpern et al., 2018). Centre-of-Mass (Methods), which was a gross indication of the zonation, was used to correlate the two datasets. Following the blood flow direction, portal zone was defined as zone 1, peri-portal as 2, peri-central as 3 and central as 4. Therefore, the lower the CoM, the stronger a gene was zonated towards the portal side; conversely, the higher the CoM, the stronger a gene is zonated towards central. Similarly, for the scRNAseq dataset, each cell was assigned to the corresponding zone and the mean gene expression was used for calculation of the CoM. The CoM values from 48 genes that were zonated in both datasets were correlated and high correlation was observed (Figure 8a, $r_{Pearson}$ = 0.873, p-val = 5.7 X 10^{16}). In addition, some landmark genes were selected and their patterns were overlappingly plotted (Figure 8b). As expected, I could observe highly similar patterns between the two datasets. Overall, the comparison demonstrated the high reproducibility of both datasets.

2.2 Transcriptome of spatially sorted L-EC

2.2.1 Heterogeneous patterns of L-EC transcriptome

Next, I performed analysis on the transcriptome to obtain insight for the heterogeneous expression patterns of the L-EC expressed genes. Only genes with a mean TPM >1 in at least zone was processed for further analysis, which made for a total 13,737 genes. Kruskal Wallis (KW) tests were performed to check for differential gene expression in at least one zone with a p-val cut-off at 0.05. Next, to adjust the multiple hypotheses, Benjamini–Hochberg (BH) correction was performed on the KW p-values. Instead of focusing on individual genes, a general zonation overview was desired. Therefore, a false discovery rate (BH q-val) of 0.25 was accepted. A total of 4,943 genes were found to be zonated in the spatial sort RNAseq, as shown in Figure 9a. Compared to the scRNAseq dataset, which identified 475 zonated genes, the spatial sort extended the resolution by an order of magnitude, demonstrating the robustness of this approach.
A closer examination of the heatmap led to the observation that while the majority of genes polarized zonation towards either portal or central, some genes exhibited distinct patterns. Therefore, the definition of zonation patterns was refined (Methods), by taking into account the continuum nature of the vasculature. In addition to the previously established portal and central zonation patterns, sinusoidal and large vessel patterns were defined. Although this has been reported for individual genes, for instance, *Lyve1* and *Stab2* (Halpern et al., 2018), a distinct pattern was not assigned mainly due to the relative rareness of these genes and the sparsity of single cell datasets. This limitation could now be overcome with the higher resolution obtained from bulk RNAseq, which enabled the clustering of a large number of genes to either sinusoidal and large vessel patterns (Figure 9b). As a proof-of-concept, the zonation patterns of two prototypic genes, CD31 and LYVE1, were confirmed by immunofluorescent (IF) staining for their large vessel and sinusoidal pattern, respectively, as shown in Figure 9c.

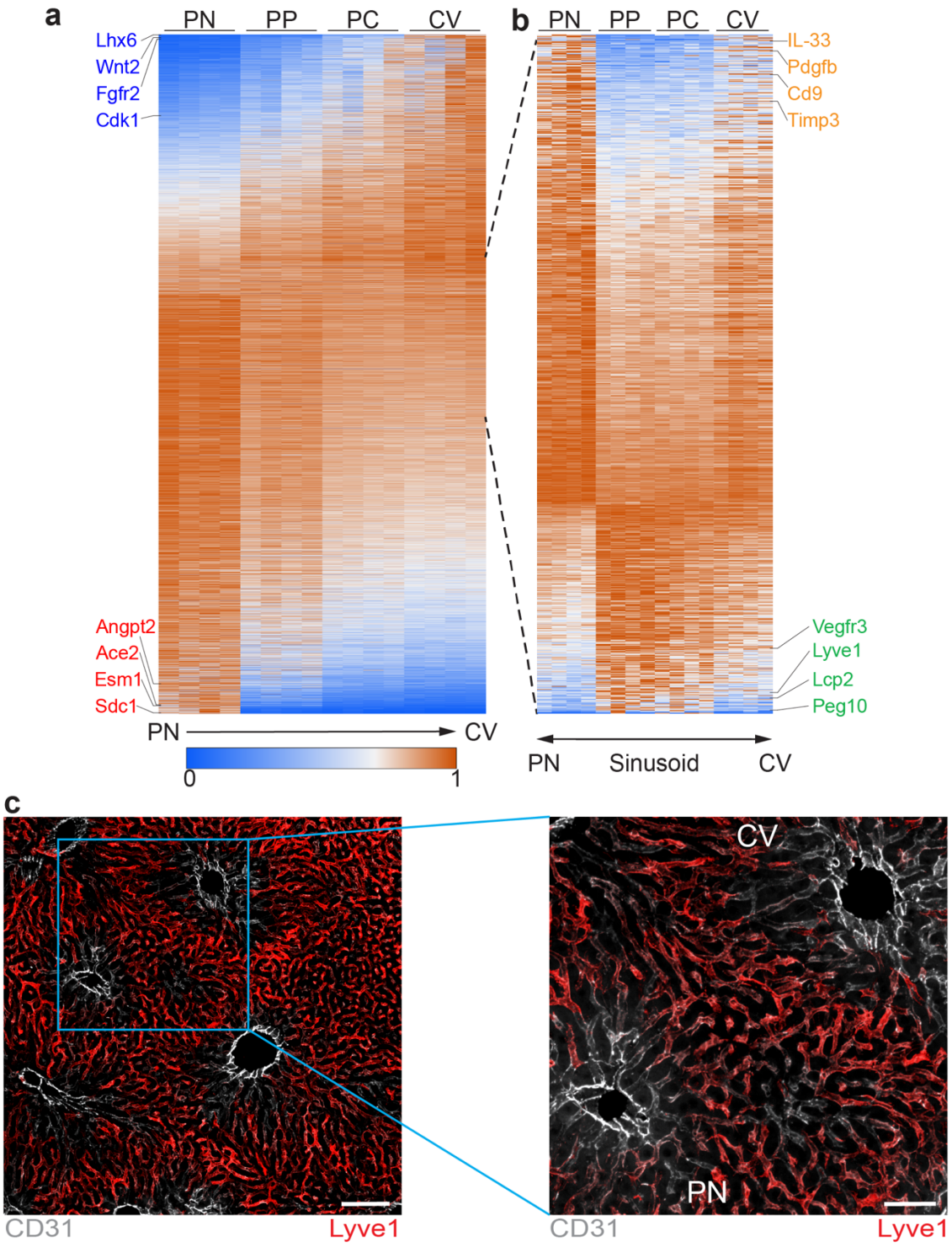

Figure 9. Zonation patterns of the L-EC transcriptome. (a) Heat map representation of 4,943 zonated genes. Genes are normalized to their maximum expression and sorted by their Centre-of-Mass. **(b)** Expression profiles of 890 genes zonated on vessels or sinusoids. Genes are normalized to their maximum expression and sorted by their vessel to sinusoid log2 fold change. **(c)** Liver immunofluorescence staining of CD31 (large vessel, grey) and Lyve-1 (sinusoid, red). Scale bars: 100 µm (left), 50 µm (right). Representative images from three C57/B6 mice.

Next, representative genes for each pattern were validated by qRT-PCR assay. Unsurprisingly, RNAseq-defined zonation patterns were almost 100% reproduced by qPCR as evidenced by perfectly overlapping expression profiles (Figure 10), demonstrating the robustness of the spatial sort approach. Interestingly, we could observe subtle differences within the same zonation pattern. For examples, Sdc1 expression is strongly enriched in the portal zone, and exhibited a sharp decrease in expression in the peri-portal zone, which remained at a low level in the peri-central and the central zone. In comparison, Esm1 had a more gradual and linear decrease along the portal to central axis, while Angpt2 was expressed to similar extents in the portal and peri-portal zone, with a subsequent gradual decline in expression towards the central side. A similar heterogeneity was observed among the central patterns. Large vessel zonation was defined by a lower expression in sinusoidal areas than in the combined large vessel area (portal and central). However, we observed that some genes had prominent expression in the portal zone and that the expression in the central zone was only slightly higher than in the sinusoidal area. Similarly, the conversed pattern was also observed. This led to the exclusion of genes with extremely low (<2.2) or high (>2.8) CoM. Still, distinct patterns could be observed for large vessel zonation: portal dominant, central dominant or equal expression. All combinations of subtle differences could eventually generate a rather distinct gene signature in neighbouring cells, fining tuning the cellular function along the lobular axis.

Collectively, the bulk analysis of spatially sorted L-EC populations was capable of increasing the sequencing depth by an order of magnitude in comparison to the previous scRNAseq (Halpern et al., 2018), revealing that approximately one third of quantifiable L-EC transcripts were, in fact, expressed in a zonated manner.

2.2.2 Zonation of transcription factors of L-EC transcriptome

Transcription factors are proteins which bind to DNA regulatory sequences and directly promote or repress gene transcription. They are, therefore, major drivers of cellular function and behaviour. We could identify 970 transcription factors in our transcriptome analysis, out of which 365 were expressed in a zonated manner. This provided a valuable resource for future studies to understand, for example, possible driving forces of L-EC zonation and how cells integrate intrinsic, as well as extrinsic cues that result in transcriptional changes. Figure 11 provides a list of the top zonated transcription factors in the L-EC (KW q-val < 0.01).

As expected, transcription factors involved in arterial specification were identified to be zonated portally, for instance *Hey1*, which is down-stream of Notch signalling. Sox7, on the other hand, which was reported to function in conjunction with COUP-TFII for venous specification, was zonated on central (Park et al., 2013). Intriguingly, the lymphatic fate determining transcription factor, *Sox18,* displayed portal zonation, whereas lymphatic identity markers *VEGFR3* and *Lyve1* were enriched in the sinusoidal area, delineating a unique hybrid phenotype of L-EC between lymphatic and vascular EC (Park et al., 2013; Tanaka and Iwakiri, 2016; Trutmann and Sasse, 1994).

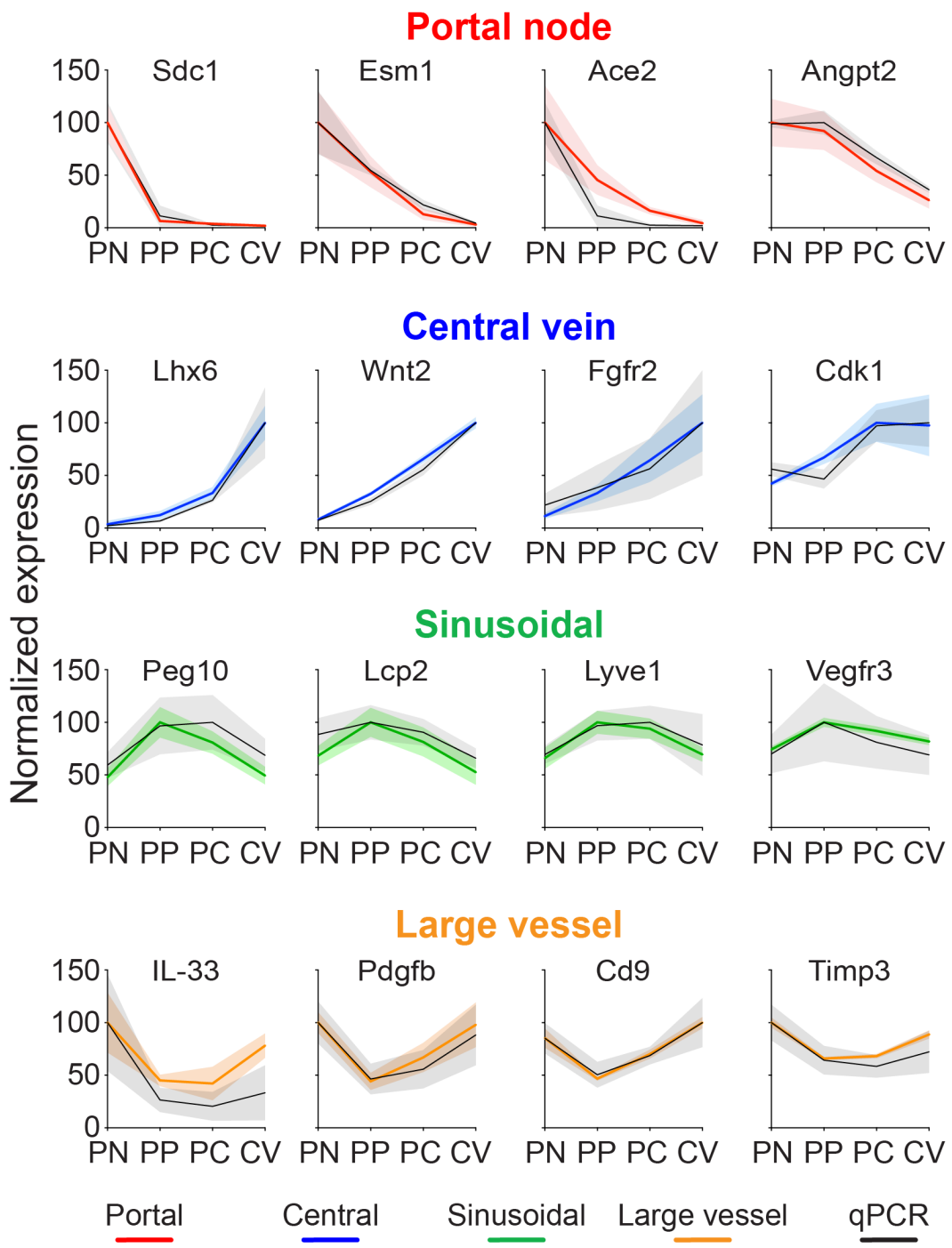

Figure 10. Validation of RNAseq by qRT-PCR assay for each zonation pattern. Representative expression profiles of qRT-PCR validation (black) and the corresponding pattern indicated by colour. Expression is represented as percentage of maximum; patches represent SD. qRT-PCR was performed on spatial sorted L-EC samples from four mice (n=4).

2.2.3 Zonation of kinases of L-EC transcriptome

Protein kinases represent one of the largest protein families and their deregulation is linked to a variety of malignancies (Manning et al., 2002). Under supervision of Dr. Inverso, I extracted the known list of mouse kinases from UniProt to overlap with the spatial sorting results. Next, I performed the phylogenetic analysis of the L-EC expressed kinases with CORAL (Metz et al., 2018). In the L-EC transcriptome, 74% (381/515) of known kinases were detected, which is represented in the kinome phylogenetic tree (Figure 12). Overall, the tyrosine kinases (TK) seemed to be more centrally expressed, while the kinases from CMGC family (cyclin-dependent kinases [CDKs], MAPKs, GSK and CDK-like kinases) showed stronger portal expression. Other kinase families, on the other hand, did not exhibit a general zonation trend. This could indicate a functional distribution of different kinase families along the lobular axis. The data would serve as a value resource to help illuminating the largely elusive relationships between kinases and their substrates, for example, by bioinformatically integrating the zonated expression/activation of kinases with substrates to score for potential interactions.

Among the kinases, 186 members were found to be zonated on a transcriptional level. Figure 13a provides and overview of the top zonated kinases (KW p-val<0.01) and the expression pattern of typical portal or central zonated genes were displayed in Figure 13b. *Bmx* was initially found to be specifically expressed in the endocardium and the endothelium of large arteries (Ekman et al., 1997), which was in concordance with its extreme portal zonation pattern.

Another strongly portal zonated genes, *Insr* (Insulin receptor) was widely expressed in most cell types.

Another strongly portal zonated genes, *Insr* (Insulin receptor) was widely expressed in most cell types. Considering the metabolic function of the liver and the rather quiescent phenotype of L-EC under homeostatic condition, the zonation of *Insr* was likely to be related to the nutrient/Insulin gradient following direction of the blood flow (Payankaulam et al., 2019). Interestingly, like *Bmx* and *Insr*, the two most centrally zonated kinases, *Fgfr2* and *Kit*, are all tyrosine kinases. *Fgfr2*, together with *Fgfr1* and *Fgfr3*, was expressed by L-EC, but not *Fgfr4* and *Fgfr5*, different with cultured HUVEC (Antoine et al., 2005), indicative of an organotypic expression. EC and hematopoietic deletion of Fgfr1 or Fgfr2 has no effect on normal embryonic development but impairs neovascularization after skin or eye injury (Oladipupo et al., 2014). Considering their relatively low expression, it could be assumed that they could have similar functions, for example, to promote liver regeneration after injury. *Kit* gene, also known as cKit or CD117, is the surface marker that was used in this project for spatial sorting. cKit is predominantly expressed in bone marrow stem cells as well as endothelial and cardiac progenitor cells (Cheng and Qin, 2012). cKit+ population from isolated adult lung endothelial cells, had higher colony formation ability *in vitro* and can generate functional blood vessels *in vivo* (Fang et al., 2012). The same group has also reported that around 18% CD31+ L-EC are cKit positive (Fang et al., 2012), most likely represented the central zonation of cKit expression. Together with the putative role of FGFRs, central L-EC could represent a stem cell like subpopulation.

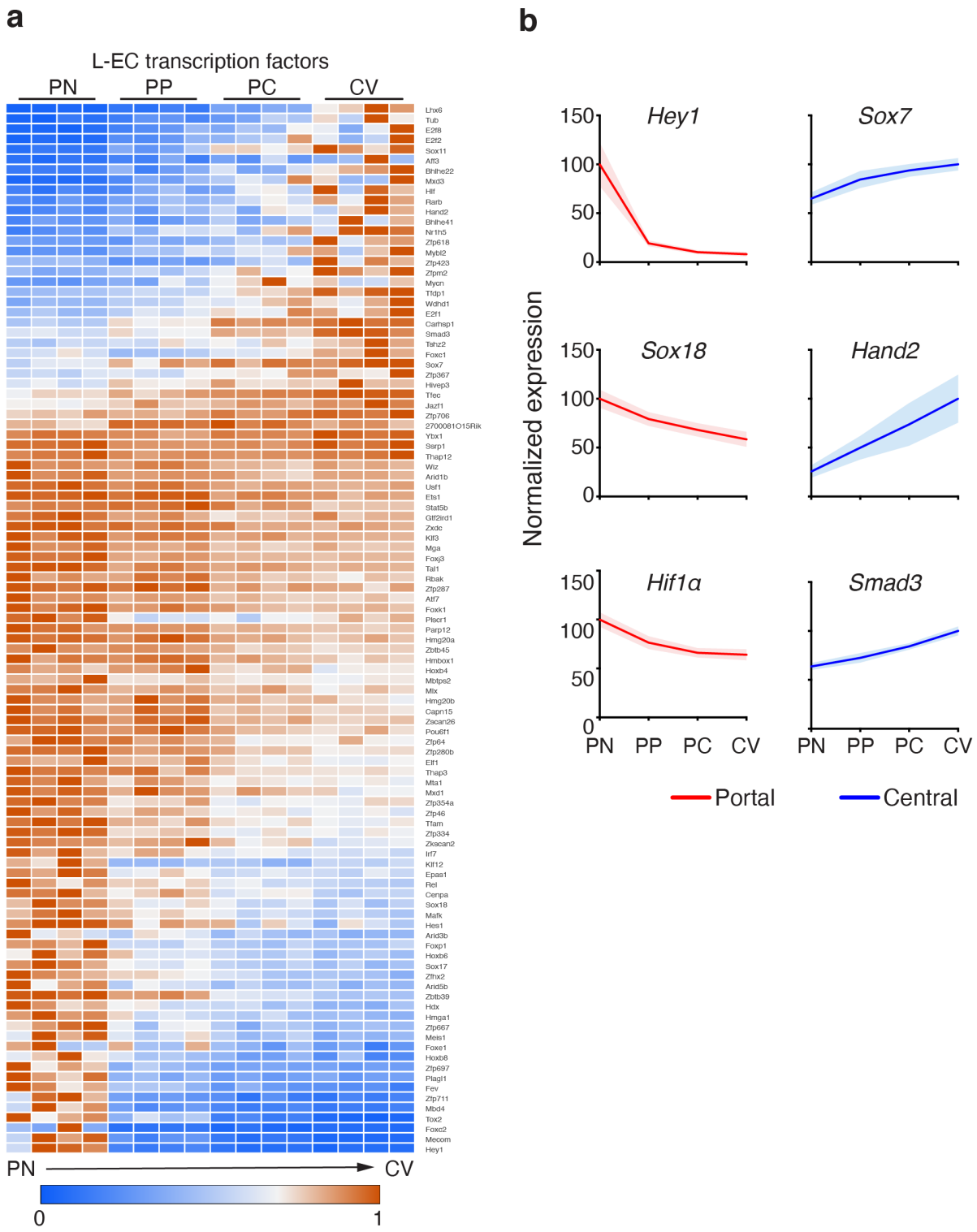

Figure 11. The Zonated transcription factors (TF). (a) Heat map representation of 103 most zonated TF. Genes are normalized to their maximum expression and sorted by their Centre-of-Mass. **(b)** Representative expression profiles portally (red) or centrally (blue) zonated TF. Expression is represented as percentage of maximum; patches represent SD.

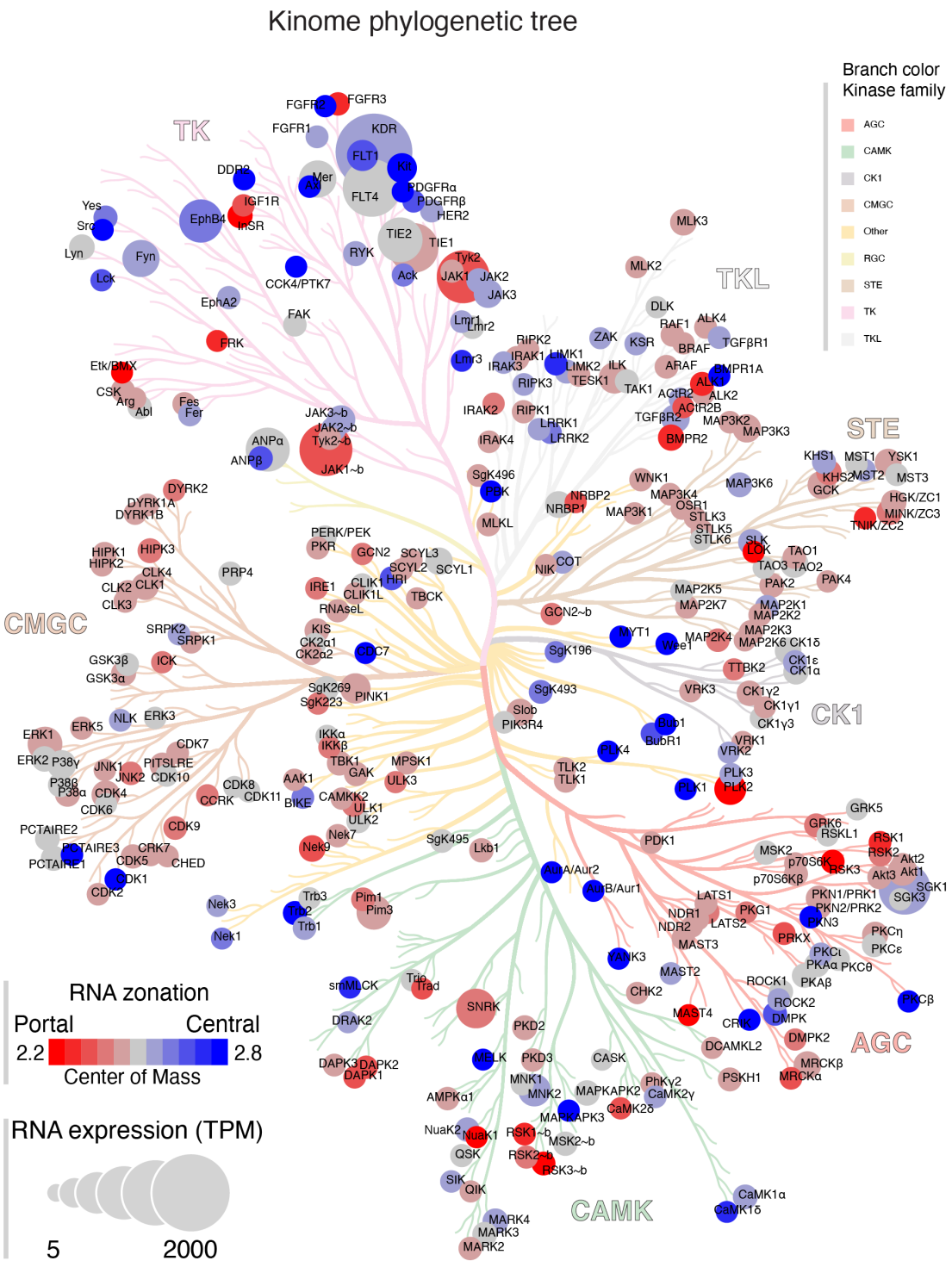

Figure 12. Kinome phylogenetic tree of L-EC kinases. Each kinase is represented by a circle and grouped by kinases family. The circle size is proportional to the mean TPM across zones. The colour represents expression zonation from portal (red) to central (blue).

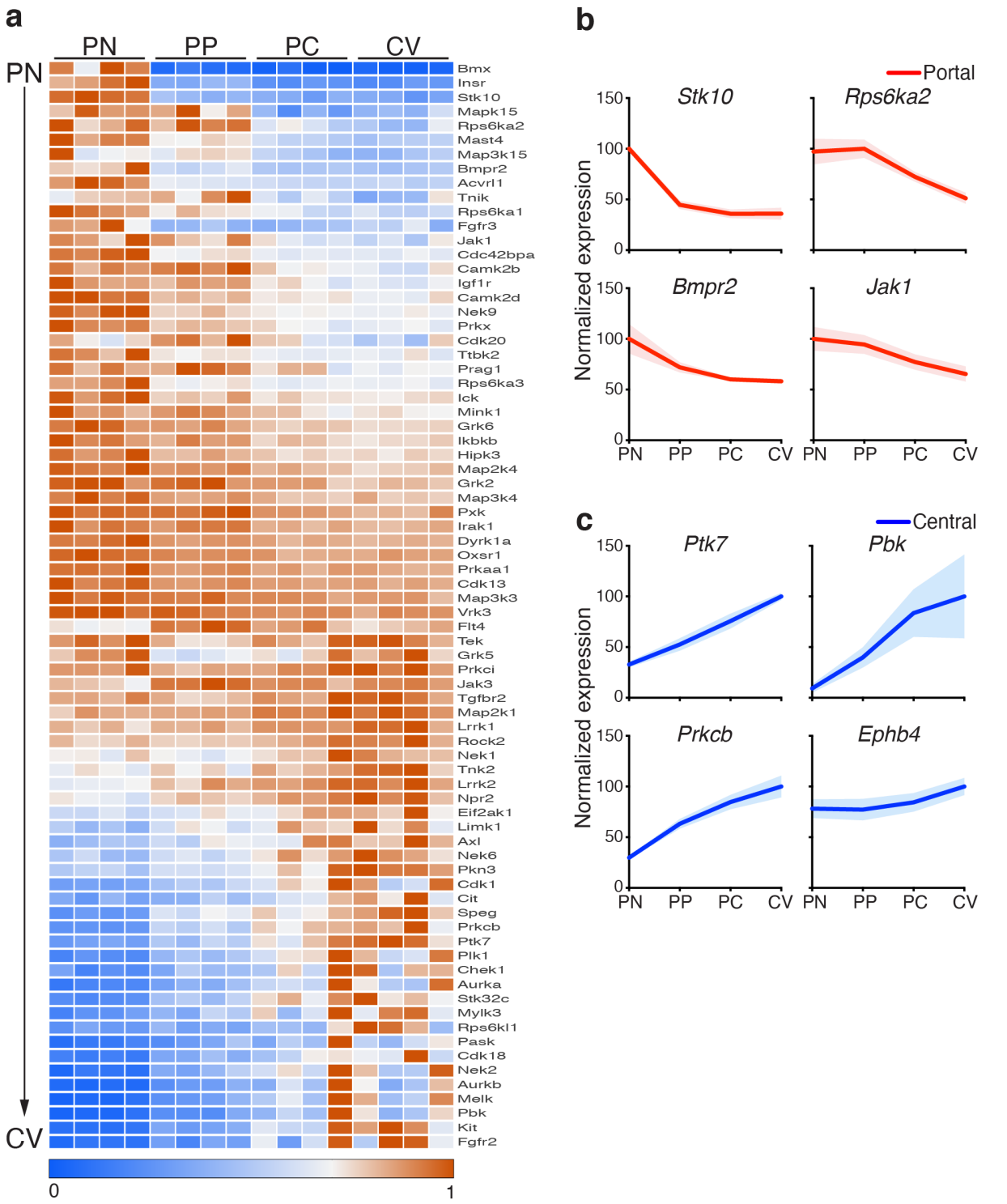

Figure 13. Zonation of L-EC kinases. (**a)** Heat map representation of the expression profiles of 76 significantly zonated kinases. Genes are normalized to their maximum expression and sorted by their Centre-of-Mass. (**b** and **c**) Representative expression profiles of portal (**b**, red) and central (**c**, blue) zonated kinases. Gene expression is represented by percentage of maximum; patches represent SD.

2.2.4 Zonation of phosphatome of L-EC transcriptome

Similar to the kinome analysis, I performed the phylogenetic analysis of the L-EC expressed phosphatases with CORALp (Min et al., 2019). L-EC expressed most of the known phosphatases (98/127), with 52 of them being zonated (Figure 14). Phylogenetic analysis revealed that the expression was rather distributed in different families with the exception of histidine phosphatase (HP) family that was almost absent in L-EC (Figure 14a). The best-known vascular phosphatase is *Ptprb*, also known as VE-PTP, which was also the most abundant phosphatase in L-EC and displayed zonation pattern of large vessel. Souma *et al* have demonstrated that absence of VE-PTP confers an agonist function of Angpt2 on Tie2 in lymphatic endothelium while the presence of VE-PTP abrogates this function in blood endothelium (Souma et al., 2018). Although abundantly expressed by all L-EC, sinusoidal L-EC indeed expressed less VE-PTP compared to large vessels, substantiating the previous notion that sinusoidal L-EC display a lymphatic phenotype. Interestingly, the expression of Tie2 was similarly zonated on vessels but the ligand Angpt2 was on portal node. It would be interesting in the future to integrate also the pattern of non-EC expressed Angpt1 in the liver lobule, and study the differential functional output of this pathway relative to different gradient of ligands and negative regulation by the phosphatase. In comparison to VE-PTP, the other zonated phosphatases were much less expressed. As the most portal zonated gene (Figure 14b), PTPRE was abundantly expressed by HUVEC, which did not express VE-PTP (Thompson et al., 2001). In contrast, LSEC expressed PTPRE was around 200 times less than VE-PTP, which might point towards an organotypic function or culture induced phenotype. A prominent target of PTPRE is insulin receptor (Liang et al., 2019), which was similarly zonated on portal side, indicating a possible negative regulatory machinery. All the zonated phosphatases are shown in the heatmap and representative patterns are shown for selected genes (Figure 14). The heterogenous expression of phosphatases, together with the aforementioned kinases, indicates a multi-level regulation of the L-EC transcriptome, which likely also reflects protein activity.

2.3 Proteome of spatially sorted L-EC

To quantitively assess the L-EC proteome, I included in the following analysis only proteins quantified in at least two samples from at least one zone. The missing values for protein expression (LFQ) were imputed by MinDet, i. e., to replace the missing values by the minimum value observed in each sample (Lazar et al., 2016). The technical variance between biological replicates in mass spectrometry was observed to be much higher than for the transcriptome. Therefore, samples were further normalized for each experimental replicate (Methods). Out of the 5,015 identified proteins, 4,346 were included for zonation analysis. Similar to the transcriptome, around 25% of the quantified L-EC proteome was found to be expressed in a zonated manner along the portal-central axis of the liver lobule.

2.3.1 Zonation of the L-EC proteome

Among the quantified proteins, 319 were zonated at the central side and 366 at the portal side (Figure 15a). Proteins from each pattern were subjected to pathway analysis against the KEGG database (Kanehisa and Goto, 2000) by STRING (Szklarczyk et al., 2019). The most prominent central enriched pathway was “DNA replication” (Figure 15b), including the genes *Fen1, Mcm2, Mcm3, Mcm4, Mcm5, Mcm6, Mcm7, Pcna* and *Rfc5*. Minichromosome Maintenance (MCM) proteins form the best-known protein family involved in replication initiation complex. MCM2-7 are six conserved proteins found in all eukaryotes, which form a stable heterohexamer acting as DNA helicases (Neves and Kwok, 2017). In addition, MCMs are also involved in DNA damage response, chromatin structure and transcription control (Forsburg, 2004). Considering that Axin2-positive hepatocytes, which serve as a stem cell like population to renew the homeostatic parenchyma, were also peri-centrally located, the enrichment of “DNA replication” pathway in central L-EC suggested a possible endothelial progenitor role, which was previously implicated by the central zonation of *Fgfr2* (Section 2.2.3).

On the other hand, the portal enriched pathways were mainly metabolism and biosynthesis related, including “porphyrin and chlorophyll metabolism”, “metabolism of xenobiotics by cytochrome P450”, “drug metabolism - cytochrome P450”, “glutathione metabolism”, “fatty acid degradation”, “alanine, aspartate and glutamate metabolism”, “carbon metabolism”, and “arginine biosynthesis”, “thyroid hormone synthesis”, “biosynthesis of amino acids” and “glycolysis / gluconeogenesis” (Figure 15b). This observation could be explained by the direction of blood flow that exposes portal ECs to nutrient-rich blood, which consequently seemed to induce more metabolic activities compared to central EC that are exposed to nutrient-depleted blood. This, however, is in stark contrast to the metabolic division of labour in hepatocytes, where, for instance, cytochrome P450 pathway molecules are enriched on the central side of hepatocytes (Ben-Moshe et al., 2019). Together, these findings suggested a heterogenous metabolic behaviour of different liver cell populations despite their anatomical proximity.

Not surprisingly, pathways enriched in large vessels (Figure 16) were typical for continuous endothelium, including “cell adhesion molecules (CAMs)”, “gap junction”, “focal adhesion”, “adherens junction” and “tight junction”, which was in contrast to the fenestrated sinusoids. In addition, the sinusoidal enrichment of metabolic pathways including “glycosaminoglycan degradation”, “cysteine and methionine metabolism” and “amino sugar and nucleotide sugar metabolism” was expected, as the major nutrient and waste exchange between the blood and parenchyma happens at the sinusoids area. Interestingly, we could also observe an enrichment of pathways related to “DNA replication”, “homologous recombination”, “mismatch repair”, and “nucleotide excision repair”. The higher metabolic activity and higher exposure of bacterial derived toxins from gut due to the low flow rate, could represent a threat for genomic stability, thus repairing machineries are more active in sinusoids.

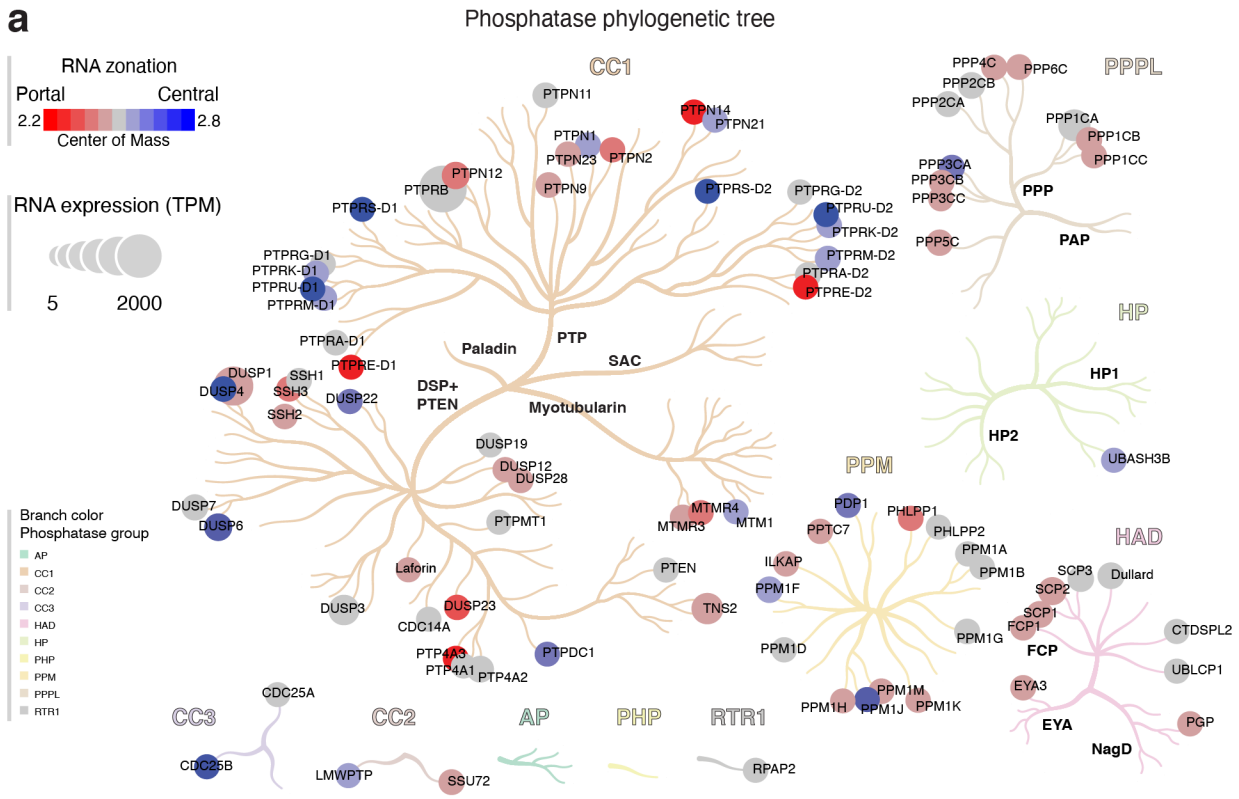
a
Phosphatase phylogenetic tree
RNA zonation
Portal
Central
2.2
2.8
Center of Mass
RNA expression (TPM)
5
2000
Branch color
Phosphatase group
AP
CC1
CC2
CC3
HAD
HP
PHP
PPM
PPPL
RTR1
CC1
PPPL
PPP
PAP
HP
HP1
HP2
PTP
Paladin
SAC
DSP+
PTEN
Myotubularin
PPM
HAD
FCP
EYA
NagD
CC3
CC2
AP
PHP
RTR1
PTPN11
PTPN14
PTPN21
PTPN1
PTPN23
PTPN2
PTPN12
PTPRB
PTPN9
PTPRS-D1
PTPRS-D2
PTPRG-D2
PTPRU-D2
PTPRK-D2
PTPRM-D2
PTPRA-D2
PTPRE-D2
PTPRG-D1
PTPRK-D1
PTPRU-D1
PTPRM-D1
PTPRA-D1
PTPRE-D1
DUSP1
SSH1
DUSP4
SSH3
DUSP22
SSH2
DUSP19
DUSP12
DUSP28
DUSP7
DUSP6
PTPMT1
Laforin
DUSP3
DUSP23
CDC14A
PTP4A3
PTP4A1
PTP4A2
PTPDC1
CDC25A
CDC25B
LMWPTP
SSU72
RPAP2
PTEN
TNS2
MTMR4
MTMR3
MTM1
PPM1F
ILKAP
PPM1D
PDP1
PPTC7
PHLPP1
PHLPP2
PPM1A
PPM1B
PPM1G
PPM1H
PPM1J
PPM1K
PPM1M
SCP3
Dullard
SCP2
SCP1
FCP1
CTDSPL2
UBLCP1
EYA3
PGP
PPP4C
PPP6C
PPP2CB
PPP2CA
PPP1CA
PPP1CB
PPP1CC
PPP3CA
PPP3CB
PPP3CC
PPP5C
UBASH3B
b
Ptpre
Ptprj
Ptpn14
Ptp4a3
Dusp23
Cdc14b
Phlpp1
Ptpn12
Ssh3
Ppm1h
Ptc7
Ssu72
Ctdsp2
Ppp1cb
Mtmr3
Ppm1m
Ssh2
Ppp4c
Ptpn9
Ctdsp1
Ppp6c
Ppp3cb
Ppp1cc
Ppp3cc
Eya3
Pten
Ptprb
Ppm1a
Ppm1g
Ppp2cb
Ptprg
Ctdspl
Ptprn
Ppm1f
Ptpn1
Mtm1
Ubash3b
Pdp1
Ptpdc1
Dusp22
Ppm1j
Ppm1l
Cdc25b
Dusp10
Ptprs
Ptpn13
Ptpn3
Cdkn3
Dusp4
Ptprr
Cdc25c
Ptprt
CV
PC
PP
PN
1
0
PN
CV
c
Portal
Ptpre
Dusp23
Normalized expression
150
100
50
0
PN
PP
PC
CV
d
Central
Dusp4
Ptprs
Normalized expression
150
100
50
0
PN
PP
PC
CV

Figure 14. Zonation of L-EC phosphatases. (a) Phosphatome phylogenetic tree of L-EC phosphatases. Each phosphatase is represented by a circle and grouped by phosphatases family. The circle size is proportional to the average TPM across zones. **(b)** Heat map representation of the expression profiles of 52 significantly zonated phosphatases. Genes are normalized to their maximum expression and sorted by their Centre-of-Mass. The colour represents expression zonation from portal (red) to central (blue). **(c** and **d)** Representative expression profiles of portal (c, red) and central (d, blue) zonated phosphatases. Gene expression is represented by percentage of maximum; patches represent SD.

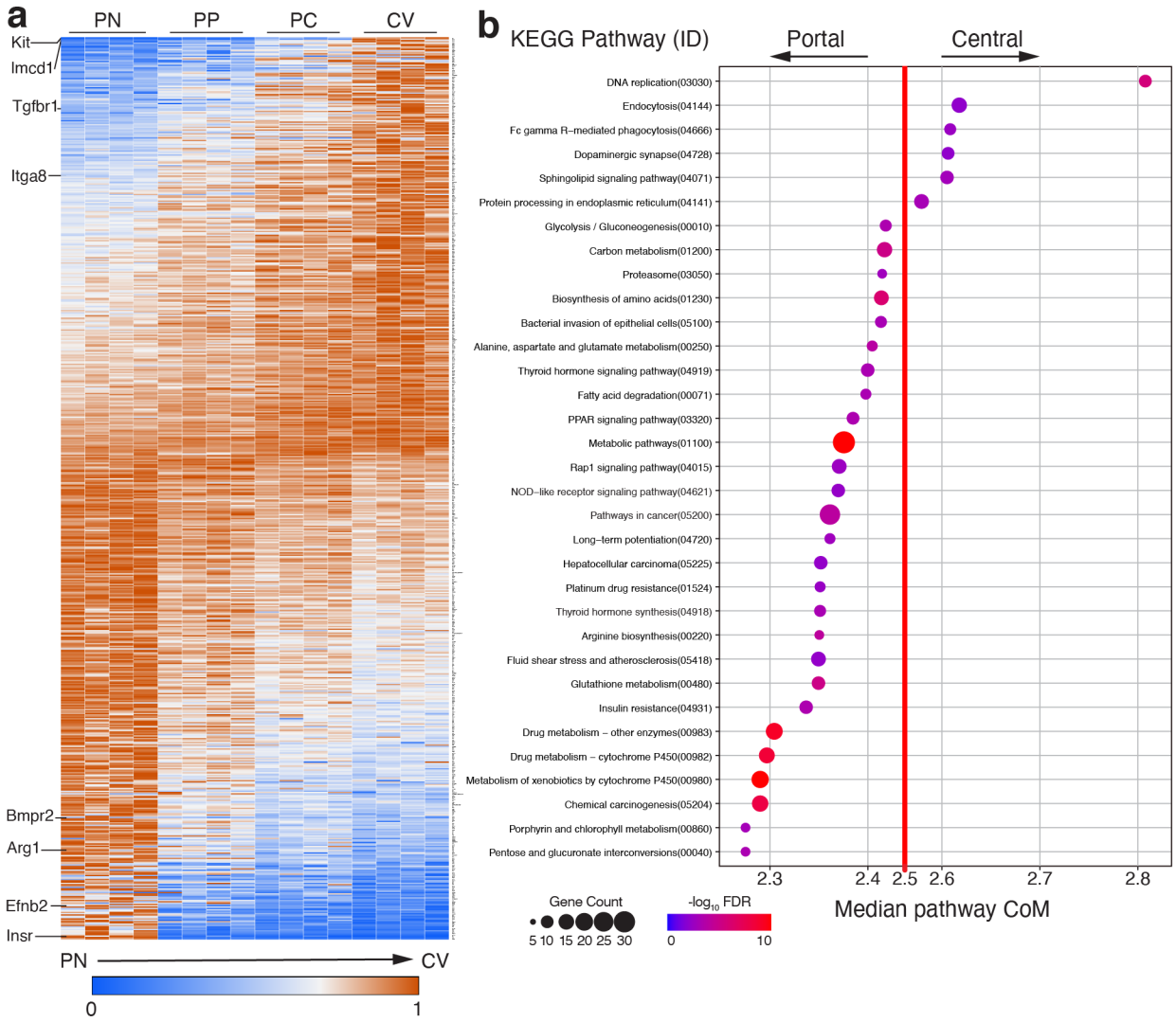

Figure 15. L-EC proteome zonation from portal to central. (a) Heat map representation of the expression profiles of 688 proteins significantly zonated on portal or central side. Proteins are normalized to their maximum LFQ value and sorted by their Centre-of-Mass. **(b)** Dot plot of the KEGG pathways significantly enriched in portal or central. Pathways (Y axis) are ordered from portal to central by increasing median Centre-of-Mass (X-axis) of the proteins enriched in the pathway. Dot size and colour indicate gene count and -log10 FDR, respectively.

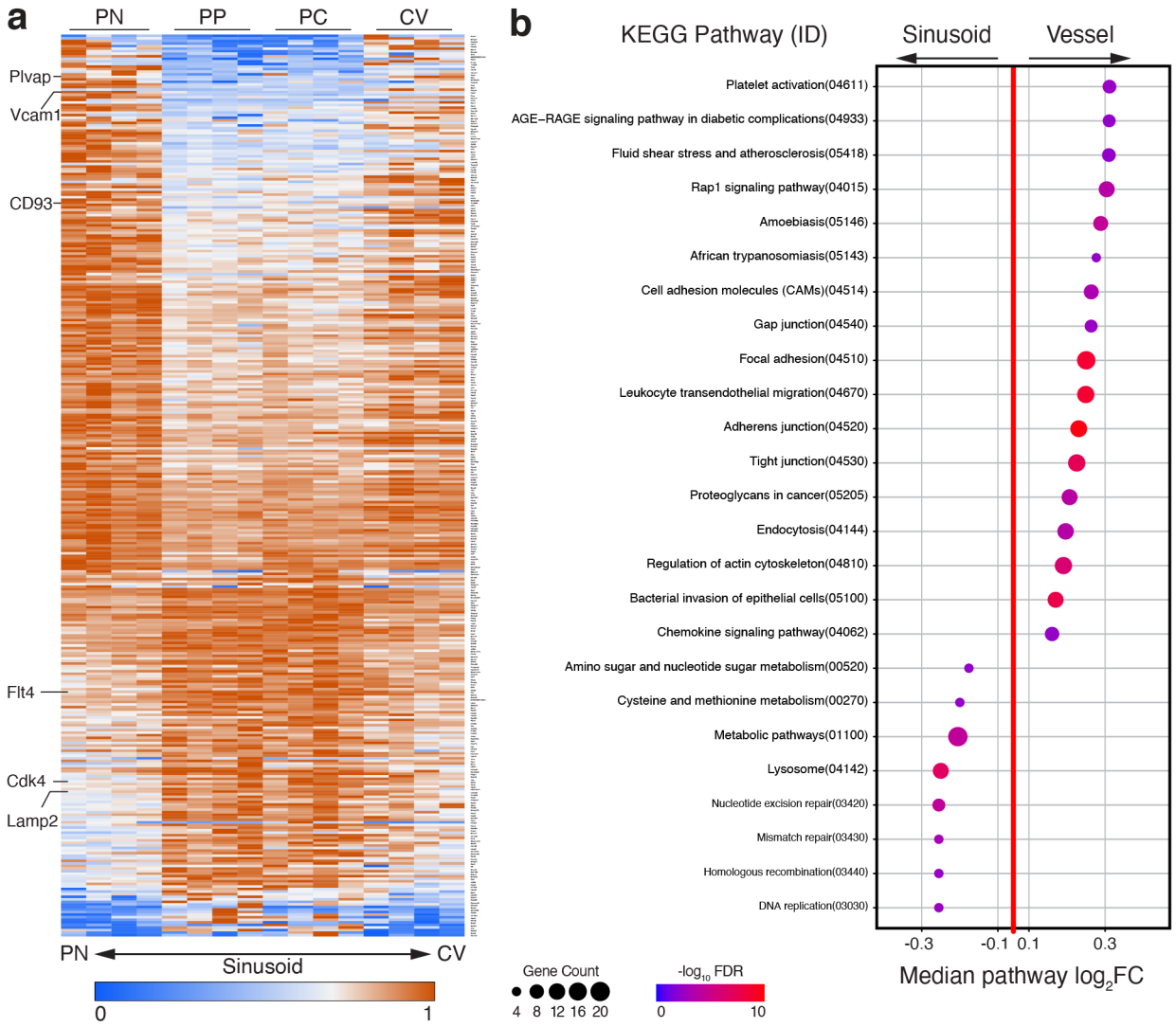

Figure 16. L-EC proteome zonation of vessels versus sinusoids. (a) Heat map representation of the expression profiles of 352 proteins significantly zonated on vessels or sinusoids. Proteins are normalized to their maximum LFQ value and sorted by their vessel to sinusoid log2 fold change. **(b)** Dot plot of the KEGG pathways significantly enriched on vessels or sinusoids. Pathways (Y axis) are ordered from sinusoids to vessels by increasing median log2 fold change (X-axis) of the proteins enriched in the pathway. Dot size and colour scale indicate gene count and -log10 FDR, respectively.

2.3.2 Correlation of translation and transcription

Cells need to express genes at the appropriate protein copy number to exert proper function, which is regulated by synthesis (transcription and translation) and decay (dilution and degradation). Both transcription and translation are energy demanding processes and it was reported that transcription and translation rates vary in a 1000-fold range while in comparison, the decay rates vary only in a 10-fold range (Hausser et al., 2019). It is generally thought that the transcriptome reflects the proteome. To validate this in our datasets, I correlated the proteomic and transcriptomic results, yielding a total of 4,169 protein-mRNA pairs that were quantitatively analysed. Indeed, there was a positive correlation of mRNA and

protein abundance ($r_{PEARSON}$= 0.378, p-val < 2.2 x 10^{-16}; Figure 17a). However, similar transcript abundance could correlate with protein abundance in a range of 2^{10}-fold, reflecting the huge difference of synthesis and/or decay for different proteins (Figure 17a). The distribution of Protein-to-Transcript-Rate (PTR) followed a Gaussian distribution, with a shift towards high PTR (Figure 17b). Here, the high PTR and low PTR range were defined as one standard deviation (SD) distance to the median value of all PTR pairs (Figure 17b). Previous studies reported a depletion of genes that combine high transcription and low translation due to a trade-off between precision and economy, as high transcription decreases stochastic fluctuations but increases transcription cost (Hausser et al., 2019). This is also reflected our data that there are almost 3-fold more proteins in PTR high range in comparison to low PTR range.

Next, the low and high PTR protein were subjected to pathway (Figure 17c) and protein interaction network analysis (Figure 18). Notably, among the low PTR proteins, “ribosome pathway” was enriched (Figure 17c). Furthermore, these ribosome component proteins formed a distinct cluster in the protein network (Figure 18a). While housekeeping genes like ribosomal components were reported to have stable proteins and mRNAs (Schwanhausser et al., 2011), this unexpected low PTR ratio could be indicative of a large RNA reserve for ribosomal proteins to ensure their proper functionality. On the other hand, the proteins involved in metabolism and biosynthesis (Figure 17c and 18b) were enriched in the PTR high range, implying optimized translational rates and/or protein stability to facilitate fast cellular adaptation.

To compare if the overall regulation from RNA to protein was consistent along the portal-to-central axis of the liver lobule, the Centre-of-Mass (CoM) values of mRNA and protein were compared (Figure 19a). Representative expression patterns are shown in Figure 19b, and the difference of the CoM (ΔCoM) between each protein-mRNA pairs are presented in the figure. Although one quarter to one third of the protein or mRNA was zonated along the liver lobular axis, more than 90% of the protein-mRNA pairs had consistent expression patterns. This indicated that for most individual genes, the post-transcription regulations were consistent along the lobular axis, whereas a small fraction (~8%) of the proteins were subjected to more divergent regulation.

2.4 Phosphoproteome of spatially sorted L-EC

The function of many proteins, most notably of molecules involved in signalling, is not primarily regulated by their abundance, but rather their activation state, which is determined by post-translational modifications (PTM), such as protein phosphorylation (Huttlin et al., 2010). Due to technical limitations and the reversible and substoichiometric nature of signalling events, deep phosphoproteomic analysis remains challenging, particularly when tissue dissociation is a pre-requisite for analysis. Applying the dedicated spatial L-EC isolation workflow (Methods), phosphoproteomic analyses were performed on the same samples that had been employed to establish spatial transcriptomic and proteomic zonation maps. In total, 19,607 phosphosites (p-site) were identified and the class I p-sites have been mapped to 3,447 proteins (Figure 6). Thus, this approach enabled the establishment of the most comprehensive *in vivo* phosphoproteomic map of endothelium.

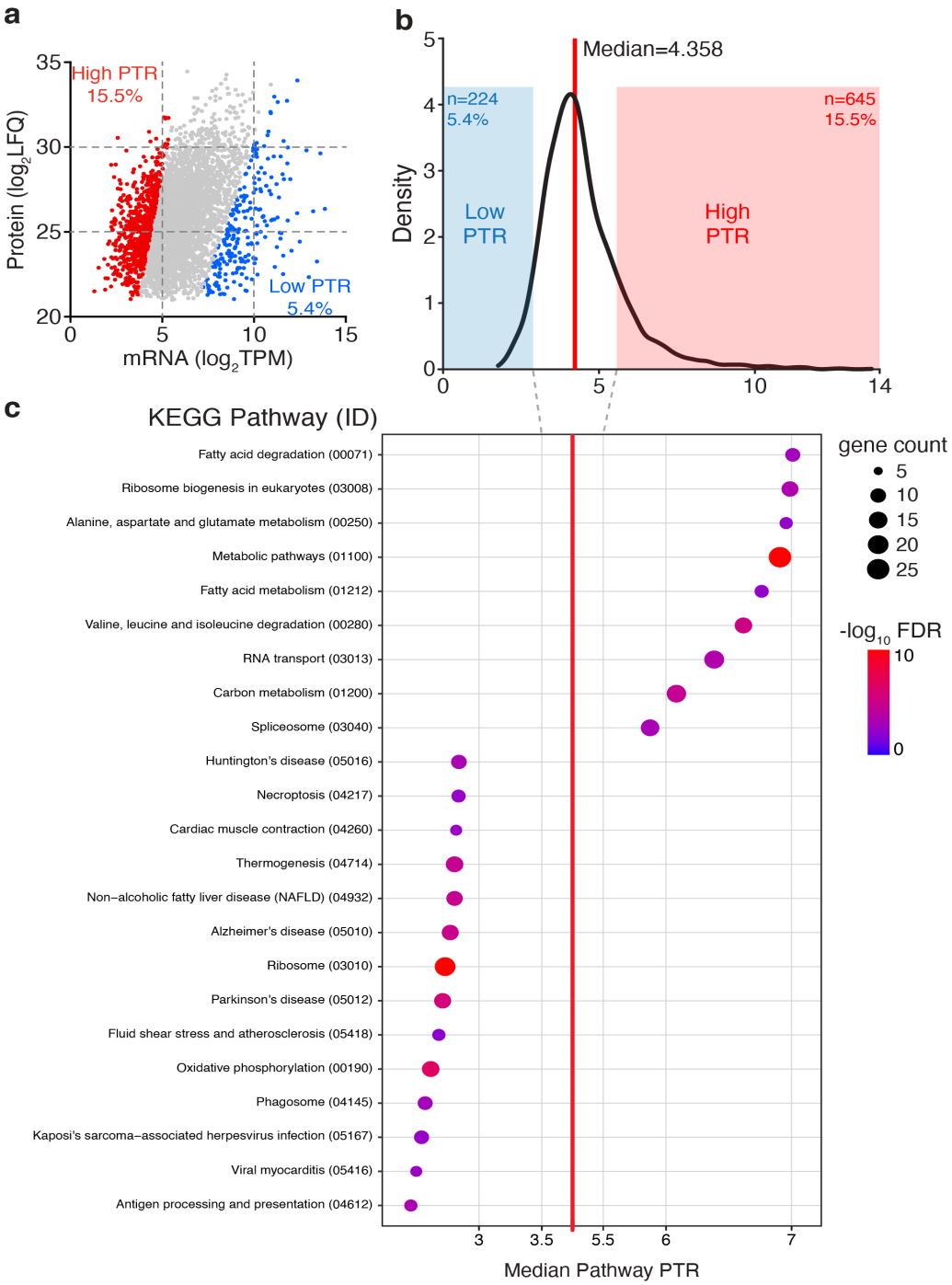

Figure 17. Protein to RNA correlation. (a) Scatter plot of the correlation of 4,169 protein-RNA pairs. Protein or RNA abundance was log2 transformed. Red and blue mark the genes with high and low PTR. **(b)** Distribution of protein-to-transcript ratio (PTR) values of the protein-RNA pairs. The red line indicates the median, the red and blue overlay display ±1 SD from the median to define high and low PTR (Methods). **(c)** Dot plot of the KEGG pathways significantly enriched in the gene sets corresponding to low or high PTR. Pathways (Y axis) are ordered from low to high PTR by increasing median PTR value (X-axis) of the proteins enriched in the pathway. Dot size and colour indicate gene count and -log10 FDR, respectively.

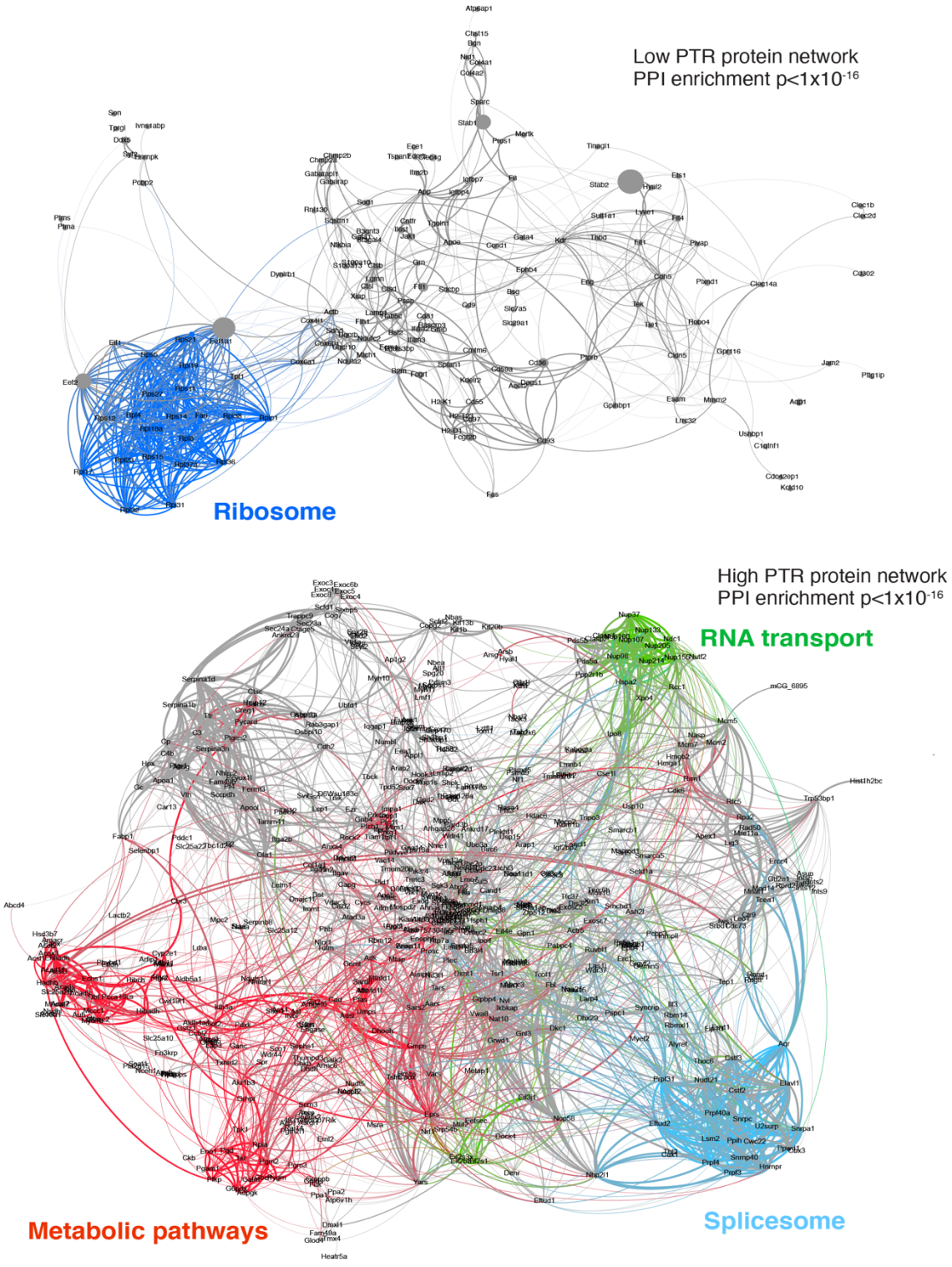

Figure 18. Protein interaction networks. Protein interaction network visualization of low **(a)** or high **(b)** PTR proteins. Node size is proportional to the protein abundance (LFQ) and the edge weight is proportional to the combined interaction score. Proteins (node) and the related interaction (edge) belonging to the indicated pathways were highlighted with different colours.

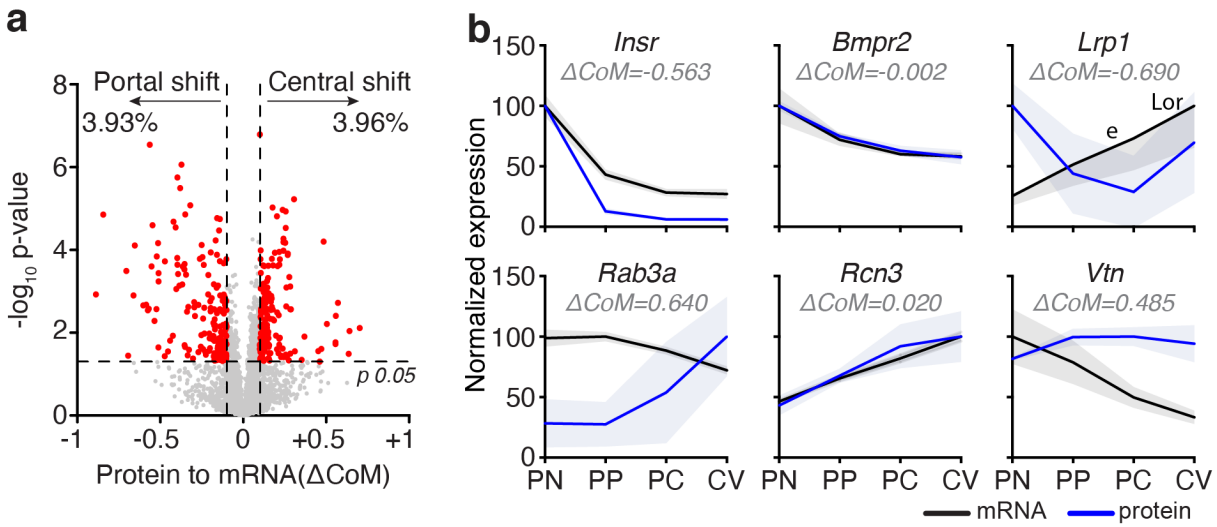

Figure 19. Zonation pattern change from protein to RNA. (a) Scatter dot plot of the ΔCoM (zonation shift) and the log10 p-value of 4,169 RNA-protein pairs. Red dots mark significantly shifted genes. **(b)** Expression profiles of the indicated pairs of proteins (blue) and RNA (black). Expression in percentage of maximum; patches represent SD.

2.4.1 Phosphosite motif analysis

Although measurement of thousands of phosphorylation site by mass spectrometry was achieved as demonstrated by this and other studies, the understanding of the kinase-substrate is still limited. Currently, only 5% of the phosphosites identified in phosphoproteome have related kinases and the functional assignment to these phosphosites is almost negligible (Needham et al., 2019). In general, each kinase preferentially phosphorylates substrates with a particular phosphorylation motif (Sugiyama et al., 2019). Therefore, I performed motif analysis on p-sites with high-confident localization scores (>0.75, class I) separately for phospho-serine (p-S), phospho-threonine (p-T) and phospho-tyrosine (p-Y). In total, 116 motifs were identified, belonging to four categories (proline-directed, acidic, basic and other). The distribution of the motif categories is shown in Figure 20a, and revealed a substantial difference among the three p-site, especially for p-Y. Interestingly, while most p-S sites were associated with a motif, more than one-third of the p-Y sites was not. This may result from the sparsity of identified p-Y in the dataset (3.3%), or the intrinsic sequence divergency. In addition to that, consensus sequences were extracted for each category and revealed high similarities between phospho-Serine (p-S) and phospho-Threonine (p-T) and marked discrepancies to phospho-Tyrosine (p-Y) (Figure 20b), likely reflecting substrate differences between Serine/Threonine- and Tyrosine-kinases. Notably, the consensus sequence from 'other' motifs of p-Y was reminiscent of acidic motifs, indicating a possible acidic prone tropism of the L-EC Tyrosine-kinome.

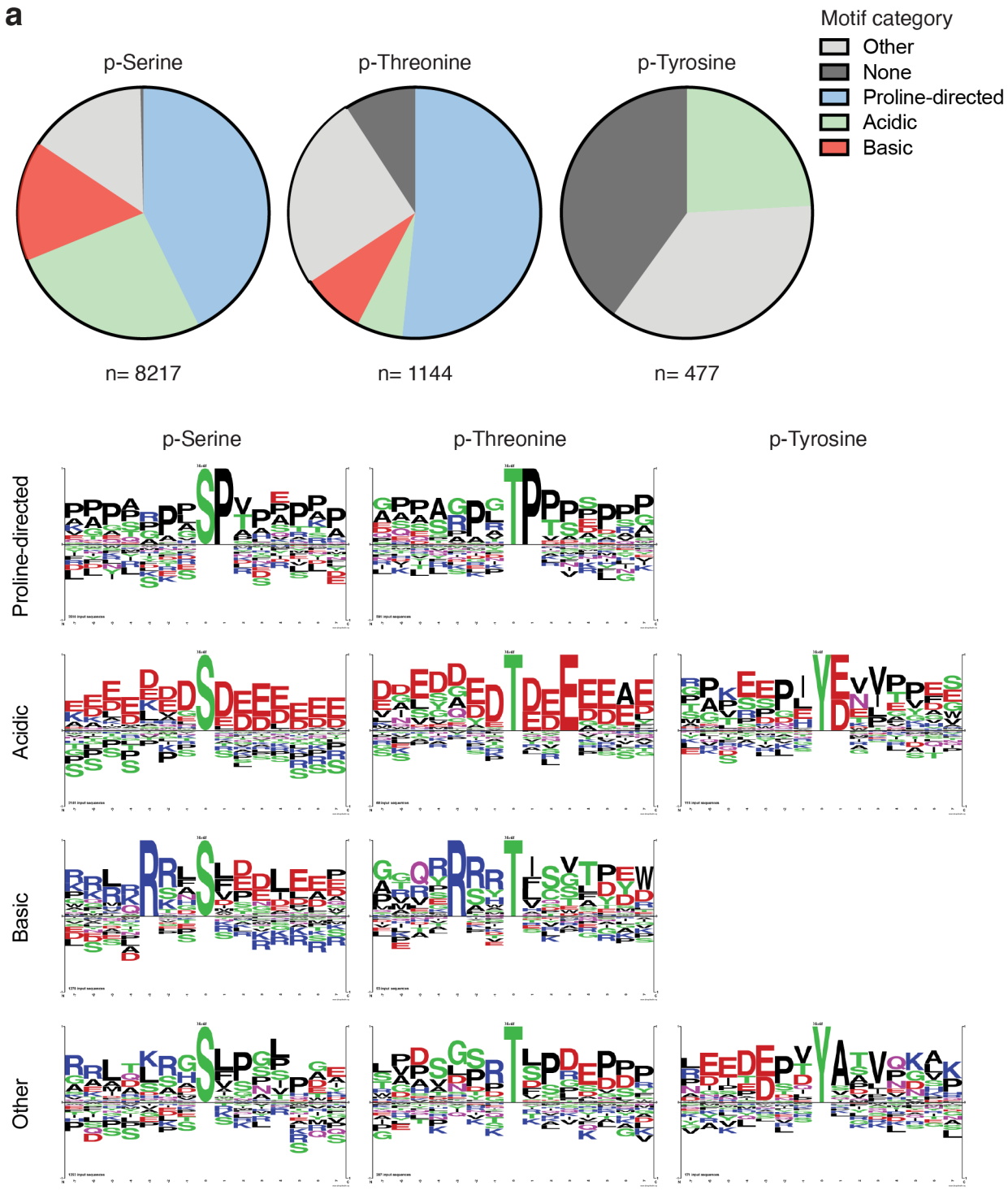

Figure 20. Phosphorylation motif analysis of the p-S, p-T and p-Y sites. (a) Pie charts showing the proportion of proline-directed, acidic, basic and other motif categories for phosphorylated Ser (p-S), Thr (p-T) and Tyr (p-Y) residues. Only class I P-sites (localization score >0.75) were considered. "None" indicates sequences not associated with any motif. **(b)** Motif logos of consensus sequences surrounding p-S, p-T and p-Y for proline-directed, acidic, basic and other motifs classified in a (Methods).

2.4.2 Comparison of phosphorylation with protein expression

Phosphopeptides (p-peptide) represent only a small fraction in cells. Therefore, before the mass spectrometry measurement, IMAC-based p-peptide enrichment was performed with the AssayMap Bravo platform (Agilent) by M. Komeili at University of Strasbourg. For quality control, as suggested by the CFMP at the ZMBH, I have included an internal control containing a mixture of digested peptides from all zones. This internal control was medium-dimethyl labelled and spiked equally to the samples which were light-dimethyl labelled. The obtained results, thus, represented the expression ratio of sample-to-control, instead of abundance as for mRNA or protein. Nevertheless, the relative expression patterns along the portal-central axis were retained with this methodology. I performed an imputation under normal distribution and subsequent batch normalization before analysing the spatial distribution of the phosphoproteome. Here, only class-I p peptides were analysed, revealing significant zonation for 25% of the identified peptides (Figure 21a), which was in line with overall protein zonation.

Similar to the protein-mRNA pairs, CoM values of the p-peptides and their respective protein were compared (Figure 21b and c). Interestingly, out of the 7,520 p-peptide-protein pairs, a significant zonation shift for 16% of the pairs could be observed, compared to 8% observed for protein-RNA pairs. This indicated that differential phosphorylation along the sinusoid serves as a major regulator of protein function.

2.4.3 Zonated domains in phosphorylated proteins

Protein domains are the structural, functional, and evolutionary units of proteins, which can exist and fold independent of the rest of the protein chain (Yu et al., 2019). Phosphorylation is an energy demanding reaction, which in most cases leads to protein activation. Therefore, the proteins with zonated phosphorylation were subjected to analysis for functional domain enrichment. Distinct domains were enriched in portally or centrally zonated proteins as shown in Figure 22, indicating differentially regulated protein interaction and signalling networks along the sinusoids. However, several domains were found to be enriched in both directions, for instance, calponin homology (CH) domain, which is critical for stability and organization of the actin cytoskeleton, calcium mobilization and activation of downstream pathways (Yin et al., 2020). It would be interesting for future studies to compare this dataset to those from other liver cell populations or other vascular beds to understand whether these domains are involved in L-EC specific functions. Particularly, the protein kinase catalytic domains are of note, which are more directly related to the p-sites identified in this study: Serine/threonine protein kinases, catalytic domain (S_TKc) were enriched on both sides, while tyrosine kinases, catalytic domain (TyrKc), were strongly zonated in central area, which could indicate a possible substrate zonation.

2.4.4 Peri-central zonation of phospho-tyrosine

The zonation of protein kinase catalytic domains prompted a more thorough analysis on their substrates. Phosphorylation occurred almost exclusively on serine (S), threonine (T) and tyrosine (Y) residues (Sharma

et al., 2014). Therefore, I plotted the respective zonated p-sites separately. As shown in Figure 23a-b, the overall zonation distribution of p-S and p-T was spread evenly from portal to central in a similar fashion as observed for RNA and protein zonation. In stark contrast to that, p-Y (Figure 23c) is almost exclusively zonated on central vein.

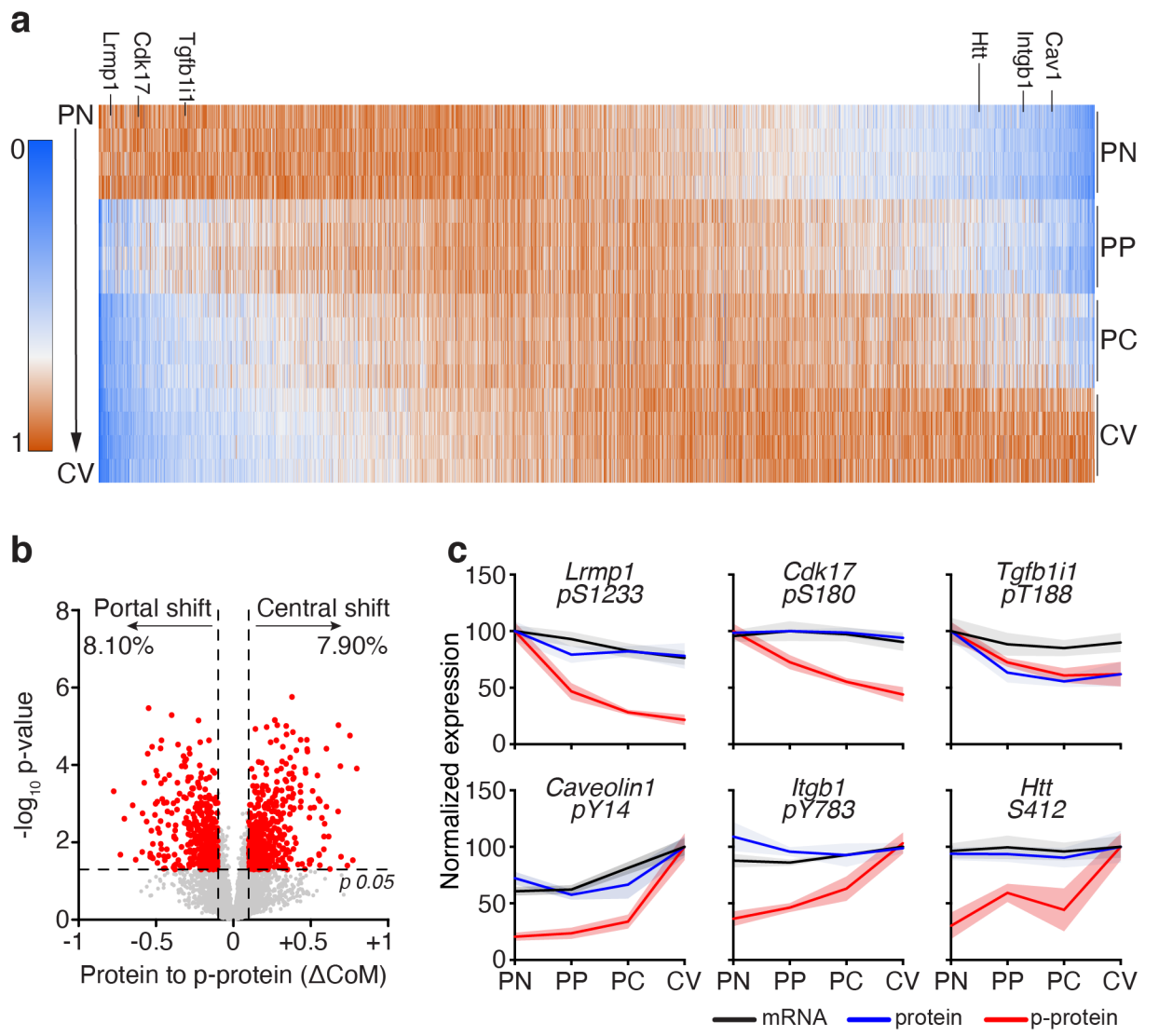

Figure 21. Zonation of the phosphosites. (a) Heat map representation of the expression profiles of 2,828 zonated p-peptides. P-peptides are normalized to their maximum expression and sorted by Centre-of-Mass. **(b)** Scatter dot plot of the DCoM and the log10 p-value of 7,520 p-peptide-protein pairs. Red dots mark significantly shifted proteins. **(c)** Expression profiles of the indicated matches of p-peptides (red), proteins (blue) and RNA (black). Expression in percentage of maximum; patches represent SD.

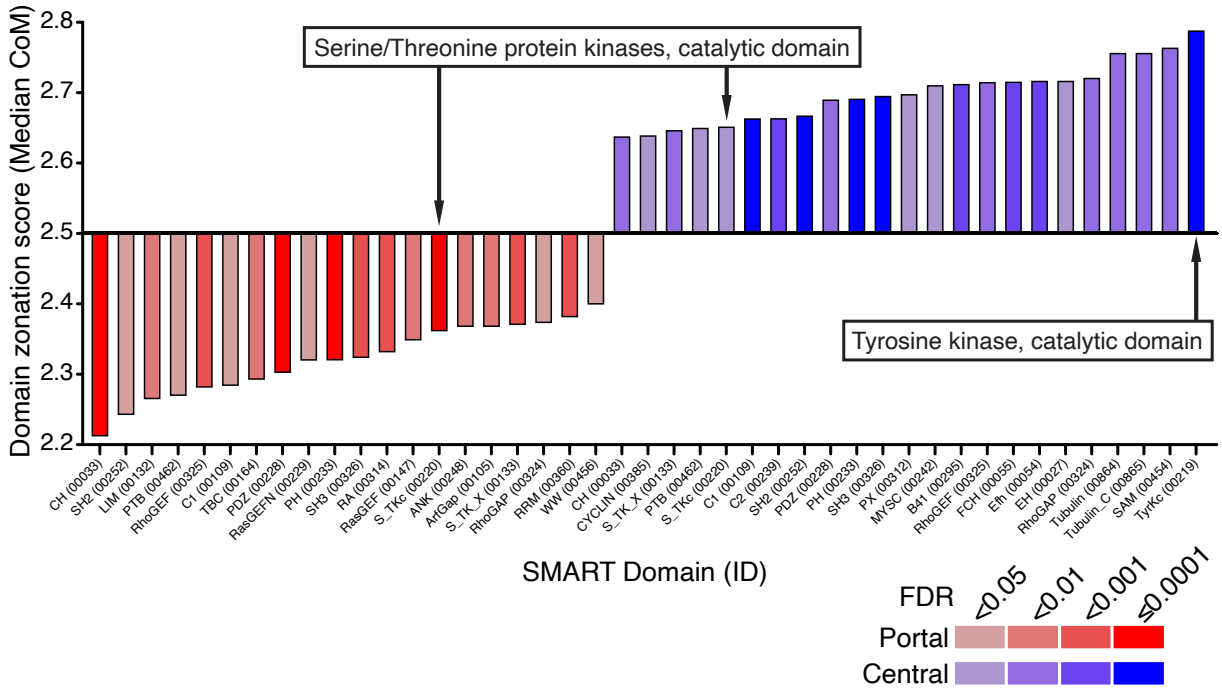

Figure 22. Domains enriched in L-EC zonated phosphoproteins. Bar graph of the SMART protein domains significantly enriched in portal (red) or in central (blue) zonated phosphoproteins. Domains (X-axis) are ordered median Centre-of-Mass (Y-axis) of the proteins enriched for the domain. Bar colour indicates the FDR range.

In general, zonation of p-sites can result from (i) zonated protein abundance with similar phosphorylation stoichiometry, (ii) similar protein abundance with zonated phosphorylation stoichiometry, or (iii) combination of both. To examine which was the major contributor for the p-Y zonation, all the zonated p-sites were plotted with their corresponding proteins and mRNAs (Figure 24). I observed that most of the p-Y had a zonated phosphorylation stoichiometry shifting towards the central side (Figure 24 and 25a). This was confirmed by comparing the CoM from the p-sites and their corresponding proteins, which revealed a significant difference (Figure 25b).

To further expand this observation in zonated p-sites, all the identified p-sites were taken into account for analysis. As most of the p-sites were not zonated, each of them was assigned to one of the four zones (PN, PP, PC, CV) depending on where maximal expression was located. Next, the distribution of p-S, p-T, and p-Y was analysed for each zone, represented in Figure 26a as combined experiments and in Figure 26b as individual experiments. The distribution of the three p-sites was similar in PN, PP, and PC: ~88% for p-S, ~10% for p-T and ~2% for p-Y. In contrast, in CV, p-Y reached ~10% with a corresponding decrease of p-S to ~80%. Taken together, the phosphorylation of tyrosine sites was over all strongly zonated on the central side, which was largely independent of protein abundancy.

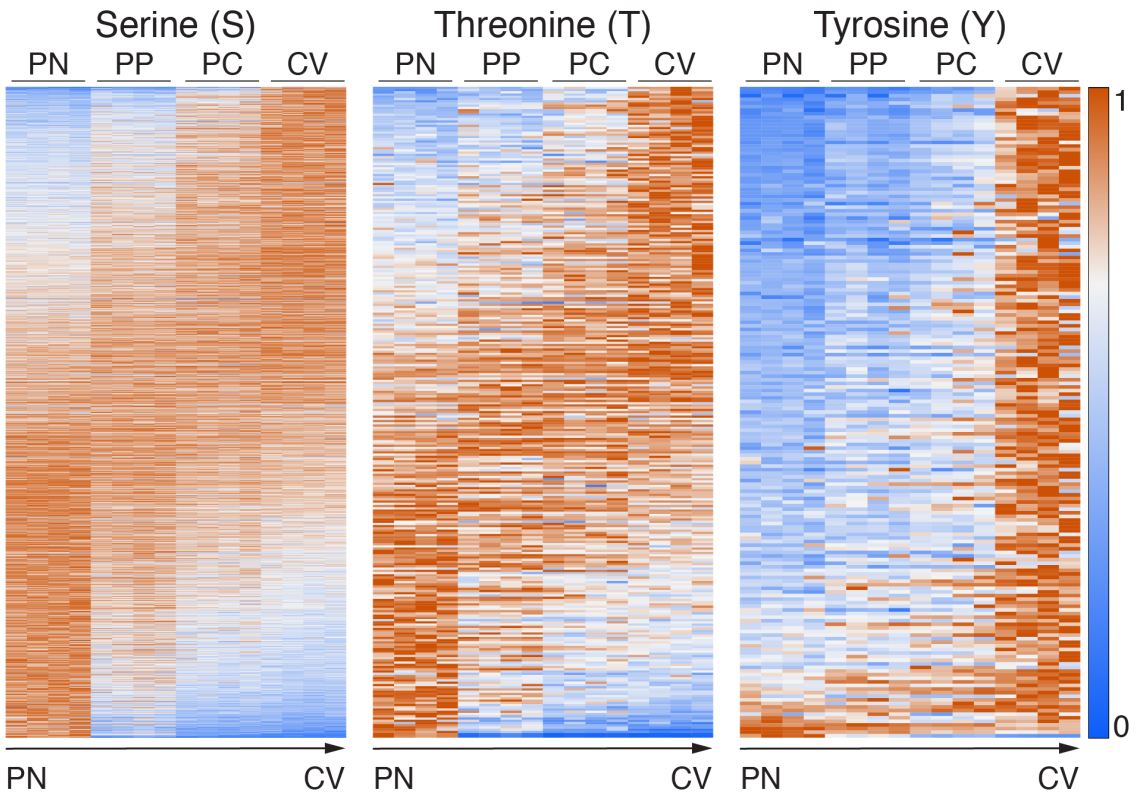

Figure 23. Phosphosite specific analysis. Separated heat map representation of significantly zonated phospho-serine (p-S), phospho-threonine (p-T), and phospho-tyrosine (p-Y). P-Peptides are normalized to their maximum expression and sorted by their Centre-of-Mass.

2.4.5 Central zonation of receptor tyrosine kinases (RTK)

As previously observed that the tyrosine kinase catalytic domain and consistently also p-Y was enriched on central side, the tyrosine kinase family was further examined. I performed the phylogenic analysis considering the corresponding genes of the zonated phosphopeptides, revealing that in L-EC, the TK family was the most abundant kinase family and that their phosphorylation was mostly zonated on the central side (Figure 27a). The phosphorylation patterns for the most well-known RTKs are shown in Figure 27b, including the VEGFRs, the Tie receptors, cKit and Ephrin receptor. To confirm these observations, immune-based phospho-RTK array was performed on spatially sorted L-EC, which clearly demonstrated the overall central zonation of RTK phosphorylation (Figure 28). It was quite intriguing that the angiopoietin receptors Tie1 and Tie2/TEK were identified among the top zonated p-proteins, whereas in contrast to that, their mRNA and protein abundance was rather homogenous along the axis of the liver lobule. This suggested a highly localized activation of this pathway and possibly pointed towards a regulatory role in liver zonation.

Part-a

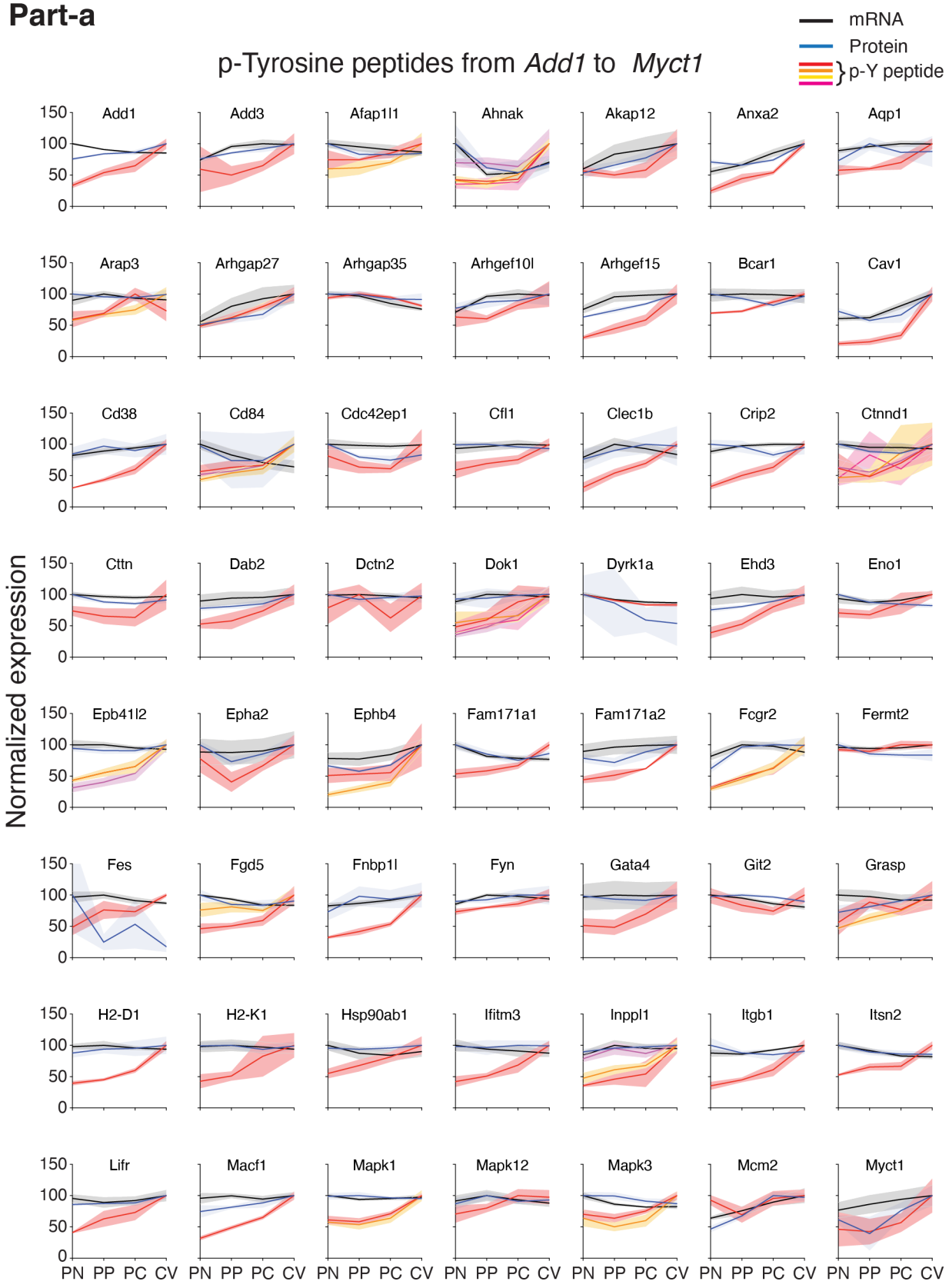
mRNA
Protein
p-Y peptide
p-Tyrosine peptides from *Add1* to *Myct1*
Normalized expression
Add1
Add3
Afap1l1
Ahnak
Akap12
Anxa2
Aqp1
Arap3
Arhgap27
Arhgap35
Arhgef10l
Arhgef15
Bcar1
Cav1
Cd38
Cd84
Cdc42ep1
Cfl1
Clec1b
Crip2
Ctnnd1
Cttn
Dab2
Dctn2
Dok1
Dyrk1a
Ehd3
Eno1
Epb41l2
Epha2
Ephb4
Fam171a1
Fam171a2
Fcgr2
Fermt2
Fes
Fgd5
Fnbp1l
Fyn
Gata4
Git2
Grasp
H2-D1
H2-K1
Hsp90ab1
Ifitm3
Inppl1
Itgb1
Itsn2
Lifr
Macf1
Mapk1
Mapk12
Mapk3
Mcm2
Myct1
150
100
50
0
PN PP PC CV

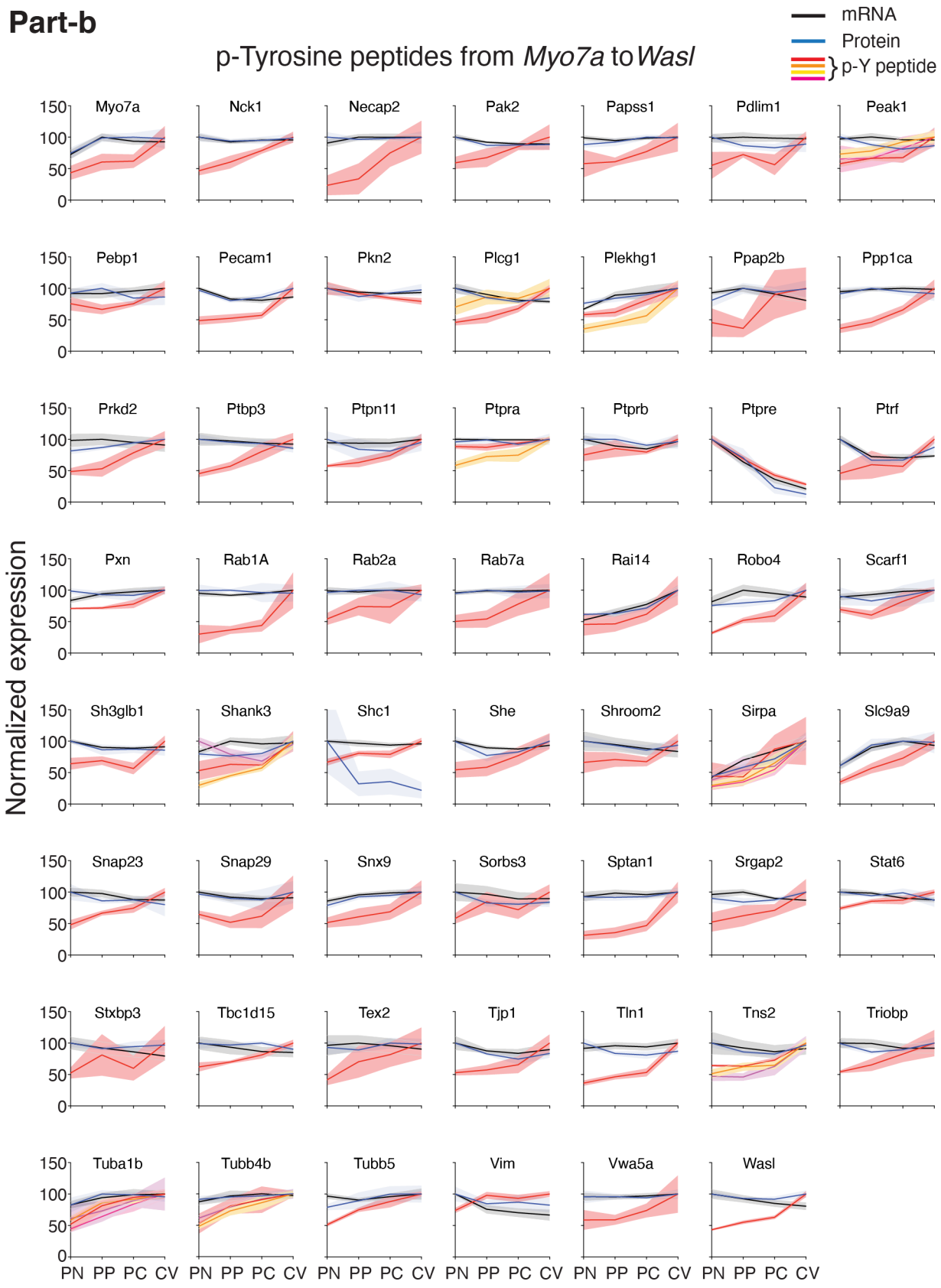
Part-b
p-Tyrosine peptides from Myo7a to Wasl
mRNA
Protein
p-Y peptide
Normalized expression
Myo7a
Nck1
Necap2
Pak2
Papss1
Pdlim1
Peak1
Pebp1
Pecam1
Pkn2
Plcg1
Plekhg1
Ppap2b
Ppp1ca
Prkd2
Ptbp3
Ptpn11
Ptpra
Ptprb
Ptpre
Ptrf
Pxn
Rab1A
Rab2a
Rab7a
Rai14
Robo4
Scarf1
Sh3glb1
Shank3
Shc1
She
Shroom2
Sirpa
Slc9a9
Snap23
Snap29
Snx9
Sorbs3
Sptan1
Srgap2
Stat6
Stxbp3
Tbc1d15
Tex2
Tjp1
Tln1
Tns2
Triobp
Tuba1b
Tubb4b
Tubb5
Vim
Vwa5a
Wasl
150
100
50
0
PN PP PC CV

Figure 24. Expression profiles of zonated p-Y peptides and their corresponding RNA and protein. Plots of the Expression profiles of 154 significantly zonated p-Y peptides matched to proteins. Plots are arranged in alphabetical order of the respective gene names from Add1 to Myct1 (part-A), and from Myo7a to Wasl (part-B). Expression values are expressed as percentage of maximum; patches represent SD.

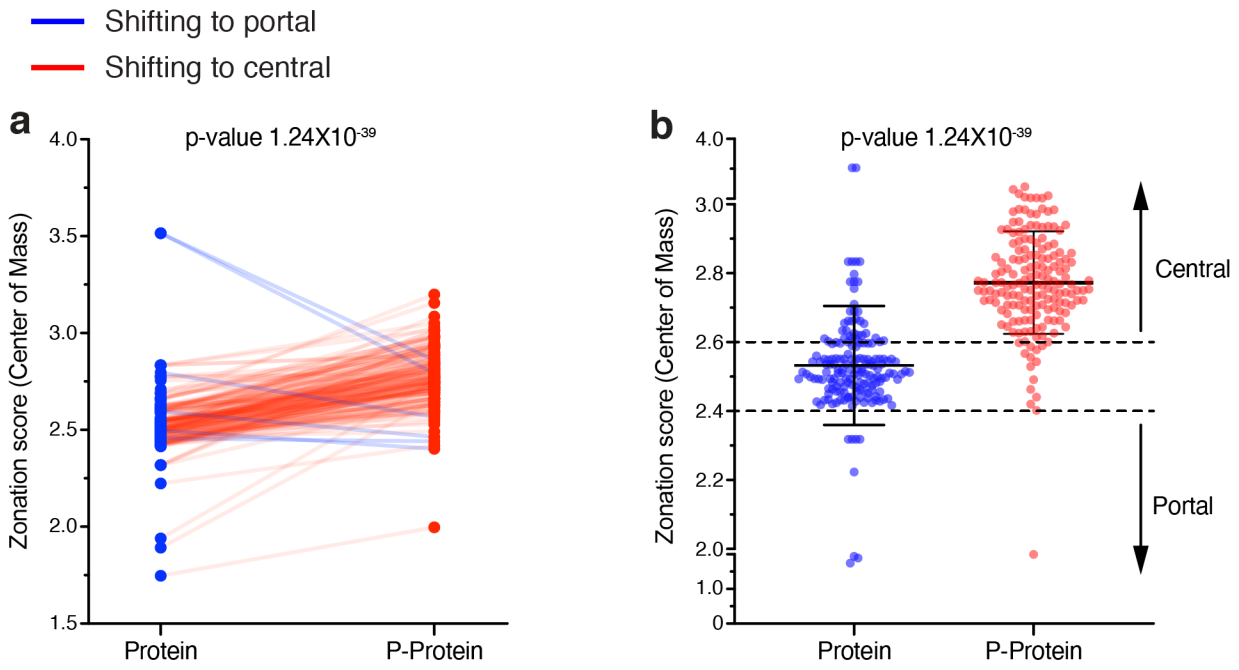

Figure 25. Variation of the zonation score of p-Y peptides and corresponding proteins. (a) Aligned dot plot of the CoM relative to p-Y peptides and corresponding proteins. Before-after connecting lines indicate a shift to central (red) or to portal (blue). **(b)** Scatter dot plot of the same groups represented in a. Data are represented as mean ± SD.

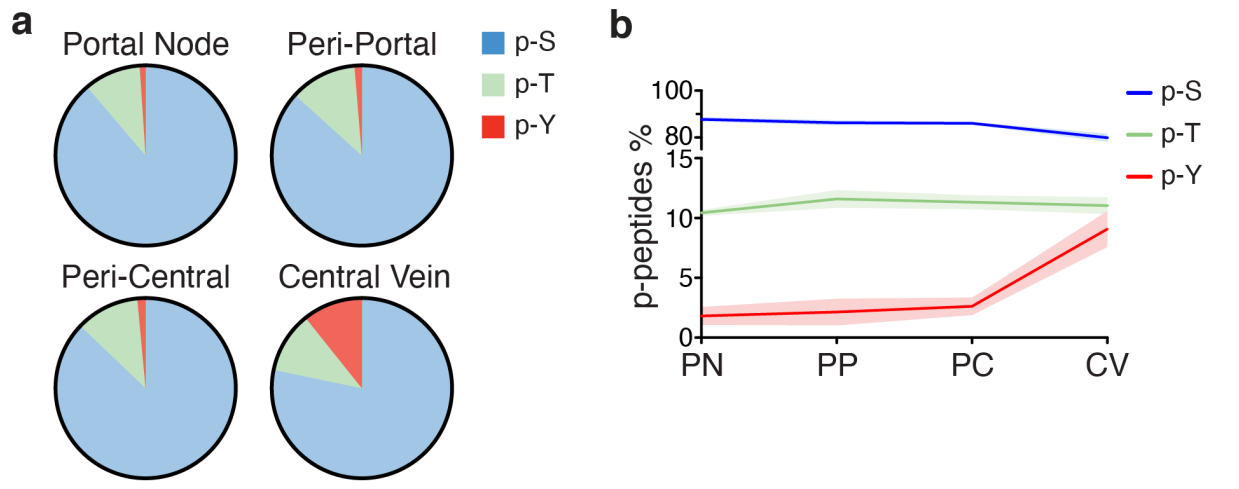

Figure 26. Distribution of p-site for each zone. (a) Proportion of p-S, p-T and p-Y for the indicated zone, assigning each p-peptide to one zone according to their maximum expression (mean value). **(b)** Proportion of p-S, p-T and p-Y for each biological replicate. Patches indicate SD.

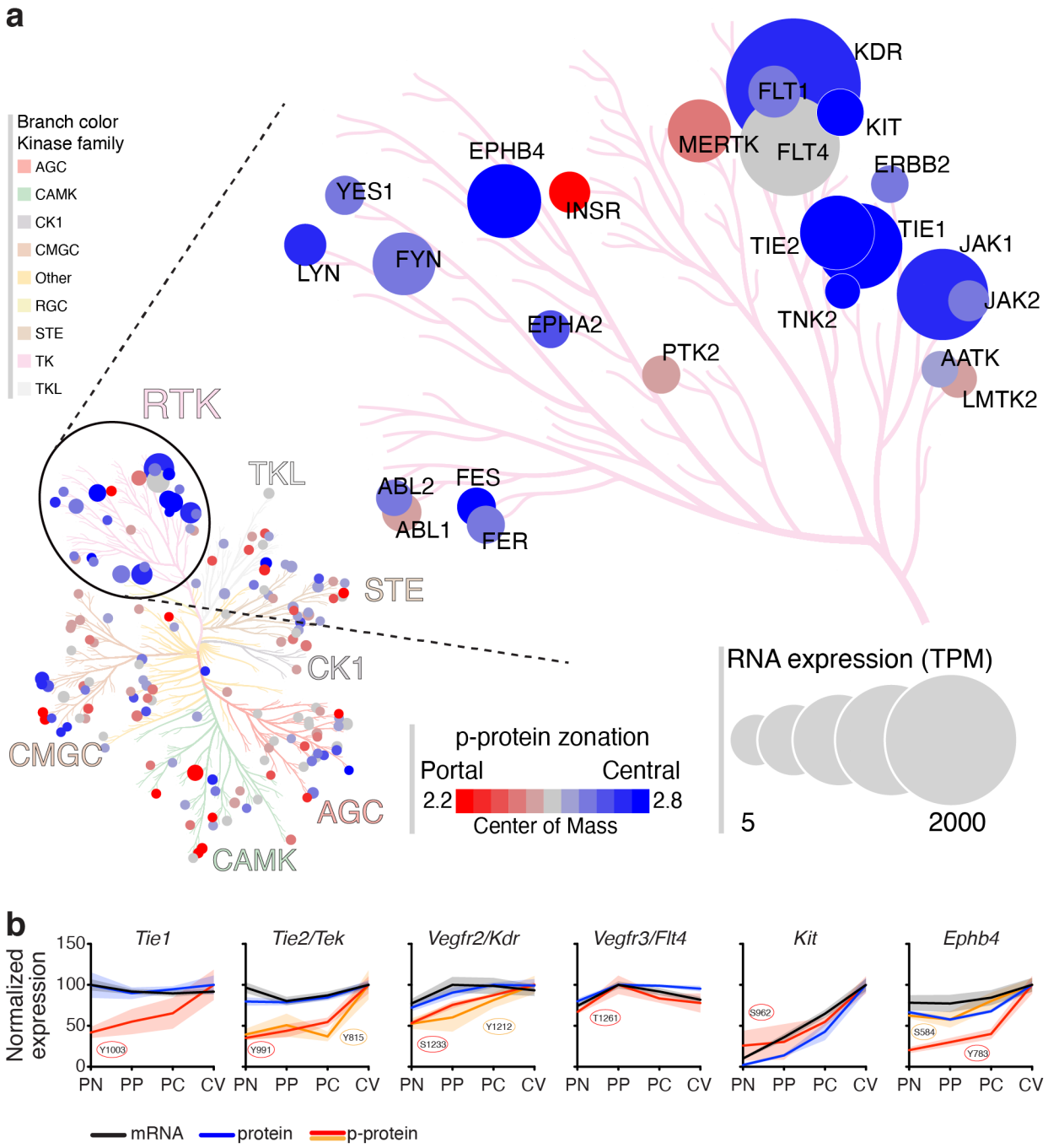

Figure 27. Zonation of phosphorylation of tyrosine kinase. (a) Kinome phylogenetic tree of phosphorylated kinases. Circle size proportional to TPM; colour representing phosphorylation zonation (CoM) from portal (red) to central (blue). **(b)** Expression profiles of matches of p-peptides (red or orange), proteins (blue) and RNA (black) for the indicated RTKs. Expression in percentage of maximum; patches represent SD.

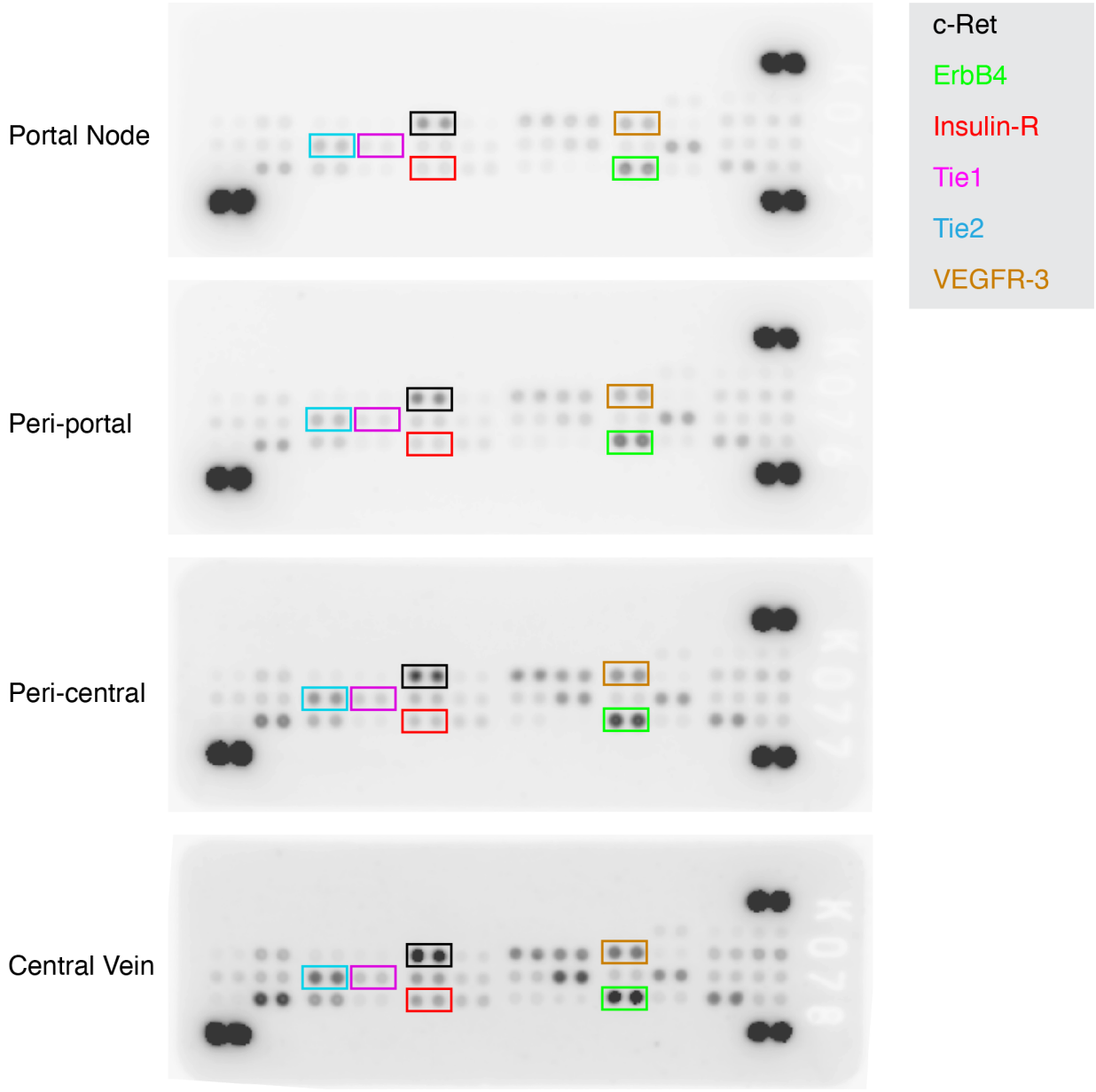

Figure 28. Phospho-RTK assay of spatially sorted L-EC. Dot-blot array analysis of L-EC spatially sorted from the indicated zones. Selected pRTKs are indicated by colour matched boxes. Spatial sorted L-EC was pooled from three C57BL/6N mice. Representative of two independent experiments.

2.5 Control of liver zonation and regeneration by the tyrosine kinase Tie1

2.5.1 Tie1 blockade preferentially regulates gene expression on central L-EC

The Tie1 receptor is indispensable during embryonic development and its role in liver fibrosis progression was recently characterized (Puri et al., 1995; Sato et al., 1995; Xu et al., 2019). In addition, a Tie1 blocking antibody (Tie1-39) was recently characterized in a preclinical model that could impede systemic metastasis and improve survival (Singhal et al., 2020). Considering its central activation, Tie1 was selected

as a prototypic molecule from the phosphoproteome screening for functional validation. C57BL/6N Mice were systemically treated with Tie1-39 and RNAseq analysis was performed on spatially sorted L-EC 2 hours after treatment. Here I did not pool mice for the samples as I could obtain sufficient amount of RNA for the bulk RNAseq and I have included four biological replicates for each zone. Compared to the RNAseq mentioned in earlier section (*1.9*), the Tie1 blockade induced a dysregulation of several genes across all zones, with a stronger effect on central zone gene expression, as evidenced by a 2-fold higher number of significantly regulated genes compared to the portal zone (Figure 29a). Furthermore, the regulation is overall stronger on central than portal as indicated by comparing the DESeq2 q-values of the regulated genes (q-val < 0.05 in portal and/or central zone), (Figure 29b). Together, these data suggested that Tie1 blockade had a more pronounced effect on central L-EC, which is in line with its central activation.

2.5.2 Tie1 signalling specifically regulates Wnt9b expression

Most notably, the central vein landmark gene Wnt9b was the top candidate gene regulated by Tie1 blockade (Figure 29a). QRT-PCR and RNA fluorescence *in situ* hybridization (FISH) validated this finding, revealing an almost completely shut-off of Wnt9b after Tie1 blockade and, hence, identifying the Tie receptor signalling as a novel regulator of vascular Wnt expression (Figure 30).

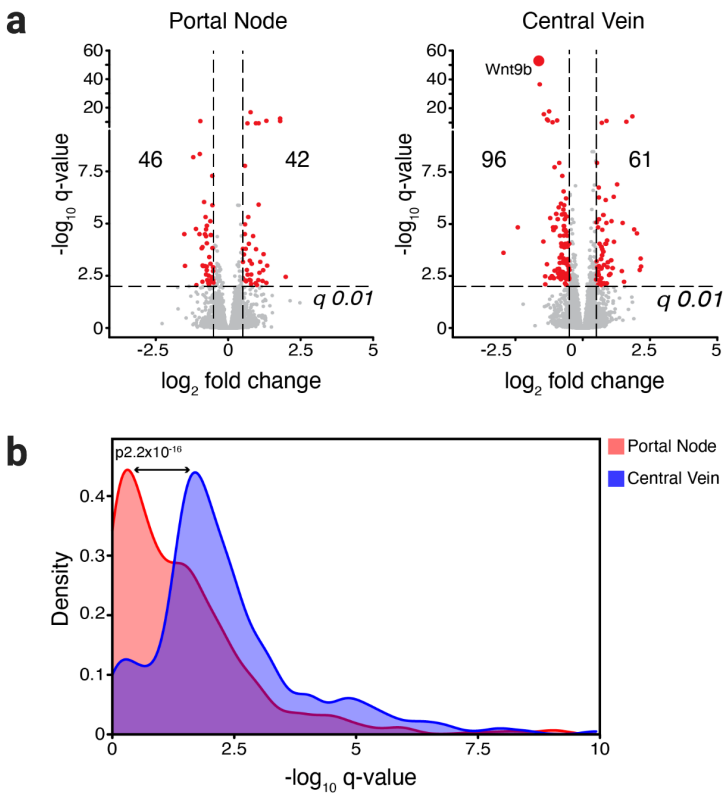

Figure 29. Tie1 blockade preferentially regulate gene expression on central L-EC. (a) Volcano plots of gene regulations induced by Tie1 blockade in spatially sorted L-EC from portal node (left) and central vein (right), respectively. Red dots mark the significantly regulated genes, indicated by the number in each square. **(b)** Histogram of the -log10 q-value distribution of regulated genes in portal node and central vein 2 h after Tie1 blockade. The effect of Tie1 blockade on PN and CV was compared by Wilcoxon matched-pairs signed rank test of the -log10 q-values. Four biological replicated were used in the analysis.

Central vein-derived Wnt ligands play a key role in the angiocrine regulation of liver zonation, targeting approximately one-third of the hepatocyte zonated genes (Ben-Moshe and Itzkovitz, 2019; Wang et al., 2015). Indeed, the EC-specific genetic inactivation of the Wnt signalling enhancer *Rspo3* abrogates hepatocyte zonation (Rocha et al., 2015).
The rapid regulation of L-EC *Wnt9b* expression consequently prompted the hypothesize that vascular Tie receptor signalling could act as key regulator of maintaining liver homeostasis in a Wnt signalling-dependent manner. To further characterize this regulation, I performed a temporal analysis of the Tie1 blocking antibody. Already 30 min after the treatment, slightly down-regulation of Wnt9b expression could be observed, which reached its peak 2-4 hours post treatment and thereafter slowly returned to physiological levels (Figure 31a). This surprisingly rapid regulation of Wnt9b is also indicative of a relative fast turnover rate of the gene.

Next, I asked the question whether Wnt9b regulation was Tie1 specific or due to a secondary effect from a systemic perturbance of homeostasis. In collaboration with Dr. Inverso, I applied antibody blocking of major EC signalling pathways in C57BL/6N mice and the expression of Wnt9b in the liver was analysed by qRT-PCR. As shown in Figure 31b-e, blockade of VEGFR-2, VEGFR-3, Dll4, integrins- αV, integrin-α5 or PECAM1 *in vivo* had a no effect on L-EC *Wnt9b* expression, further substantiating the specificity of Tie1-Wnt9b regulation.

2.5.3 Transcription factor FoxO1 and STAT3 directly regulate Wnt9b

The rapid response upon Tie1 blockade (Figure 31) suggested a direct transcriptional regulation of Wnt9b mediated by Tie1 signalling. Thus, I performed *in silico* analysis of the *Wnt9b* promoter region. The genomic region consisting -1000 to 1000 bp relative to the *Wnt9b* transcription start site was searched against the database of JASPAR Transcription Factor Motifs (Fornes et al., 2020). Among the putative transcription factors that could bind to Wnt9b promotor, FoxO1 and STAT3 were of high relevance (Figure 32a), as both were reported to be regulated by Angpt/Tie pathway (Kim et al., 2016; Korhonen et al., 2016; Korpelainen et al., 1999). However, phosphorylation of FoxO1 and STAT3 has distinctly opposing functional consequences: whereas STAT3 phosphorylation promotes nuclear translocation and STAT3-dependent transcription, FoxO1 phosphorylation leads to nuclear exclusion and inactivation of FoxO1-dependent transcription (Figure 32b)(Farhan et al., 2017; Huynh et al., 2019).
The potential involvement of both STAT3 and FoxO1, consequently suggested a fine-tuned balance of these transcription factors in Tie receptor signalling mediated regulation of Wnt9b expression. Therefore, Wnt9b expression was analysed in mice after EC-specific conditional genetic knockout of *Stat3* (refered as STAT3^{iECKO}, Figure 33a) or *Foxo1* (refered as FoxO1^{iECKO}, Figure 33b). Indeed, *in vivo* inactivation of Stat3 significantly downregulated Wnt9b expression whereas Foxo1 knockout induced upregulation of Wnt9b (Figure 33c and d), adding further evidence to their function as Wnt9b transcription regulators: STAT3 promoted Wnt9b transcription, whereas FoxO1 acted as a Wnt9b transcriptional repressor.

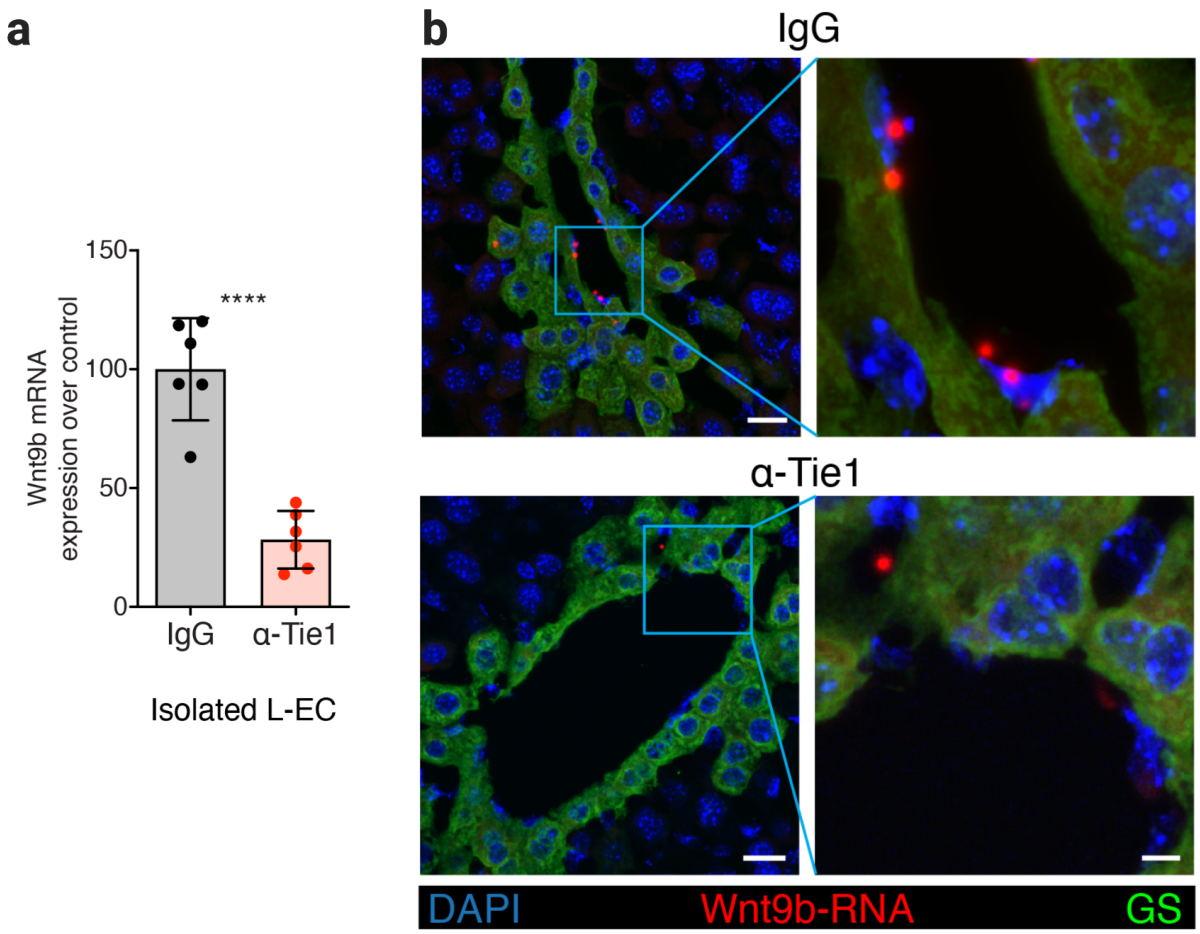

Figure 30. Tie1 blockade almost shut off L-EC derived Wnt9b expression. (a) qRT-PCR analysis Wnt9b mRNA expression from freshly isolated L-EC 2 h after IgG (grey bar) or anti-Tie1 (red bar) administration in C57/B6 mice. n = 6, each mouse was represented as a single dot. **(b)** Wnt9b RNA visualized by FISH staining (red) 2 h after injection of anti-Tie1 antibody (compared to IgG control). The central vein area is visualized by staining for glutamine synthetase (GS, green). Staining was performed on the same samples as in (a) and representative images were shown. Scale bar: 20 µm (left), 5 µm (right).

2.5.4 Functional relevance of Tie-Wnt axis in liver regeneration

Next, to assess the functional contribution of the Tie-Wnt signalling axis, the most commonly used model for the study of liver regeneration, namely 2/3 partial hepatectomy (PHx) were performed. The liver possesses an remarkable regenerative potential as the differentiated liver cells can enter the cell cycle in response to tissue loss and divide until the original liver mass is restored (Fausto et al., 2006). L-ECs actively control this regenerative process as a dynamic rheostat, spatiotemporally orchestrating hepatocyte and L-EC proliferation (Ding et al., 2010; Hu et al., 2014). In collaboration with Dr. Inverso, I performed PHx on mice with endothelial-specific conditional inactivation of Tie1 (referred as Tie1^{iECKO}) and two days later, sacrificed the mice for subsequent analysis (Figure 34a and b). The expression of Wnt9b and Wnt2 was significantly reduced in liver lysates of PHx mice compared to control littermates. This

down-regulation was specific for these L-EC-expressed Wnt ligands and not observed for non-endothelial Wnt ligands, including Wnt2b, Wnt4, Wnt 5a, Wnt5b, Wnt7b, Wnt 9a, and Wnt 11 (Figure 34c), further substantiating the specificity of the angiocrine Tie-Wnt crosstalk axis. Consistent with the downregulation of Wnt9b and Wnt2, Wnt target genes, including Axin2 (Wang et al., 2015), Tbx3 (Wang et al., 2015), Sox9 (Blache et al., 2004) and Lgr5 (Huch et al., 2013), were down-regulated in Tie1^{iECKO} upon PHx (Figure 34d). As a consequence, liver regeneration was significantly impaired in Tie1^{iECKO} mice as evidenced by a reduced liver-to-body ratio (Figure 34e). Lastly, the specificity of these findings was substantiated by Tie1 blocking antibody experiments during PHx, which phenocopied the genetic Tie1 endothelial inactivation experiment (Figure 34f and g).

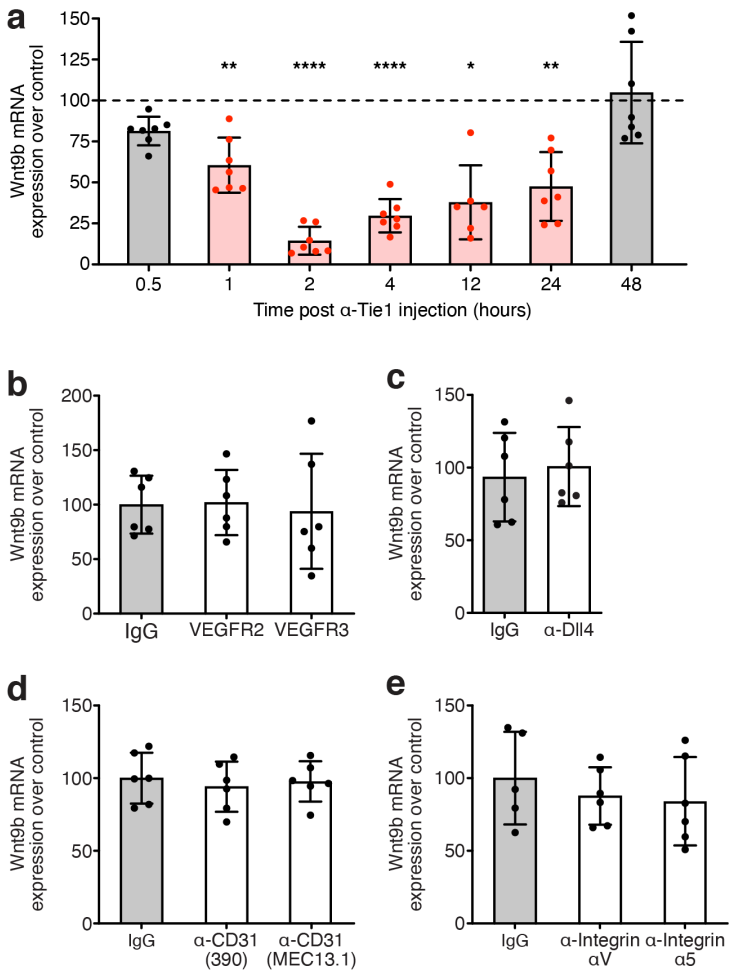

Figure 31. Tie1 specifically regulates the expression of Wnt9b. (a) Wnt9b mRNA (whole liver tissues) from anti-Tie1 treated C57/B6 mice, normalized to the relative IgG treated C57/B6 mice (dashed line), significantly regulated time points highlighted in red. (b-e) qRT-PCR analysis of Wnt9b mRNA measured in whole liver lysates 2 h after administration of the indicated blocking antibody against VEGFRs **(b)**, deltalike ligand 4 (Dll4) **(c)**, PECAM1/CD31 **(d)**, and alpha-chain integrins **(e)**. Data are expressed as percentage normalized to the corresponding controls. n = 6, each mouse is represented as a dot, bars indicate group mean ± SD. Unpaired Student's t-test was used to determine the difference between experimental groups. * p<0.05, ** p< 0.01, *** p < 0.001, **** p< 0.0001.

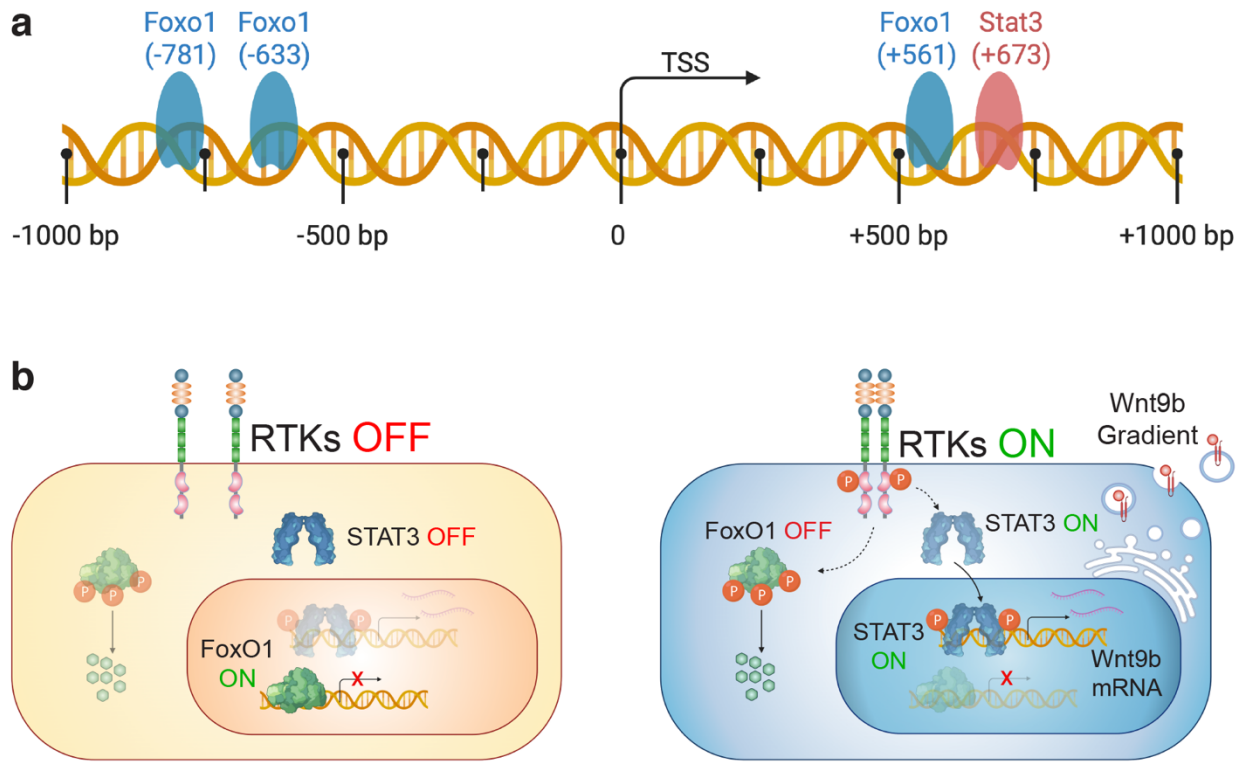

Figure 32. Putative regulation of Wnt9b by FoxO1 and STAT3 transcription factors. (a) Representation of Wnt9b promoter region. Putative binding sites for FoxO1 and STAT3 are indicated in blue and red respectively. **(b)** Signalling scheme of FoxO1 and STAT3 activation and nuclear translocation with inactive (left panel) or active (right panel) RTK signalling.

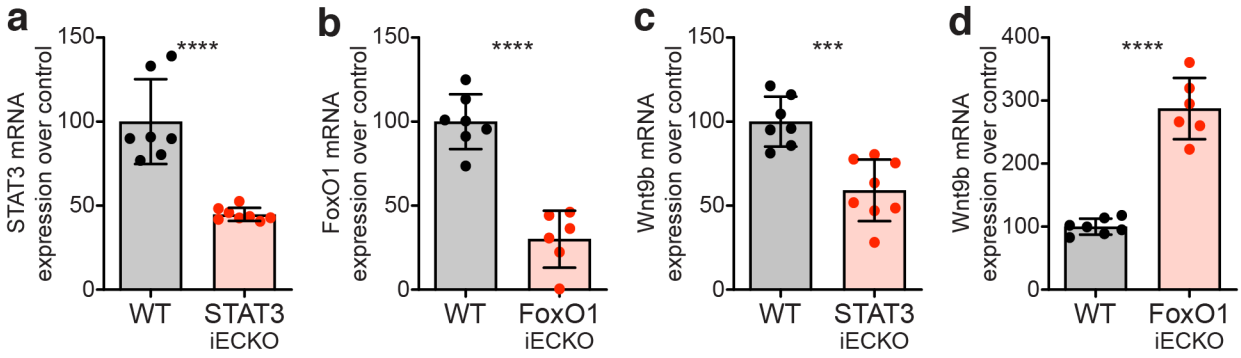

Figure 33. FoxO1 and STAT3 reciprocally regulate Wnt9b expression. (a and **b)** qRT-PCR analysis of Stat3 **(a)** and Foxo1 **(b)** mRNA expression from freshly isolated L-EC after tamoxifen treatment of $Stat3^{iECKO}$ and $Foxo1^{iECKO}$ mice (red bar) and relative control mice (grey bar). **(c** and **d)** mRNA expression of Wnt9b in $Stat3^{iECKO}$ **(c)** and $Foxo1^{iECKO}$ **(d)** mice (red bar) normalized to the relative control mice (Cre- littermates, grey bar) from isolated L-EC. n = 6, 7, 8; each mouse is represented as a dot. Data are expressed as percentage normalized to the corresponding controls. Unpaired Student's t-test was used to determine the difference between experimental groups. Result are expressed as mean ± SD. *** $p < 0.001$, **** $p< 0.0001$.

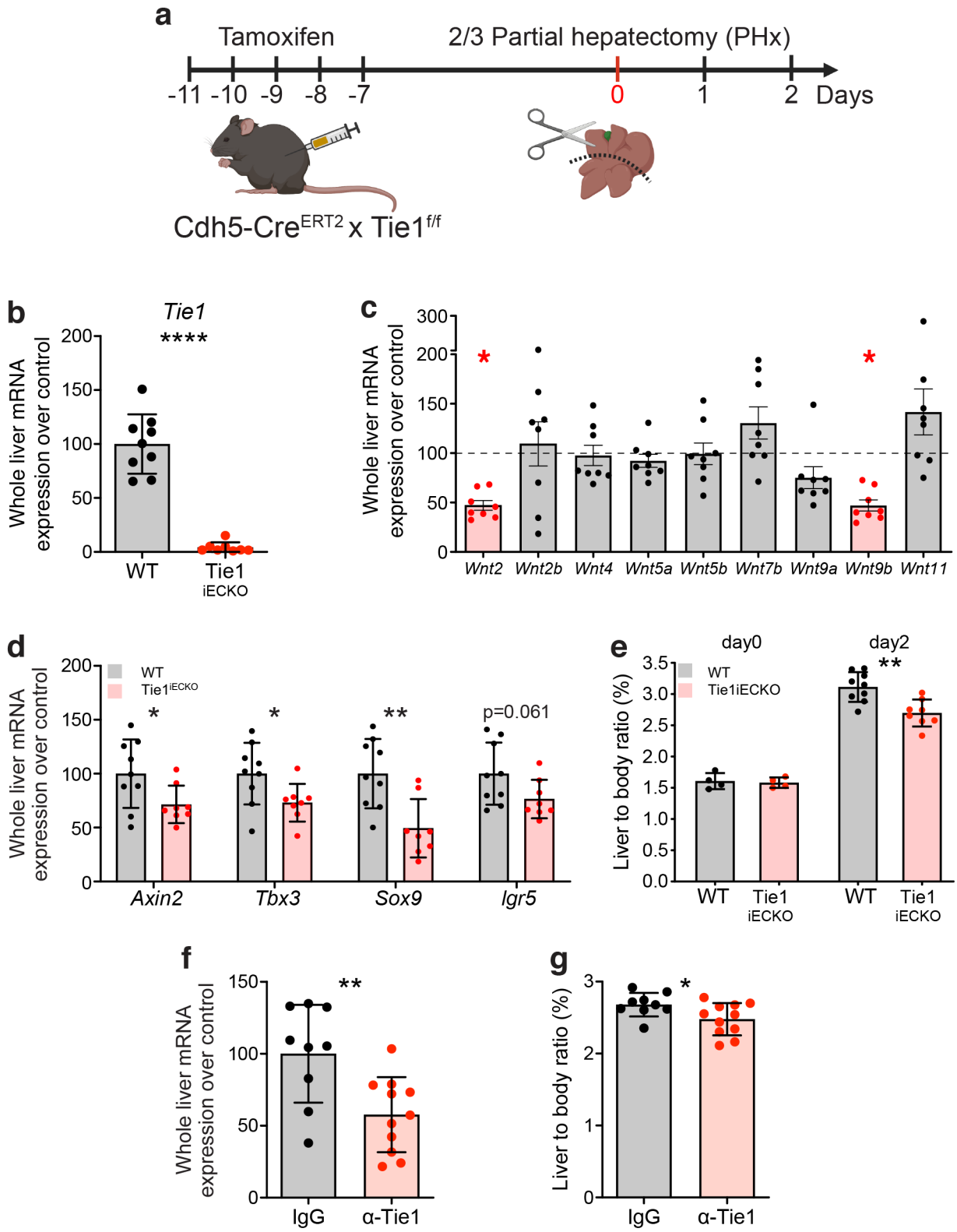
a
Tamoxifen
2/3 Partial hepatectomy (PHx)
-11 -10 -9 -8 -7
0
1
2 Days
Cdh5-CreERT2 x Tie1f/f
b
Tie1
****
Whole liver mRNA expression over control
WT
Tie1 iECKO
c
Whole liver mRNA expression over control
Wnt2 Wnt2b Wnt4 Wnt5a Wnt5b Wnt7b Wnt9a Wnt9b Wnt11
d
WT
Tie1iECKO
Whole liver mRNA expression over control
p=0.061
Axin2 Tbx3 Sox9 Igr5
e
day0
day2
WT
Tie1iECKO
Liver to body ratio (%)
f
Whole liver mRNA expression over control
IgG
α-Tie1
g
Liver to body ratio (%)
IgG
α-Tie1

Figure 34. Sustained liver regeneration through the Tie-Wnt signalling axis. (a) Experimental schedule for EC deletion of Tie1 followed by 2/3 partial hepatectomy (PHx). **(b)** qRT-PCR analysis of Tie1 mRNA measured in whole liver lysates after tamoxifen treatment of $Tie1^{iECKO}$ (red bar) and relative control mice (grey bar). **(c)** mRNA expression of Wnt ligands (whole liver) 2 days after 2/3 PHx in $Tie1^{iECKO}$ mice, normalized to the relative control mice (Cre- littermates, dashed line), significantly regulated genes highlighted in red. **(d)** mRNA expression of Wnt target genes from whole liver tissue 2 days after 2/3 PHx in $Tie1^{iECKO}$ (red) and corresponding controls (Cre- littermates, grey). **(e)** Liver-to-body ratio of $Tie1^{iECKO}$ (red) and relative controls (Cre- littermates, grey) at the indicated time points after 2/3 PHx. **(f** and **g)** Whole liver Wnt9b mRNA expression **(f)** and liver to body ratio **(g)** measured in C57/B6 mice 2 days after 2/3 PHx, treated with anti-Tie1 blocking antibody Tie1-39 (red bar) or IgG control (grey bar) at day 0. All gene expression was determined by qRT-PCR and normalized to Actb. n = 4, 8, 9; each mouse is represented as a dot.Data are expressed as percentage normalized to the corresponding controls. Unpaired Student's t-test was used to determine the difference between experimental groups. Result are expressed as mean ± SD. * $p<0.05$, ** $p< 0.01$, *** $p < 0.001$, **** $p< 0.0001$.

2.6 The role of Tie1 cleavage

Surface presented Tie1 can be processed by metalloprotease in response to stimulation, such as phorbol-12-myristate-13-acetate (PMA), VEGF, tumour necrosis factor-α (TNF-α), as well as changes in shear stress, resulting in the shedding of the extracellular domain (Chen-Konak et al., 2003; Marron et al., 2007; Yabkowitz et al., 1999; Yabkowitz et al., 1997). The shedding of the extracellular domain of Tie1 is involved in regulating the context-dependent outcome of Angpt/Tie signalling (Kim et al., 2016; Korhonen et al., 2016; Marron et al., 2007), which prompted us to further investigate the role of Tie1 cleavage in Wnt regulation and liver regeneration.

2.6.1 Site-directed mutagenesis of Tie1 cleavage site

The human Tie1 (hTie1) cleavage site has been mapped between amino acids E749 and S750, positioned in the juxta-membrane domain (Yabkowitz et al., 1999). As mouse Tie1 (mTie1) is highly homologous to hTie1 (Figure 35a and b), it was consequently hypothesized that mTie1 would similarly respond to stimulation and that the cleavage site is between E745 and S746. Therefore, I performed site-directed mutagenesis surrounding the cleavage site as indicated in Figure 35b. Different mTie1 mutants were overexpressed in HEK cells by lentiviral system and the cells were stimulated with PMA to induce Tie1 cleavage. First, I mutated the amino acids flanking the cleavage site and tested the mutation E745A/S746A. However, the mutation did not change the property of Tie1 in terms of response to PMA (data not shown). To confirm that the cleavage site in mouse is positioned the same as mapped in human Tie1, I tested deletion mutations, where amino acids 745-746, 744-747, 741-750 were deleted respectively. Indeed, these mutants of Tie1 were resistant to PMA stimulation. However, an additional fragment was observed on the Western blot analysis (data not shown), which led to the next strategy to perform mutagenesis on amino acid surrounding the cleavage site. As shown in Figure 35c, R744A, R744E, R747A, R744A/R747A

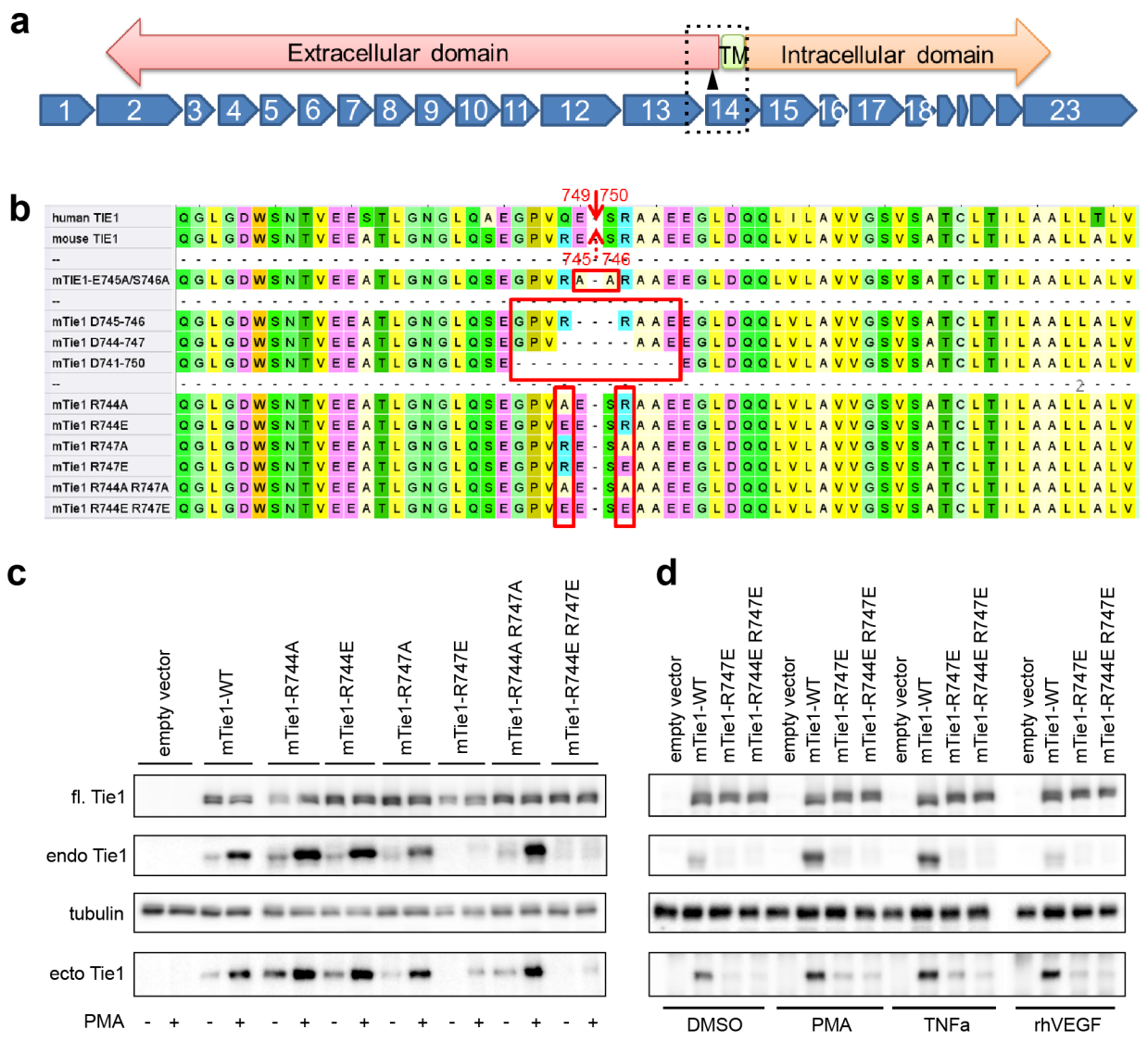

Figure 35. Site-directed mutagenesis of Tie1. (a) Genomic structure of Tie1. Human and mouse Tie1 are highly homologous and share the same genomic structure. Exons are depicted in blue with corresponding number and extracellular, intracellular domain as well as transmembrane (TM) domain are marked. Cleavage site is indicated with arrow head. A zoom-in sequence comparison is shown for the area marked with dashed lines. **(b)** Tie1 cleavage site mutagenesis strategies. Human and mouse Tie1 amino acid sequences are aligned and the cleavage site are indicated with arrows and numbers. Different mutagenesis strategies have been employed as highlighted. **(c** and **d)** Western blot analysis of Tie1 shedding. Full-length (fl.), endodomain (endo) fragment of Tie1 were detect in the cell lysates using Tie1 antibody raised against the intracellular part of Tie1. Ectodomain (ecto) Tie1 were detected via immunoprecipitation with Tie1 extracellular specific antibody from cell supernatant. HEK293A cells were treated with indicated stimuli for 30 min with the following concentration: PMA: 10ng/ml; TNFα: 100ng/ml; recombinant human VEGF (rhVEGF): 100ng/ml. Three independent experiments were performed and the representative images were shown.

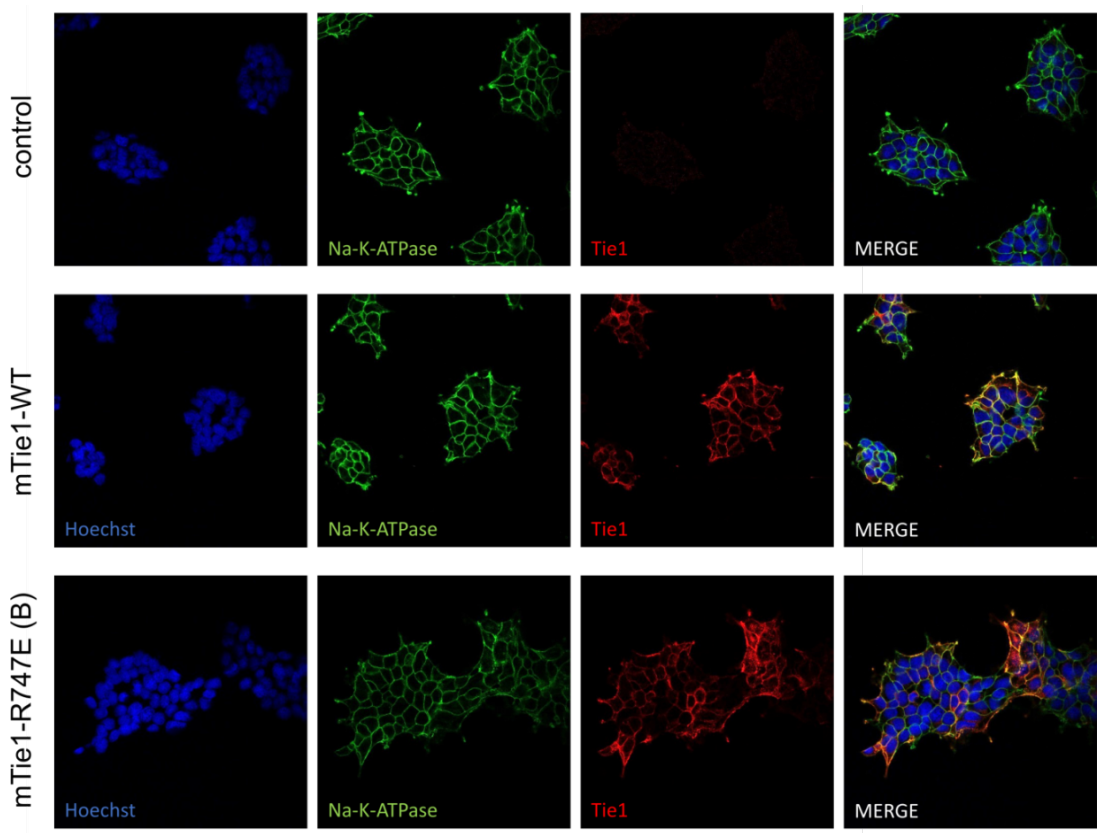

Figure 36. Tie1-R747E mutant was presented on the cell membrane. HEK293 cells overexpressing the indicated Tie1 form were seeded cover glasses and stained with the antibodies against Na-K-ATPase (green) and Tie1 (red). Hoechst (blue) and Na-K-ATPase mark the nucleus and the plasma membrane, respectively. Representative images from three independent experiments.

mutation did not affect Tie1 cleavage but R747E and R744E/R747E mutation almost completely abolished Tie1 cleavage. These two cleavage-resistant mutants were then further validated by TNFα and VEGF stimulation (Figure 35d). Considering that hTie1-748Q and mTie1-744R are not conserved, I therefore concluded that the mTie1-747R site is crucial for the cleavage recognition.

Even single amino acid mutation could lead to conformation change of the protein and thus change of its property. Tie1 is highly glycosylated after translation, before it can be represented on the cell membrane. Therefore, in Western blot analysis, the antibody against Tie1 normally detected a doublet band, with the upper band represent the mature glycosylated protein and the lower one the incomplete glycosylated form that is yet to be translocated to the membrane (Yabkowitz et al., 1997). The size and the doublet Western blot bands for Tie1-R747E mutant was same to the WT Tie1, suggested the occurrence of glycosylation of the mutant form. Next, I asked if the mutant form was properly translocated to the membrane. As shown by immunofluorescent staining, the majority of Tie1-R747E mutant was membrane located (Figure 36). Together, I identified the crucial amino acid for Tie1 cleavage recognition and established a mutant form that was cleavage resistant but maintained the post-translational modification.

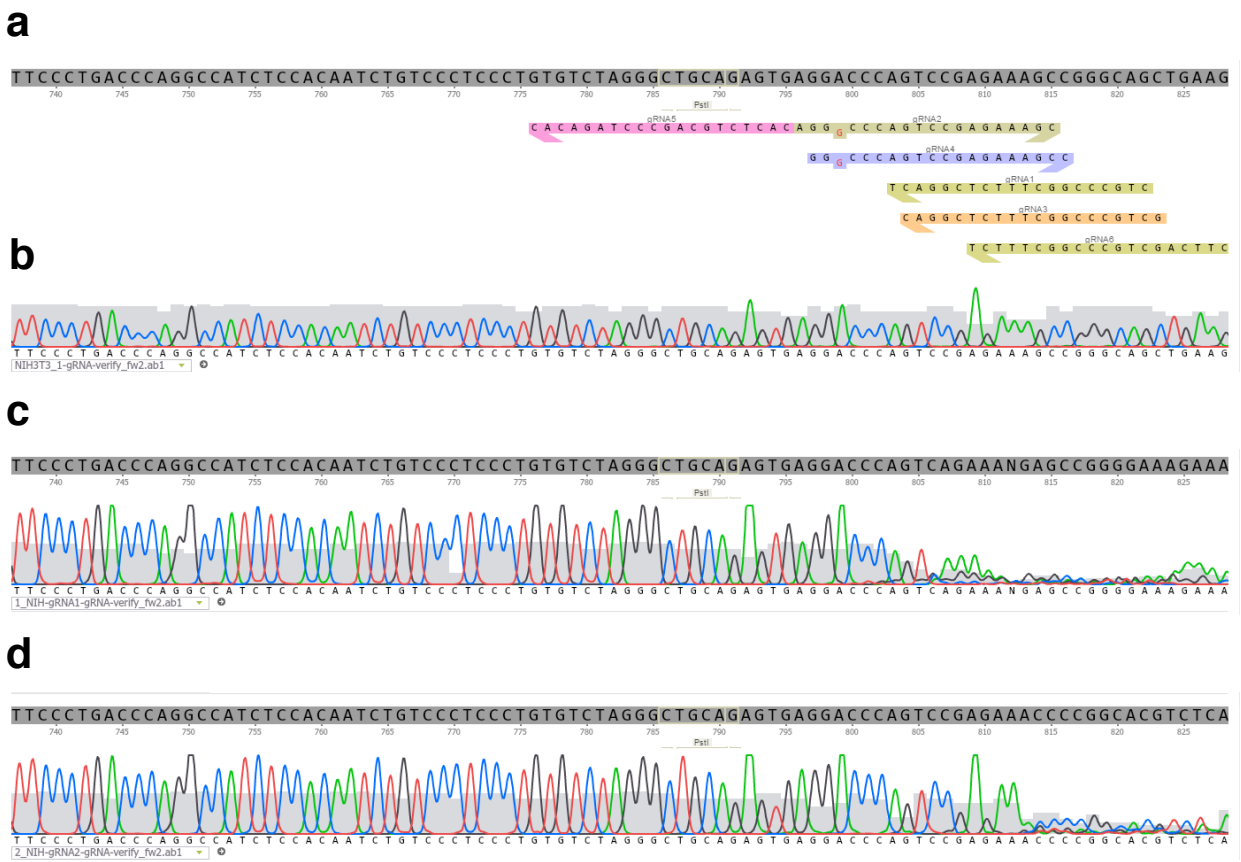
a
b
c
d
e
desired mutation: GA
Reference
no variant
SNV:6
3:1D
4:1I
2:2D
−6:10D
−2:9D
1:4D
3:1I
Other
12414
9667
118
633
338
132
79
76
76
54
150
Percentage
0
25
50
75
100
Jing12

Figure 37. Genome editing by CRISPR/Cas9. (**a**) Mouse genomic sequences surrounding the Tie1 cleavage site and the sequence of the sgRNAs. (**b-d**) Sanger sequencing histograms of NIH3T3 cells flanking the mouse Tie1 cleavage site for non-transfected (b), sgRNA1 (c) and sgRNA2 (d) transfected cells. sgRNA3-6 similar to sgRNA1-2, graphs not shown. n = 1. (**e**) MiSeq result from sgRNA2 and repairing template co-transfected NIH3T3 cells. Representative result from four sequenced samples.

2.6.2 The Tie1 uncleavable form does not change homeostatic Wnt signalling

To investigate the role of Tie1 shedding *in vivo*, a mouse model carrying the Tie1 uncleavable point mutation R747E ($Tie1^{R747E}$) was generated employing CRISPR/Cas9 technology.

I designed with CRISPR DESIGN tool (Zhang lab) 6 sgRNAs which target the genomic region of Tie1 cleavage site (Figure 37a). In order to check the efficacy of the sgRNAs, NIH3T3 cells were transfected with sgRNA and Cas9 expressing vector, and eventually genomic DNA was extracted for analysis. The target region was amplified by PCR and examined by Sanger sequencing and I could show that all the 6 sgRNA efficiently targeted the Tie1 cleavage site (Figure 37b-d). Two sgRNA with higher score by CRISPR DESIGN were chosen and together with a repairing DNA template, were transfected in NIH3T3 cells and examined by Illumina MiSeq system in collaboration with Dr. Zhan from Division of Signalling and Functional Genomics at DKFZ. Despite with low efficiency, the desired CG → GA mutation was detected (Figure 37e). The major reason for the low repairing efficiency could be that Non-homologous end joining (NHEJ) DNA repair is the major repairing mechanism upon DNA damage. A second reason could be that in culture, only a subset of the cells is proliferating. As the zygote is 100% proliferating and homologous repairing is more prevalent during cell division, better efficiency *in vivo* was therefore expected.

As no significant difference between sgRNA1 and sgRNA2 regarding targeting and repairing efficiency was observed, I performed *in vitro* transcription of the sgRNA2 and further generated the $Tie1^{R747E}$ mouse line in collaborated with the Transgenic Service at DKFZ, where the embryonic microinjection and embryo transplantation were performed. First, Cas9 protein was injected in the zygote together with the sgRNA and the repairing template. However, the injection was with low successful rate, possibly because of the glycerol contained in the buffer for protein preservation, which changed the viscosity of the solution. Therefore, Cas9 mRNA was used instead. In total, 227 morula was successfully transplanted to surrogate mothers and 16 pups were born, two carrying the desired mutation. As observed in *in vitro*, most of the embryonic mutation would have been random mutations due to NHEJ often leading to premature stop codons, which would result in nonsense mRNA decay for Tie1. As Tie1 embryonic knockout is lethal (Puri et al., 1995; Sato et al., 1995), therefore, most of the embryos did not survive until birth.

The two founder mice ware used to establish the mouse line and mice were born at expected Mendelian ratio from heterozygous mating (Figure 38a). and $Tie1^{R747E}$ homozygous mice were phenotypically normal and fertile and overtime monitor of body weight revealed that the $Tie1^{R747E}$ mice had similar growth rate (Figure 38b-c). This mutation was further validated *in vivo* by Western blot from whole tissue lysates from

lung (Figure 39a). Next, gene expression analysis was performed to examine the potential effect of Tie1 shedding on Wnt expression. However, as shown in Figure 39b, R747E mutation did not have any effect on L-EC derived Wnt expression (Wnt2 and Wnt9b), nor the Wnt target genes (Axin2 and Tbx3). This, however, is in line with the notion that Tie1 shedding is involved in inflammatory condition. Therefore, it is reasonable that in static condition the gene expression is not impacted or compensated. We are currently using different models for acute liver damage such as CCl_4 or partial hepatectomy to evaluate the role of Tie1 cleavage in supporting the activation of Wnt signalling during liver injury and regeneration.

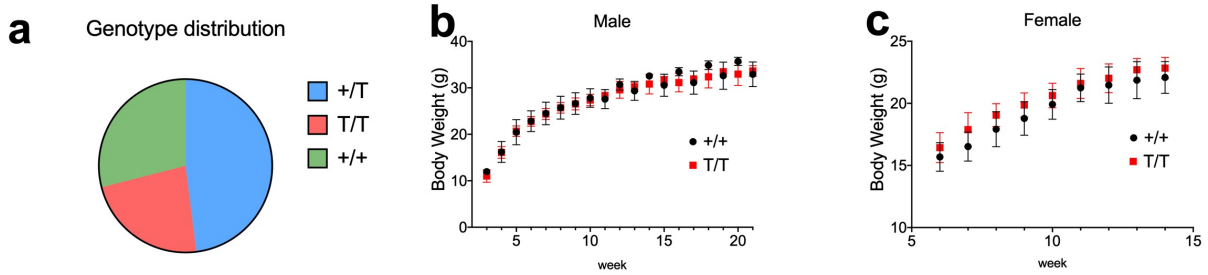

Figure 38. Tie1^{R747E} mice were phenotypically normal. (**a**) Genotype distribution from heterozygous breedings of Tie1^{R747E} mice. (**b-c**) Body weight (g) of male (b) and female (c) mice over time. Male +/+, n = 10 mice; Male T/T, n = 8 mice; Female +/+ and T/T, n = 8 mice. +/+: WT control; T/T: homozygous mutation; +/T: heterozygous mutation.

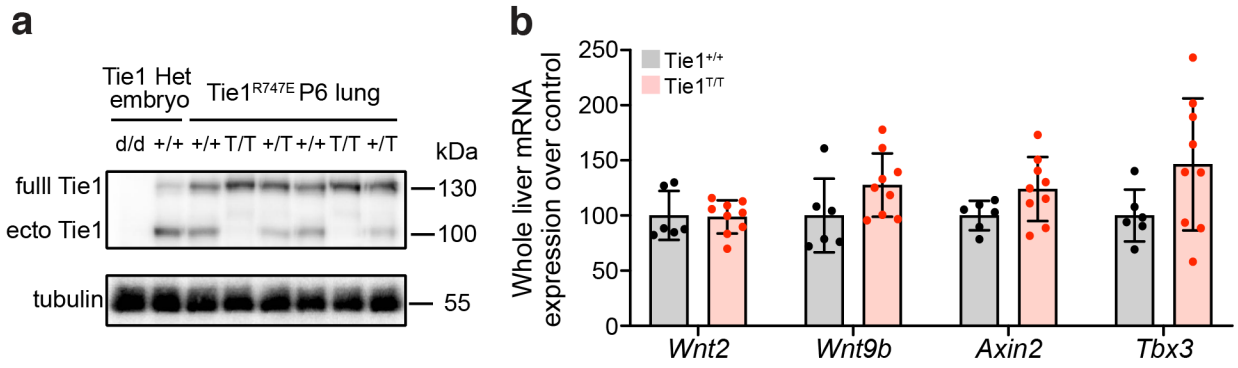

Figure 39. Tie1 uncleavable mutation does not affect homeostatic Wnt signalling. (a) Western blot analysis of Tie1 uncleavable mutant in *vivo*. Whole lung tissue lysates from post-natal day 6 Tie1^{R747E} mice were probed for Tie1 antibody raised against its extracellular domain. Constitutive Tie1 knockout (KO) embryo lung lysates were included as negative control. n = 2 for each genotype. **(b)** mRNA expression of Wnt ligands and Wnt target genes from whole liver tissue from adult Tie1^{R747E} mice. n = 6, 9; each mouse is represented as a dot. d/d: homozygous KO; +/+: WT control; T/T: homozygous mutation; +/T: heterozygous mutation.

3. Discussion

The liver endothelium displays spatial and molecular heterogeneity along the axis of the liver lobule, facilitating its specialized angiocrine functions through which it controls adjacent hepatocytes. The endothelium thereby exerts gatekeeper roles in maintaining liver metabolic zonation (Rocha et al., 2015; Wang et al., 2015) and hepatic responses to pathologic challenge including liver regeneration, fibrosis and cancer (Cao et al., 2017; Ding et al., 2010; Hu et al., 2014; Morse et al., 2019). The present study established comprehensive genome-wide transcriptomic, proteomic and phosphoproteomic maps of liver endothelial spatial organization, yielding unparalleled insight into the interplay of transcriptional, translational and posttranslational mechanisms controlling the activity of individual L-EC molecules and pathways.

3.1 A complete coverage of L-EC transcriptome with spatial resolution

scRNAseq has emerged as a powerful tool to identify rare cell populations and delineate the subtle differences of morphological or functional similar cells. However, dissociation of tissue to obtain single cell suspensions is a prerequisite for most studies, leading to the loss of spatial information. When the tissue organization is well-known, for example, the gradient expression of landmark genes in hepatocytes along the lobular axis, the spatial information can be retrieved based on the known gene expression pattern/combination (Halpern et al., 2017). When there is no detailed information or specific markers, different strategies were recently proposed. For instance, the Itzkovitz group successfully applied a paired-cell sequencing strategy to obtain the spatial transcriptome of the L-EC. Specifically, they took advantage of not completely dissociated hepatocyte-EC pairs to use a panel of hepatocyte landmark genes to infer the spatial information of the paired L-EC (Halpern et al., 2018). More recently, tissue *in situ* transcriptomic solutions promise to provide the whole transcriptome on tissue section pre-coated with arrays of barcodes spots, in order to correlate both gene expression and morphological data (Vickovic et al., 2019). These innovations hold promise to revolutionize our understanding of tissue structure and functional divisions of an increasing number of different cell subtypes.

However, sequencing sensitivity is still a limiting factor for the single cell field. For example, the paired-cell sequencing strategy has obtained around 1,300 genes for L-EC (Halpern et al., 2018). Similarly, the recent EC atlas detected on average 1,300 genes per cell (Kalucka et al., 2020). The latest Smart-seq3 technology had made fundamental improvement to resolve allele and isoform information and could detect around 4,000 genes per cell (Hagemann-Jensen et al., 2020). In contrast, a regular RNAseq could yield more than 10,000 expressed genes, much beyond the limitation of scRNAseq. Indeed, in the current spatial bulk cell RNAseq, more than 13,000 L-EC genes have been quantified. The confirmation of expression pattern for low abundant genes by qRT-PCR, which were close to the detection limit of qRT-PCR, indicates a complete coverage of the L-EC transcriptome in this study.

The spatial bulk cell RNAseq approach has yielded more than an order of magnitude higher sequencing depth to the available EC databases (Halpern et al., 2018; Kalucka et al., 2020), thus allowing us to

unambiguously define expression pattern enriched on large vessels or in sinusoidal EC. Of note, sinusoidal EC are positioned between a vascular lumen (sinusoid) and a lymphatic like space (space of Disse), which is in line with the atypical enrichment of lymphatic EC identity markers Vegfr3 and Lyve1 in the sinusoidal area compared to the neighbouring large vessels. In turn, proteins characterizing typical vascular pathways (i.e., shear stress, cell adhesion molecule) were found polarized on portal and central EC but not in sinusoidal EC. Together, these findings delineate sinusoidal EC as a highly specialized cell population with a unique hybrid phenotype between lymphatic and vascular EC, in line with previous studies (Tanaka and Iwakiri, 2016). Together with the panels of TF, kinome and phosphatome, this study has offered a great resource for the understanding of tissue heterogeneity.

3.2 The first comprehensive vascular (phospho-)proteome with spatial resolution

Proteins are the major executors of the biological functions and their abundance, location and activities are tightly controlled at multiple levels. In this study, more than 5,000 proteins have been quantified, representing the first *in vivo* endothelial proteome. The expression of proteins is by large reflected on the transcript level, as demonstrated in this study as well as other studies that there was strong positive correlation of the mRNA and protein abundance (Eraslan et al., 2019; Mergner et al., 2020). On the other hand, a large variance of PTR for different genes was observed, indicative of a diverse regulation of protein biosynthesis and decay (Hausser et al., 2019; Mergner et al., 2020). PTR in general follows a Gaussian distribution, with ~80% in a relative restricted range. However, several hundreds of genes strongly deviated from this range, defined as high or low PTR genes. From an evolutionary point of view, a high RNA pool for translation (i.e., lower PTR) reflects the fast adaptation to the cellular need to achieve an appropriate protein copy number. In turn, a high RNA reserve is energy demanding, evidenced by fewer low PTR proteins. Overall, the cell acquires an equilibrium between precise regulation and cost efficiency (Hausser et al., 2019). In line with this, we identified ribosome component proteins enriched among low PTR proteins, ensuring a large RNA reserve ready to adapt to intrinsic and extrinsic challenges, whereas metabolism-related processes are likely to have better protein stability to most cost efficiently maintain the basic cellular activities (Figure 17). Together, L-EC exhibit a highly diverse and tightly coordinated regulation on post-transcriptional and post-translational levels to balance their energy consumption and adaptability. On the other hand, the segregation of high and low PTR proteins into functional related protein networks also demonstrate the strength of this system for comparative studies (Figure 18), which was exemplified also by the study from (Mergner et al., 2020). One aspect that was not addressed in this study is the sequence based prediction of PTR. It was previously reported that certain mRNA or protein sequence motifs were associated with PTR regulation through matching 11,575 protein-mRNA pairs across 29 human tissues (Eraslan et al., 2019). A single cell type as in this study might not be sufficient to draw conclusions. However, it could serve as a building block for future researches such as to investigate whether these regulatory motifs were conserved among different species.

Furthermore, integration of the spatial information led the analysis to a “pseudo-single-cell” resolution. Comparison of the expression pattern along the sinusoids of protein and mRNA revealed an over 90% congruence, indicating that the protein abundance is largely dependent on the transcription level. Yet, the other 10%, which nevertheless represents hundreds of proteins, are those that dynamically regulated after transcription. This observation is supported by the conclusion from Liu *et al* that protein levels is primarily explained by RNA levels at steady state but transcript levels are not sufficient to predict protein levels in many scenarios (Liu et al., 2016). Therefore, this study laid a solid foundation for understanding the biology of the vascular bed on protein level and would ignite follow up researches focusing on various pathological conditions.

In this study CoM was used to correlate the different datasets (Ben-Moshe et al., 2019), which, as seen throughout the result, served as a powerful parameter to quantitively assess the pattern without interference of different units for absolute amount. Following the blood flow direction or oxygen level, liver sinusoids can be considered as a linear model that probably best exemplify the strength of CoM. Nevertheless, I believe this concept can be further applied in any hierarchal system that is unidirectional, for example the gut villi, kidney nephron, ect. It is also worth noting that for more heterogenous patterns, like the large vessel and sinusoidal pattern defined in this study (Figure 9 and 16), CoM is not well applicable. Therefore, development and implementation of other mathematical models are needed in the future in order to be applicable for nonlinear distributions.

Phosphorylation represent a major mechanism to regulate protein function. More than 100,000 distinct phosphorylation events have been identified in human cells, which likely affect the function of every protein (Needham et al., 2019). Most mass spectrometry based phosphoproteome analyses were performed on tissues or cell lines because of the prerequisite on input quantity for phosphopeptide enrichment (Huttlin et al., 2010; Locard-Paulet et al., 2016; Meijer et al., 2013; Villen et al., 2007). Endothelial cells are flat in shape and contain little amount of mRNA and proteins (Ben-Moshe and Itzkovitz, 2019; Jakab and Augustin, 2020). Therefore, it is particular challenging to analyse the endothelial proteome. In this study, the L-EC isolation protocol was optimized to minimize the effect of sample processing on the phosphorylation status and the spatial sort strategy enabled the pool of cells from the same position.

Finally, I had successfully obtained the first *in vivo* vascular specific phosphoproteome map integrated with spatial information. The phosphoproteomic map of L-EC spatial zonation yielded unparalleled insight into liver vascular function. We discovered zonated genes with high congruence of RNA, protein and phosphoprotein levels, but we also discovered many genes that were exclusively regulated post-translation on the activation level. Biologically, the probably most remarkable discovery was the strong enrichment of tyrosine phosphorylation in the central vein area of the endothelium. Except five p-Y, all the 181 zonated p-Y exhibit a central pattern. When compared the CoM of the p-Y to the corresponding proteins, 133 out of 171 p-Y (with corresponding protein detected in the proteome) displayed a shifted expression pattern, indicating that tyrosine phosphorylation was zonated largely irrespective of the

amount of protein. In addition, considering that the zonation patterns of p-S and p-T were evenly distributed, the localized tyrosine phosphorylation is unlike due to experimental or analytical artifact. This result, therefore, also demonstrated that the experimental set up allowed to satisfy the sample requirement for phosphoproteomic analysis in terms of high input quantity and at same time preservation of the chemically unstably phosphorylation gradient along the liver capillary.

Together with the spatial transcriptome and proteome, this study provided a spatial resolved atlas of the protein distribution along the liver sinusoid together with their activation status, and definitely the first functional map of the L-EC proteome. Moreover, by applying different mathematic parameters, I presented different data integration and visualization modalities that could serve as an analysis template to further characterize the current datasets on L-EC as well as on other morphologically polarized organs.

3.3 Tie1 shapes the central vein EC signature

When zooming in on individual vascular RTKs, the angiopoietin receptors Tie1 and Tie2/TEK were identified among the top zonated p-proteins, despite their homogenous mRNA and protein levels along the axis of the liver lobule. In contrast, the phosphorylation of VEGFR2, VEGFR3, cKit and Ephb4, despite an overall central zonation pattern, was much more resembling their protein/RNA expression (Figure 27). This difference of phosphorylation stoichiometry suggested a highly localized activation of Tie pathway and possibly a regulatory role in liver zonation.

Retrieving this information from the phosphoproteomic map, I prototypically validated this hypothesis. Indeed, I could show that *in vivo* application of a Tie1 blocking antibody followed by spatial transcriptome analysis of peri-portal and peri-central L-EC identified a more prominent gene regulation on central vein L-EC (157 regulated genes) compared to portal L-EC (88 regulated genes) (Figure 29), substantiating the concept of the pericentral polarization of Tie1 signalling. Notably, Wnt9b and Lhx6, scoring among the top centrally zonated genes, were both identified as the most prominently regulated transcripts indicating that Tie1 signalling acts as a central vein specifier.

In addition, in vivo blocking experiments applied to several major EC signalling pathways, including VEGF, Notch, CD31 and Integrins did not lead to alteration of Wnt9b expression, revealing a high specificity of Tie signalling pathway regulation on L-EC Wnt9b ligand. It can be speculated that under extended treatment regime or under conditions where EC is subjected to perturbation, Wnt expression can be regulated differently, which can be further addressed in the future studies.

3.4 Identification of Tie1-STAT3/FoxO1-Wnt9b axis

Tie1 had remained an orphan receptor until recently and is generally considered to be a co-receptor for Tie2 (Saharinen et al., 2017a; Xu et al., 2019). Therefore, direct effectors of Tie1 that mediate Wnt ligand transcriptional changes is likely downstream of Tie2 signalling. STAT proteins are important mediators linking extracellular signalling cues to both transcriptional and non-transcriptional events which are involved in a wide range of cellular functions (Huynh et al., 2019). Tie2, more potently Tie2-R849W mutant,

could induce tyrosine phosphorylation and DNA binding activity of STAT3 and STAT5, whereas Tie1 alone only weakly activated STAT3 and STAT5 (Huynh et al., 2019). On the other hand, it is well established that FoxO1 activity is inhibited by Angpt-1 mediated Tie2/Akt signalling (Daly et al., 2004; Kim et al., 2016). Notably, the FoxO1 regulation is opposed to most known TFs as phosphorylation retains FoxO1 in the cytoplasm which restricts its transcriptional activity (Brunet et al., 1999). *In silico* analysis reveals that Wnt9b promoter region contains putative binding motifs for both STAT3 and FoxO1 (Figure 32), and subsequent mouse genetic knockout studies further substantiate the direct regulation of STAT3 and FoxO1 on Wnt9b expression, especially considering their opposing effect (Figure 33). In addition, chromatin immunoprecipitation (ChIP) with STAT3 or FoxO1 specific antibody followed by PCR analysis of the Wnt9b promoter region demonstrated a direct binding of these TFs to Wnt9b promoter (data not shown, personal communication with Dr. Inverso).

Whereas current data in turn substantiate that the Tie1-STAT3/FoxO1-Wnt9b axis is Tie2-dependent, a possible Tie1 direct or indirect regulation of STAT3 and FoxO1 that is independent of Tie2 cannot be excluded. In line with this, *in vivo* treatment of a commercial Tie2 antibody failed to induce Wnt9b transcriptional changes within 2h (data not shown, personal communication with Dr. Inverso).

Wnt signalling is involved in a plethora of cellular processes during development and disease and has received intensive research since its discovery almost 40 years ago (Klaus and Birchmeier, 2008). It has been estimated that about one-third of hepatocyte zonated genes are Wnt targets, highlighting the crucial role of this signalling pathway (Ben-Moshe and Itzkovitz, 2019). A PubMed search of “Wnt” resulted in over 40,000 hits with an increasing trend (retrieved on November 2020). However, the vast majority of these studies have been focused on Wnt downstream pathways and on the Wnt target genes. Conversely, our knowledge about the regulation of the Wnt ligand production is mostly restricted to the Wnt ligand secretion and very few is known about their transcriptional regulation. Here, I identified Tie1 signalling as a major and spatial Wnt ligand regulator in the liver and we are currently investigating if a similar mechanism is involved in other tissue context.

However, considering the wide range of cellular activities regulated by Wnt signalling, it remains very plausible that other TFs can regulate Wnt expression. Indeed, in silico analysis of the Wnt9b promoter revealed many other TF candidates including previously mentioned STAT5a:5b, as well as Hes1, Hes2, Hey1, Hey2 and KLF4. As formerly discussed, STAT5 could also be activated by Tie2 (Huynh et al., 2019), but can mediate distinct, even opposing effect to STAT3 (Walker et al., 2009). The crosstalk between Notch and Wnt signalling has been well reported on multiple levels, including co-operative regulation of transcriptional targets, transcription-dependent interaction and direct molecular crosstalk between signal transduction machinery (Collu et al., 2014). KLF4 belongs to the Krüppel-like factor (KLF) family of transcription factors that plays crucial role in regulating vascular functions and has been reported to negatively regulate Wnt signalling by directly binding with β-catenin (Evans et al., 2010; Sweet et al., 2018; Zhang et al., 2012). Therefore, a further exploration on these candidates would be of future interest. It is

worth notifying that in the RNAseq analysis of this study, Hes2 and Hey2 were not detected, which excludes their role in Wnt regulation in L-EC at homeostatic status.

Of note, here I mostly focused on Wnt9b as readout of L-EC zonation, and the eventual functional difference between the two major Wnt ligands expressed by the L-EC (Wnt2 and Wnt9b) need to be further clarified. Although the 19 Wnt ligands have been classified into canonical and noncanonical Wnts, and individual Wnt genetic knockout models had yielded great insights, our understanding about the functional specificity and the regulatory mechanism remain limited (Clevers and Nusse, 2012; van Amerongen and Berns, 2006). Based on our transcriptomic data, the zonation pattern of these two ligands along the sinusoid was almost identical, with expression on portal zone approximately 8% of the expression level on central zone. However, the absolute abundance of Wnt2 was 7 fold more than Wnt9b, suggesting possible different functions.

3.5 Mechanistic insight of Tie1 function

Considering the role of Wnt signalling in maintaining tissue self-renewal and the regeneration capacity, I speculated a possible role of this Tie1-Wnt axis in supporting the liver regenerative potential. Specifically, Wnt signalling is well-established as a niche factor maintaining stem cell self-renewal in several organs, including the digestive tract, the hematopoietic and the nervous system (Barker et al., 2007; Nusse et al., 2008; van de Wetering et al., 2002; Willert et al., 2003). In the liver, the existence and localization of “stem cells” are controversial. Upon hepatectomy, the mature hepatocyte can all re-enter cell cycle to promptly restore the liver loss and the impaired metabolic capacity. However, during homeostatic renewal, or in response to certain injury, different markers for highly regenerative subpopulation have been reported. For example, Artandi group has shown that a Tert-high expressing subpopulation distributed in the liver could repopulate the liver during homeostasis and injury (Lin et al., 2018), while peri-portal Mfsd2a+ cells were described by Zhou group with similar characteristics (Pu et al., 2016). However, most of the molecules reported as markers of “highly proliferative hepatocytes” are typical Wnt responsive genes, including Axin2, Tbx3, Sox9 and Lgr5 (Ang et al., 2019; Blache et al., 2004; Huch et al., 2013; Wang et al., 2015). Moreover, EC derived Wnt ligands, Wnt2 and Wnt9b, in comparison to other cell type derived Wnt ligands, was significantly and specifically induced after hepatectomy and their genetic deletion led to a delay of cell cycle re-entry and cell proliferation to rescue the live mass (Preziosi et al., 2018).

Finally, our group have reported Angpt2 functions as a spatiotemporal rheostat via TGF-β and/or VEGFR2 to control hepatocyte and L-EC proliferation at different phases of regeneration (Hu et al., 2014). As a context-dependent antagonist, Angpt2 could mediate functionally opposing effect on its receptor Tie2. This functional switch was thought to be facilitated by Tie1 (Kim et al., 2016; Korhonen et al., 2016). In line with these considerations, the data presented here showed that Tie1 deficient led to a downregulation of the L-EC specific Wnt ligands in mice after partial hepatectomy, which was used as a model of liver regeneration. Consistently, I found that Wnt target genes, which were reported as markers of proliferative hepatocyte are downregulated with a significant delayed rescue of the normal liver mass.

Moreover, the specificity of this mechanism is confirmed by a similar phenotype observed in WT mice treated with a Tie1 blocking antibody before hepatectomy.

This data showed a strong functional relevance of the Tie-Wnt axis in shaping the L-EC zonation and in supporting the liver regenerative niche. Currently we are investigating other liver injury models including CCl_4 administration in Tie1 inducible endothelial KO mice ($Tie1^{iECKO}$). Metabolized by the cytochrome P450 family to the trichloromethyl radical (CCl_3^*), CCl_4 is a classical carcinogen that impairs lipid metabolism and triggers genomic mutations especially to pericentral hepatocytes (Weber et al., 2003). Initial results suggested that following acute damage induced by CCl_4, the expression of Wnt ligands and targeting genes was reduced in $Tie1^{iECKO}$ mice compared to control group (data not shown), which was in line with data acquired from hepatectomy model.

Notably, in a recent study using CCl_4 induced liver fibrosis mouse model, knock-down of Tie1 worsened the liver fibrosis, inhibited portal angiogenesis, but increased liver sinusoid capillarization (Xu et al., 2019). Interestingly, the same study identified the first ligand for Tie1, Lect2, almost 30 years after its discovery (Xu et al., 2019). Moreover, it is known that Lect2 is a direct target of β-catenin and its expression is restricted to the pericentral hepatocytes (Ovejero et al., 2004), which is in line with my observation that the Tie1 phosphorylation was also strongly zonated on the central side (Figure 27).

These data together suggest a self-sustainable signalling loop between pericentral hepatocyte and the EC: the pericentral hepatocyte β-catenin signalling support the Lect2 expression that in turn maintains Tie1 activation in neighbouring EC, while Tie1 activation induce the Wnt ligand production from EC, which in turn sustains the β-catenin in the surrounding hepatocyte. This observation again confirms the feasibility of the multiomic approach that I used here as I could identify a zonated Tie1 phosphorylation that occurs independently of the protein amount and is localized in the same region of the corresponding ligand Lect2. Still some discrepancies need to be addressed. In particular, in fibrotic condition as observed by Xu et al. (2019), Lect2 disrupts Tie1/Tie2 interaction and enhances Tie2 dimerization, resulting in higher Tie2 phosphorylation and lower Tie1 phosphorylation. Considering the context dependent modulatory role of Tie1 on Tie2 (Savant et al., 2015), the different behaviour of Tie1 in fibrotic and in homeostatic condition could be due to different liver microenvironment.

3.6 The ectodomain shedding of Tie1

Here, I could show that Tie1 signalling acted as a major determinant of the spatial heterogeneity of the L-EC, maintained the localized production of angiocrine Wnt ligands and finally was required for an efficient liver regeneration. On the other hand, the Tie1 signalling cascade is poorly characterized. Regarding the context dependent regulation of Angpt-Tie signalling, the ectodomain shedding of Tie1 represents a putative mechanism. Specifically, under homeostatic conditions, Tie1 sustains the agonistic function of Angpt1 and Angpt2 ligand effect. Whereas during inflammation, ectodomain of Tie1 is released into the circulation and elevated Angpt2 exerts an antagonistic function on Tie2 (Kim et al., 2016; Korhonen et al., 2016). However, direct evidence for a causative link of Tie1 shedding and Angpt2 functional switch is still

lacking. In addition to inflammatory stimuli, Tie1 cleavage is also induced by VEGF, a potent angiogenic factor, and indeed, the cleaved fragment is observed during mouse embryogenesis (Marron et al., 2007; Qu et al., 2010). Considering that liver regeneration requires angiogenesis and the spatiotemporal regulation by Angpt2, Tie1 shedding is likely to be involved in fine tuning of liver function.

An intrinsic difficulty to study context-dependent pathways is that an *in vitro* system can rarely reproduce the diverse microenvironment of the vascular system. To overcome this limitation, I established a mutant mouse bearing an uncleavable but functional mutant form of Tie1 ($Tie1^{R747E}$). Surprisingly, the $Tie1^{R747E}$ mice was viable and had no phenotype under standard housing condition. Therefore, the cleavage during angiogenesis could be a secondary effect or a normal turnover process of the receptor. In addition, expression of Wnt ligands and target genes was also not affected by the mutation, which could result from compensatory mechanisms. On the other hand, this observation is in line with the notion that Tie1 cleavage mostly occurs during inflammatory processes. To understand if Tie1 shedding acts as a regulatory element of Tie2 signalling or if the cleaved intracellular fragment has an independent function, we are currently using different local and systemic inflammation model as well as liver regeneration and fibrosis.

3.7 Closing remarks

Liver is one of the most well studied organ and there are many resources available regarding different cell types (Ben-Moshe et al., 2019; Dobie et al., 2019; Xiong et al., 2019). In this regards, computational tools, for example NicheNet, were developed to predict ligand-target interaction based on expression data by integrating prior knowledge of signalling networks (Browaeys et al., 2020). Yet, several predictions based on transcriptomic data have failed to yield satisfying results, highlighting the need for curation of current computational methodologies and development of novel algorithms. Therefore, data mining and collaborative integration with public resource is currently on going and we are establishing public online tools to allow an intuitive and comparative analysis of our L-EC datasets integrated with similar data on hepatocytes, Kupffer cells and stellate cells in order to provide a whole liver interactome resource.

Altogether, the present study can serve as a prototypic template on how to overcome analytical limitations of scRNAseq approaches: By datamining scRNAseq data for FACS suitable surface molecules with biologically relevant spatial expression pattern, spatial sort protocols of pre-purified cell populations can in principle be deduced from any tSNE or UMAP along any spatial anatomical or biochemical axis of interest. scRNAseq and spatial sort bulk analyses thereby complement each other to apply the power of single cell and bulk spatial resolution to thereby enable proteomic and, as shown as proof-of-concept in this study, even phosphoproteomic analyses. The data generated by this study has offer great insight into understanding the functional heterogeneity of the liver endothelium. I believe that only the tip of the iceberg is discovered. Further datamining of these datasets, together with other data sources including other spatially resolved liver cell populations, or other vascular beds, would shed more light on our knowledge on cell-cell interactions, signal transductions and organotypic functions.

4. MATERIALS AND METHODS

4.1 Material

4.1.1 Reagent suppliers

Table 1. Reagent suppliers.

Company	Webpage
Abcam	www.abcam.com
Addgene	www.addgene.org
Agilent	www.agilent.com
AppliChem	www.applichem.com
Bayer	www.gesundheit.bayer.de
B.Braun	www.bbraun.de
BioLegend	www.biolegend.com
BIO-RAD	www.bio-rad.com
Carl Roth	www.carlroth.com
Cell Signalling Technology	https://en.cellsignal.de/
Eurofins	www.eurofinsgenomics.eu
GE Healthcare	www.gelifesciences.com
GERBU	www.gerbu.de
Illumina	www.illumina.com
MerckMillipore	www.merckmillipore.com
Miltenyi Biotec	www.miltenyibiotec.com
PerkinElmer	www.perkinelmer.com
Polysciences	www.polysciences.com
Qiagen	www.qiagen.com
R&D systems	www.rndsystems.com
Roche	www.lifescience.roche.com
SERVA Electrophoresis GmbH	www.serva.de
Sigma-Aldrich	www.sigmaaldrich.com
Takara Bio	www.takarabio.com
tebu-bio GmbH	www.tebu-bio.com
Thermo Fisher Scientific	www.thermofisher.com
VWR®, part of Avantor	https://de.vwr.com/

4.1.2 Reagents for animal experimentation

Table 2. Reagent for animal experimentation.

Reagent	Company	Catalog number
Bepanthen® eye cream	Bayer	-
CleanCap Cas9 mRNA	tebu-bio	L-7206-20
Ketavet	Pfizer	-
Liberase™ TM Research Grade	Roche	05401127001
Liver Digestion Medium	Thermo Fisher Scientific	17703034
Liver Perfusion Medium	Thermo Fisher Scientific	17701038
NaCl (0.9% solution)	B.Braun	-
Rompun 2%	Bayer	-
Tamoxifen	Sigma-Aldrich	T5648

4.1.3 Bacterial stains and cell lines

Table 3 Bacterial stains and cell lines.

Cell	Source	Catalog number
E.coli DH5α	Thermo Fisher Scientific	18265017
E.coli stbl3	Thermo Fisher Scientific	C737303
E.coli ccdB Survival™ 2 $T1^R$	Thermo Fisher Scientific	A10460
BEND3	ATCC	CRL-2299
HEK293	ATCC	CRL-1573
HEK293T	ATCC	CRL-11268
NIH3T3	ATCC	CRL-1658

4.1.4 Cell culture reagents

Table 4. Cell culture reagents.

Reagent	Company	Catalog number
Blasticidin S HCl (10 mg/mL)	Thermo Fisher Scientific	A1113903
DMEM, high glucose, GlutaMAX™	Thermo Fisher Scientific	61965059
Dimethylsulfoxide (DMSO)	AppliChem	A3672,0050
Dulbecco's phosphate buffered saline (PBS)	Sigma-Aldrich	D8537
Fetal bovine serum (FBS)	HyClone	SV30160.03
Iscove's Modified Dulbecco's Medium (IMDM)	Sigma-Aldrich	I3390
Penicillin-Streptomycin	Sigma-Aldrich	P4333

Table 4. Cell culture reagents – continued

Reagent	Company	Catalog number
Polyethylenimine(PEI)	Polysciences	23966
Polybrene	MerckMillipore	TR-1003-G
Puromycin Dihydrochloride	Thermo Fisher Scientific	A1113803
RPMI 1640 Medium, GlutaMAX™	Thermo Fisher Scientific	61870044
Trypan Blue Solution, 0.4%	Thermo Fisher Scientific	15250061
Trypsin – EDTA solution (10x)	Sigma-Aldrich	T4174

4.1.5 Primers and Oligonucleotides

Table 5. Primers and Oligonucleotides.

Oligo name	Application	Sequence
Actin-F	Genotyping PCR control	CAATGGTAGGCTCACTCTGGGAGATGATA
Actin-R	Genotyping PCR control	AACACACACTGGCAGGACTGGCTAGG
Cre-F	Cdh5-cre/ERT2 mice genotyping	GCCTGCATTACCGGTCGATGCAACGA
Cre-R	Cdh5-cre/ERT2 mice genotyping	GTGGCAGATGGCGCGGCAACACCATT
Tie1-flox-F	$Tie1^{fl/fl}$ mice genotyping	ATGCCTGTTCTATTTATTTTTCCAG
Tie1-flox-R	$Tie1^{fl/fl}$ mice genotyping	TCGGGCGCGTTCAGAGTGGTAT
Tie1-R747E-F	$Tie1^{R747E}$ mice genotyping	CTTCCACCTTACCCCCAACC
Tie1-R747E-R	$Tie1^{R747E}$ mice genotyping	GGACAGTTTCCCAGAGAGGC
mTie1 D741G Fw	Tie1-WT cloning	GCAGAGTGAGGGCCCAGTCCGAG
mTie1 D741G Rv	Tie1-WT cloning	CTCGGACTGGGCCCTCACTCTGC
mTie1 D307G Fw	Tie1-WT cloning	GCATGTGCACCTGGTCATTTTGGGGCTG
mTie1 D307G Rv	Tie1-WT cloning	CAGCCCCAAAATGACCAGGTGCACATGC
mTie1 R744A Fw	Tie1 mutant cloning	GTGAGGGCCCAGTCGCAGAAAGCCGGGCAGC
mTie1 R744A Rv	Tie1 mutant cloning	GCTGCCCGGCTTTCTGCGACTGGGCCCTCAC
mTie1 R744E Fw	Tie1 mutant cloning	GTGAGGGCCCAGTCGAAGAAAGCCGGGCAGC
mTie1 R744E Rv	Tie1 mutant cloning	GCTGCCCGGCTTTCTTCGACTGGGCCCTCAC
mTie1 R747A Fw	Tie1 mutant cloning	AGTCCGAGAAAGCGCGGCAGCTGAAGAAGG
mTie1 R747A Rv	Tie1 mutant cloning	CCTTCTTCAGCTGCCGCGCTTTCTCGGACT
mTie1 R747E Fw	Tie1 mutant cloning	AGTCCGAGAAAGCGAGGCAGCTGAAGAAGG
mTie1 R747E Rv	Tie1 mutant cloning	CCTTCTTCAGCTGCCTCGCTTTCTCGGACT

Table 5. Primers and Oligonucleotides- continued.

Oligo name	Application	Sequence
mTie1 R744A R747A Fw	Tie1 mutant cloning	GTGAGGGCCCAGTCGCAGAAAGCGCGGC AGCTGAAGAAGG
mTie1 R744A R747A Rv	Tie1 mutant cloning	CCTTCTTCAGCTGCCGCGCTTTCTGCGACT GGGCCCTCAC
mTie1 R744E R747E Fw	Tie1 mutant cloning	GTGAGGGCCCAGTCGAAGAAAGCGAGGC AGCTGAAGAAGG
mTie1 R744E R747E Rv	Tie1 mutant cloning	CCTTCTTCAGCTGCCTCGCTTTCTTCGACTG GGCCCTCAC
mTie1-gRNA	CRISPER/Cas9	TTAATACGACTCACTATAGGGAGGGCCCAG TCCGAGAAAGC
T7_gRNA_fw	IVT	TTAATACGACTCACTATAGGGAGGGCCCAGTCC GAGAAAGC
T7_sgRNA_rev	IVT	AAAAGCACCGACTCGGTGCC

4.1.6 Plasmids

Table 6. Plasmids.

Plasmid	Source
mTie2-His-HA (geneart)	Thermo Fisher Scientific
pCMV-SPORT6-mTie1 MGC(BC046452)	GE Healthcare Dharmacon
pLenti6.2/V5-DEST™ Gateway™ Vector	Thermo Fisher Scientific
pLenti6.2-mTie1-WT-V5	This project
pLenti6.2-mTie1-R744A-V5	This project
pLenti6.2-mTie1-R744E-V5	This project
pLenti6.2-mTie1-R747A-V5	This project
pLenti6.2-mTie1-R747E-V5	This project
pLenti6.2-mTie1- R744A/R747A-V5	This project
pLenti6.2-mTie1- R744E/R747E-V5	This project
pLenti PGK Puro DEST	Addgene
pLenti-mTie2-His-HA	This project
pMD2.G	Addgene
psPAX2	Addgene
pX330	Addgene

4.1.7 TaqMan™ assays

Table 7. TaqMan probe ID.

Target genes	Assay ID
Ace2	Mm01159006_m1
Actb	Mm00607939_S1
Angpt2	Mm00545822_m1
Axin2	Mm00443610_m1
CD9	Mm00514275_g1
Cdk1	Mm00772472_m1
Esm1	Mm00469953_m1
Fgfr2	Mm01269930_m1
Foxo1	Mm00490671_m1
IL33	Mm00505403_m1
Lcp2	Mm01187570_m1
Lgr5	Mm00438890_m1
Lhx6	Mm01333348_m1
Lyve1	Mm00475056_m1
PDGFb	Mm00440677_m1
Peg10	Mm01167724_m1
SDC1	Mm00448918_m1
Sox9	Mm00448840_m1
STAT3	Mm01219775_m1
Tbx3	Mm01195726_m1
Tie1	Mm00441786_m1
TIMP3	Mm00441826_m1
VEGFR3 (Flt4)	Mm01292604_m1
Wnt11	Mm00437328_m1
Wnt2	Mm00470018_m1
Wnt2b	Mm00437330_m1
Wnt4	Mm01194003_m1
Wnt5a	Mm00437347_m1
Wnt5b	Mm01183986_m1

Table 7. TaqMan probe ID – continued.

Target genes	Assay ID
Wnt7b	Mm01301717_m1
Wnt9a	Mm00460518_m1
Wnt9b	Mm00457102_m1

4.1.8 PCR and RT-qPCR reagents

Table 8. PCR and RT-qPCR reagents.

Kits	Company	Catalog number
DirectPCR® DNA Extraction System	VWR	732-3256
Nuclease-Free Water	Qiagen	129114
RedTaq® ReadyMix™ PCR Reaction Mix	Sigma-Aldrich	R2523-100RXN
Power SYBR™ Green PCR Master Mix	Thermo Fisher Scientific	4368708
PrimePCR Tie2 signalling pathway	Bio-rad	10029683
PrimeSTAR® GXL DNA Polymerase	Takara	R050A
Proteinase K	Gerbu	1344
SsoAdvanced™ Universal SYBR® Green Supermix	Bio-rad	1725271
TaqMan® Fast Advanced PCR Master Mix	Thermo Fisher Scientific	4444965

4.1.9 SDS-PAGE and Western blot reagents

Table 9. SDS-PAGE and Western blot reagents.

Reagent	Company	Catalog number
Ammonium Persulfate (APS)	Carl Roth	9592.2
PageRuler™ Plus Prestained Protein Ladder	Thermo Fisher Scientific	26619
Protein G Sepharose 4 Fast Flow resin	GE Healthcare	17061801
ReBlot Plus Strong Antibody Stripping Solution	MerckMillipore	2504
ROTIPHORESE® 30 % solution (37.5:1)	Carl Roth	3029.1
Sodium dodecyl sulphate (SDS) 20%	Carl Roth	1057.1
Tetramethylethylenediamine (TEMED)	Carl Roth	2367.3
Tris	Carl Roth	4855.2

4.1.10 Staining reagents

Table 10. Staining reagents.

Reagent	Company	Catalog number
Fluorescence Mounting Medium	Agilent Dako	S302380-2
FxCycle™ Violet Stain	Thermo Fisher Scientific	F10347
Hoechst 33342	Thermo Fisher Scientific	H3570
Paraformaldehyde (PFA)	Sigma-Aldrich	P6148
Sucrose	Sigma-Aldrich	84100
Target Retrieval Solution, pH 6	Agilent Dako	S1699
TSA Plus Cyanine 5 System	PerkinElmer	NEL745001KT
ViewRNA™ Tissue Assay Core Kit	Thermo Fisher Scientific	19931
Wnt9b ViewRNA Tissue Probe Set	Thermo Fisher Scientific	VB1-15880-VT
Zenon™ Alexa Fluor™ 488 Rabbit IgG	Thermo Fisher Scientific	Z25302

4.1.11 Antibodies

Table 11. Primary antibodies. *H: Human; M: Mouse; R: Rat; Rb:Rabbit; Hm:Hamster; Mk: Monkey; Mi: Mink; C: Chicken; Dm: D. melanogaster; X: Xenopus; Z: Zebrafish; B: Bovine; Dg: Dog; Pg: Pig; Sc: S. cerevisiae; Ce: C. elegans; Hr: Horse; G: Goat; All: All Species Expected.*

Antigen	Reactivity	Species	Clone	Conjugate	Company	Catalog
α/β-Tubulin	H M R Mk Z B	R	-	-	Cell Signalling	2148S
CD117 (cKit)	M	R	2B8	APC	BioLegend	105812
CD141 (BDCA-3)	M	M	REA964	PE	Miltenyi	130-116-094
CD31	M	R	MEC13.3	PE/Cy7	BioLegend	102524
CD45.2	M	M	104	AF488	BioLegend	109816
Glutamine Synthetase	M R Mk	Rb	-	-	Abcam	ab49873
LYVE-1	H M R	Rb	-	-	Novus Biologicals	NB600-1008
Na-K-ATPase	H M R	Rb	EP1845Y	-	Abcam	ab76020
TIE1	M	G	-	-	R&D	AF619
TIE1	H M	H	39	-	Eli Lilly	-
TIE2	M	G	-	-	R&D	AF762

Table 12. Secondary antibodies. *AF: Alexa Fluor; HRP: horseradish peroxidase*

Reactivity	Species	Conjugate	Company	Catalog
Goat IgG	Donkey	AF 568	Thermo Fisher Scientific	A-11057
Goat IgG	rabbit	HRP	Agilent Dako	P0160
Mouse IgG	rabbit	HRP	Agilent Dako	P0260
Rabbit IgG	Donkey	AF 647	Thermo Fisher Scientific	A-31573
Rabbit IgG	goat	HRP	Agilent Dako	P0448

4.1.12 Kits

Table 13. Kits.

Kits	Company	Catalog number
Arcturus™ PicoPure™ RNA Isolation Kit	Thermo Fisher Scientific	KIT0214
DNA 1000 Kit	Agilent	5067-1504
Gateway™ BP Clonase™ II Enzyme mix	Thermo Fisher Scientific	11789020
Gateway™ LR Clonase™ II Enzyme mix	Thermo Fisher Scientific	11791020
GenElute™ Mammalian Total RNA Purification Kit	Sigma-Aldrich	RTN350
Micro BCA™ Protein Assay Kit	Thermo Fisher Scientific	23235
NE-PER™ Nuclear and Cytoplasmic Extraction Reagents	Thermo Fisher Scientific	78833
Pierce™ Chromatin Prep Module	Thermo Fisher Scientific	26158
QIAquick PCR Purification Kit	Qiagen	28106
QuantiTect Rev. Transcription Kit	Qiagen	205313
QuikChange II XL Site-Directed Mutagenesis Kit	Agilent	200521
Qubit™ dsDNA HS Assay Kit	Thermo Fisher Scientific	Q32854
Qubit™ RNA HS Assay Kit	Thermo Fisher Scientific	Q32852
RNA 6000 Pico Kit	Agilent	5067-1513
TruSeq® Stranded mRNA Library Prep	Illumina	20020594

4.1.13 Other reagents

Table 14. Other reagents.

Reagent	Company	Catalog number
Pierce™ Phosphatase Inhibitor Mini Tablets	Thermo Fisher Scientific	A32957
Protease-Inhibitor Mix HP	SERVA	39106.03
RIPA Lysis and Extraction Buffer	Thermo Fisher Scientific	89900

Table 14. Other reagents – continued

Reagent	Company	Catalog number
SuperSignal™ West Atto Ultimate Sensitivity Substrate	Thermo Fisher Scientific	A38555
SuperSignal™ West Pico PLUS Chemiluminescent Substrate	Thermo Fisher Scientific	34577

4.1.14 Solutions and buffers

Table 15. Solutions and buffers.

Solution/Buffer		Composition
7M Urea lysis buffer	7M	Urea
	100 mM	Tris-HCl pH 8.5
	1% (v/v)	Triton X-100
	1 mM	$MgCl_2$
	10 U/ml	DNase I
	1%	Benzonase
	1mM	Na_3VO_4
	1 X	Phosphatase inhibitors mix
	1 X	Protease Inhibitor Mix
Ammonium chloride potassium (ACK) buffer, pH 7.2-7.4	150 mM	NH_4Cl
	10 mM	$KHCO_3$
	100 mM	EDTA
FACS buffer (in PBS)	0.5 % (w/v)	BSA
	2 mM	EDTA
	1.34 M	NaCl
Phosphate buffered saline (PBS), pH 7.4	27 mM	KCl
	200 mM	Na_2HPO_4
	4.7 mM	KH_2HPO_4
Tris-Buffered Saline Tween-20 (TBS-T)	10 mM	Tris-HCl pH 7.5
	100 mM	NaCl
	0.1%	Tween-20

Table 15. Solutions and buffers – continued

Solution/Buffer		Composition
Tris-Glycine SDS Running Buffer, pH 8.3	25 mM	Tris
	192 mM	Glycine
	0.1% (w/v)	SDS
Tris-Glycine Transfer Buffer, pH 8.3	25 mM	Tris
	192 mM	Glycine
	20% (v/v)	Methanol

4.1.15 Consumables

Table 16. Consumables.

Consumable	Company
384 well qPCR plates	4titute
Cell culture dishes	TPP
Cell scraper	Corning
Cell strainer	BD Falcon
FACS tubes	BD Falcon
Filter containing pipette tips	Sarstedt
Counting Chambers, Neubauer	Sigma-Aldrich
Needles	BD
Microscope cover glasses	VWR international
Microscope glass slides	Menzel-Gläser
Peel-A-WayTM Embedding Molds	Sigma-Aldrich
Pipette tips	Nerbe
Reaction tubes (0.5ml, 1.5ml, 2ml, 5ml)	Eppendorf
Reaction tubes (15ml, 50 ml)	Greiner
Sealing foil	Applied Biosystems
Surflo™ Winged Infusion Sets 27G	VWR international
Sterile pipettes	Corning
Syringes	Dispomed
Terumo® Syringe (1 ml, 5ml, 10 ml)	Terumo
Tissue culture 6 well/24 well plates	Sarstedt

4.1.16 Equipment

Table 17. Equipment.

Equipment	Company
Agarose gel documentation system	Peqlab
AmershamTM Imager 600	GE Healthcare
Axio ScanZ7.1	Zeiss
BioRad gel casting system	BioRad
BioRad gel running system	BioRad
BioRad Western Blotting equipment	BioRad
Cell culture hood	Thermo Fisher Scientific
Cell culture incubator	Thermo Fisher Scientific
Centrifuge	Thermo Fisher Scientific
FACS Aria Fusion	BD
Freezing box	Thermo Fisher Scientific
Heating block	Eppendorf
iMarkTM Microplate Reader	BioRad
Leica TCS SP5 / SP8	Leica
Light cycler 480	Roche
Magnetic stand	Thermo Fisher Scientific
Microtome Hyrax C50	Zeiss
Multistep pipette	Eppendorf
Nanophotometer® N60	INTAS
Pipettes	ErgoOne
pipetteboy	Integra
Power supply	BioRad
QIAxcel Advanced System	Qiagen
Scale	Ohaus
Special accuracy weighing device	Mettler Toledo
Surgery and dissection tools	Fine Science Tools
Table centrifuge (5417R)	Eppendorf
Thermocycler	Applied Biosystems
Shaver	Moser

Table 17. Equipment - continued

Equipment	Company
UV transluminator	Intas
Vortex	Neolab
Water bath	Julabo

4.1.17 Software and webtools

Table 18. Software and webtools

Software/Webtools	Source
Biorender	https://biorender.com
FACSDivaTM	BD
Fiji	https://imagej.net/Fiji
FlowJo	BD
Galaxy	DKFZ internal Galaxy instance
Gephi	gephi.org
Gitools	http://www.gitools.org/
Graph Pad Prism (v8.0)	Graph Pad
Illustrator	Adobe
Leica Application Suite X	Leica
Light Cycler 480 software	Roche
Rstudio	https://rstudio.com/
ZEN black	Zeiss

4.2 Methods

4.2.1 Mouse experiments

Tie1$^{tm1.1Scba}$ (MGI:4441288)(Qu et al., 2010), Stat3^{tm2Aki} (MGI:1926816)(Takeda et al., 1998), or Foxo1^{tm1Rdp} (MGI:3698867)(Paik et al., 2007) transgenic mice, carrying floxed alleles of *Tie1*, *Stat3* or *Foxo1*, respectively, were crossed with Tg(Cdh5-cre/ERT2)1Rha mice (MGI:3848982)(Wang et al., 2010) expressing tamoxifen inducible Cre recombinase under the Cdh5 promoter, to obtain inducible endothelial specific knock out (iECKO) mice for *Tie1*, *Stat3* and *Foxo1*. Tie1^{R747E} mice were generated in this study as described in the following section. C57BL/6N mice were purchased from Janvier Labs. Mice were housed at the Laboratory Animal Facility in the German Cancer Research Centre (DKFZ) under specific pathogen-free conditions.

All animal experiments were approved by the institutional and governmental Animal Care and Use Committees from Regierungspräsidium Karlsruhe, Germany. All experiments were performed in accordance with the institutional guidance for the care and use of laboratory animals.
To induce EC-specific gene deletion, mice were intraperitoneally injected with 2 mg/mouse of tamoxifen (Merck) dissolved in 100 µl of peanut oil (Merck) for 5 consecutive days at 4-6 weeks. Treated mice were used for experiments after adulthood (8 weeks). Littermates of Cre- genotypes were used as control for Cre+ experimental group.

4.2.2 Partial hepatectomy

Two-third partial hepatectomy (PHx) was performed according to the method described by Mitchell and Willenbring to induce liver regeneration(Mitchell and Willenbring, 2008, 2014). In brief, mice were anaesthetized with a mixture of ketamin (100 mg/kg body weight) and xylazine (10 mg/kg body weight) by intraperitoneal injection. After resection of falciform and triangle ligaments, the left lateral lobe was ligated with 4-0 silk sutures (Ethicon) and resected. Subsequently, the median lobe was ligated with suture between the gall bladder and suprahepatic vena cava and then resected. During and after surgery, the mice were maintained on a heating pad until waking-up. Metamizole was used as post-surgical analgesic treatment for the first 48 h post-surgery. Mice were euthanized at indicated time points to monitor liver regeneration by determining the liver to body weight ratio.

4.2.3 In vivo blocking experiments

The following blocking antibodies or corresponding IgG controls were diluted in saline solution and injected intravenously at the indicated dosage: anti-Tie1 (clone Tie1-39, Eli Lilly) was provided by Eli Lilly and used at 8 mg/kg. Anti-VEGFR2 (clone DC101, Bio X Cell) 4 mg/kg; anti-VEGFR3 (clone AFL4, Biolegend) 4 mg/kg; anti-Dll4 (clone HMD4-2, Bio X Cell) 4 mg/kg; anti-CD31 antibody (clone MEC13.3 and clone 390, Biolegend) 4 mg/kg; anti-Integrin-αV (clone RMV-7, Biolegend) 4 mg/kg; anti-Integrin-α5 (clone HMα5-1, Biolegend) 4 mg/kg. Injected mice were sacrificed at the indicated time points.

4.2.4 Liver perfusion and isolation of liver non parenchymal cells (NPC)

Liver cell isolation was adapted to minimize flow shear stress and preserve protein phosphorylation (Mederacke et al., 2015). In brief, a 27 G Surflo infusion catheter (Terumo) connected to the tubing system of an IPC pump (Ismatec) was fixed into the vena cava. The liver was perfused with 37°C pre-warmed liver perfusion medium (Gibco) at 4 ml/min for 1 min, followed by 37°C pre-warmed liver digestion medium (Gibco) supplemented with 40 µg/ml Liberase™ TM (Roche) at 2.7 ml/min for 8 min. The portal vein was cut shortly after the beginning of perfusion to allow blood drainage. After perfusion, livers were explanted into a Petri dish with pre-warmed RPMI medium (Gibco) with 1 mM sodium orthovanadate (Sigma). After removing the liver capsule membrane, tissue was dissociated by gently shaking in a final volume of 40 ml of RPMI. Dissociated liver cells were collected and filtered through a 100 µm cell strainer, centrifuged twice at 50g for 3 min at 4°C and the supernatant containing the NPC was collected. The NPC solution was

centrifuged at 300g for 10 min at 4°C. The pellet was washed once in ACK buffer and finally spun at 400g for 5 min to obtain the final NPC pellet. All steps following perfusion were performed on ice in buffers supplemented with 1 mM sodium orthovanadate.

4.2.5 Positive selection of liver endothelial cell (L-EC)

NPC from 30 mice were pooled as a single biological replicate and further processed for L-EC enrichment. Approximately $3x10^8$ NPC were resuspended in 4.5 ml of MACS buffer containing 2mM EDTA, 0.5% BSA, phosphatase inhibitor (Thermo fisher, A32957) and stained with 500 µl of mouse CD146 MicroBeads (Miltenyi Biotec, 130-092-007), for 15 min on ice. NPC were washed twice in cold MACS buffer, resuspended in 5 ml and loaded on a LS column (Miltenyi Biotec, 130-042-401). The column was washed twice and then eluted with 3 ml MACS buffer. Typically, 30 pooled mice yielded approximately $1.2X10^8$ L-EC with purity above 95% and a viability above 90%.

4.2.6 L-EC flow cytometry and cell sorting

The single cell suspension was stained on ice for 20 min with CD31 PE-Cy7 (BioLegend), CD45 FITC (BioLegend), CD117(c-Kit) APC (BioLegend) and CD141 (Thrombomodulin) PE (Miltenyi Biotec), washed twice and resuspended in 5 ml of FACS buffer. Stained cells were sorted by FACSAria sorter (BD Biosciences) using a 70 µm nozzle.

To obtain L-EC of different zones along the portal-central axis, FACS events were screened through the following nested gates: (1) plotting forward side scatter area (FSC-A) against side scatter area (SSC-A) to exclude large clusters and small debris; (2) singlets-set by excluding the margins of FSC-A and FSC-H width plot; (3) live cell gates according to the FxCycle™ Violet stain; (4) EC, by gating CD31-positive and CD45-negative population, and (5) portal, peri-portal, peri-central and central ECs, inferred from the CD117 histogram. To cross-check the gating of CD117, we used an additional central vein landmark gene CD141 to check that its fluorescence intensity was proportional to CD117.

4.2.7 One-cell embryo microinjection

The *in vivo* one-cell embryo microinjection was performed by Frank van der Hoeven and Ullrich Kloz (Transgenic Service, DKFZ). Briefly, C57BL/6N female mice (5-8 weeks old) were super ovulated and mated overnight with C57BL/6N male mice (older than 7 weeks). On the next day, zygotes were harvested from the ampullae of super ovulated females. The gRNA 50 ng/µl, Cas9 mRNA 100 ng/µl and the DNA template (CCACAATCTGTCCCTCCCTGTGTCTAGGGCTGCAGAGTGAGGGCCCAGTCCGAGAAAGCGAGGCAGCTGAAGAA GGCCTGGATCAGCAGCTGGTCCTGGCTGTGGTAGGTTCCGTCTCTG) 100 ng/µl were injected into the cytoplasm of zygotes. injected zygotes were cultured for 24 hours before oviduct transfer in mouse embryo culture medium KSOM. The delivered mice were screened for mutations by PCR amplification of the mutated region as described in the next session (4.2.8 Genotyping).

4.2.8 Genotyping

Genotyping was performed by PCR of genomic DNA from mouse ear biopsy, lysed in 100 µl Direct PCR Lysis Reagent (VWR) with 10 µg Proteinase K (Gerbu) overnight at 55°C and afterwards heated at 95°C for 20 min to inactivate the enzyme.

Tie1 floxed site was genotyped with Tie1-flox-F(ATGCCTGTTCTATTTATTTTTCCAG) and Tie1-flox-R (TCGGGCGCGTTCAGAGTGGTAT), resulting in a wild-type band of 150bp and a mutant band of 200bp.

VE-cadherin-CreERT2 line was genotyped with Cre-F (GCCTGCATTACCGGTCGATGCAACGA), Cre-R(GTGGCAGATGGCGCGGCAACACCATT), Actin-F (CAATGGTAGGCTCACTCTGGGAGATGATA) and Actin-R (AACACACACTGGCAGGACTGGCTAGG), resulting in actin control band at 300bp and Cre positive band at 390bp.

$Tie1^{R747E}$ mutation was genotyped with Tie1-R747E-F (CTTCCACCTTACCCCCAACC) and Tie1-R747E-R (GGACAGTTTCCCAGAGAGGC), followed by PCR purification with QIAquick PCR Purification Kit (Qiagen) and enzyme digestion of the PCR product by FastDigest Msp I (Thermo Fisher Scientific). The wide type results in 3 bands of 371bp, 248bp and 200 bp, the R747E mutant two bands of 629bp and 200 bp, and the heterozygout four bands of 629bp, 371bp, 248bp and 200 bp. The mutation was further confirmed by sequencing with the same PCR primer.

4.2.9 Cloning

The mouse Tie1 (mTie1) cDNA vector pCMV-SPORT6-mTie1 MGC (BC046452) carries two mutation site and was mutated back to the Tie1-WT sequence with QuikChange II XL Site-Directed Mutagenesis Kit (Agilent) following the manufacturer's instructions by two rounds of site-directed mutations with the following two sets of primers: i). mTie1 D741G Fw and mTie1 D741G Rv ii). mTie1 D307G Fw and mTie1 D307G Rv (Table 5).

The mTie1 mutants' cDNA vectors was derived from the Tie1-WT vector by site-directed mutation with the QuikChange II XL Site-Directed Mutagenesis Kit by the primers listed in Table 5.

The mouse Tie2 (mTie2) cDNA vector was obtained from GeneArt Gene Synthesis (Thermo Fisher Scientific).

The cDNA vectors then were cloned into the entry vector pLenti6.2/V5-DEST™ Gateway™ Vector (Thermo Fisher Scientific) or pLenti PGK DEST Puro (Addgene) with the Gateway cloning system (Thermo Fisher Scientific).

Guide RNA (gRNA) was cloned into the pX330 SpCas9 vector following the protocol from Zhang Lab (https://www.addgene.org/crispr/zhang/).

To obtain the mTie1 gRNA for embryo injection, T7 promoter was added to gRNA by PCR amplifications using primer T7_gRNA_fw and T7_sgRNA_rev (Table 5). The T7-gRNA PCR product was gel purified by Qiaquick gel extraction kit (Qiagen). 350 ng of the PCR product were used as template for in vitro transcription (IVT) using MEGAshortscript T7 kit (Thermo Fisher Scientific) according to manufacturer´s

instructions. Then gRNA was purified by MEGAclear kit (Thermo Fisher Scientific) and eluted in RNase-free water according to manufacturer´s guidelines.

4.2.10 Cell culture

All cell types were maintained at 37°C under sterile conditions, high humidity and 5% CO_2 and were checked regularly for mycoplasma contamination. BEND3 and HEK293 were cultured in DMEM, high glucose, GlutaMAX™ (Thermo Fisher Scientific) medium supplemented with 10% fetal bovine serum (FBS) and 1% penicillin/streptomycin (P/S). HEK293T (for lentivirus production) were cultured in Iscove's Modified Dulbecco's Medium (IMDM) (Sigma-Aldrich) supplemented with 10% fetal bovine serum (FBS) and 1% penicillin/streptomycin (P/S). To overexpress mTie1, mTie2 and the mTie1 mutants, HEK293 were seeded in 6 well plate and transduced with the corresponding lentivirus with 10ug/ml polybrene (MerckMillipore) and selected with 10ug/ml blasticidin or puromycin (Thermo Fisher Scientific).

4.2.11 Lentivirus production

The lentiviruses were produced following the protocol from Addgene (https://www.addgene.org/protocols/lentivirus-production/). Briefly, HEK293T cells were seeded in 15 cm dishes (4×10^6 cells per dish). Two days later, they were triple-transfected with (i) lenti-overexpression vector (ii) pMD2.G plasmid (iii) the psPAX2 using PEI transfection reagent. One day after transfection, fresh medium was changed and the supernatant was collected on the second and third day after transfection. The supernatant containing the lentivirus particles was filtered through a 0.22 µM filter system (Sigma) and then ultra-centrifugated at 20.000 g for 2h at 4°C. The pellet was dissolved in PBS and aliquots were stored at -80°C until further use.

4.2.12 Bulk RNA-sequencing and analysis pipeline

RNA extraction from sorted cells was performed with PicoPure™ RNA Isolation Kit (Thermo Fisher Scientific) and DNA was removed by on-column treatment with DNase I (RNase-Free DNase Set, Qiagen) according to the manufacturer's instructions. RNA integrity was measured by RNA 6000 Pico Kit (Agilent) on Bioanalyzer 2100 (Agilent) and the concentration was determined by Qubit™ RNA HS Assay Kit (Thermo Fisher Scientific). Only samples with RIN above 8 were used for library preparation. RNA from each sample (350 ng each) was used for library generation using the TruSeq® Stranded mRNA Library Prep kit (Illumina, 20020594). Quality control of the resulting libraries was performed with DNA 1000 Kit (Agilent) on Agilent Technologies 2100 Bioanalyzer and the concentration was determined by Qubit™ dsDNA HS Assay Kit (Thermo Fisher Scientific). 10 nM of 8 libraries was pooled using unique dual (UD) i7 index adapters (IDT for Illumina–Nextera DNA UD Indexes) and sequenced with NextSeq 550 Single-Read 75bp High-Output. Illumina output files were demultiplexed with bcl2fastq2 Conversion Software v2.20 (Illumina). The resulting FASTQ files were analysed on the pipeline built on the DKFZ internal Galaxy instance (Afgan et al., 2018). Adapter sequences were removed by Cutadapt(Martin, 2011) v1.16.6. The trimmed output sequences were aligned to the transcriptome index of the GRCm38.92 (Ensembl) using the RNA STAR

(Dobin et al., 2013) v2.7.2b and gene expression was measured by featureCounts (Liao et al., 2014) v1.6.3. Gene count outputs were normalized to the relative gene length and transcripts per million (TPM) were calculated for each sample for further analysis.

4.2.13 Protein extraction

For label free mass spectrometry, cell pellets were lysed in RIPA lysis and extraction buffer (Thermo Fisher Scientific) supplemented with phosphatase inhibitor and protease inhibitor mix (Serva Electrophoresis) according to manufacturer's instructions. For phospho-enrichment, cell pellets were lysed as previously described (Potel et al., 2018). In brief, the pellet was lysed with 7M urea lysis buffer containing: 100 mM Tris-HCl pH 8.5, 7 M Urea, 1% Triton, 10 U/ml DNase I, 1 mM magnesium chloride, 1% Benzonase (Sigma), 1 mM sodium orthovanadate, phosphatase inhibitors and protease Inhibitor. Dissolved pellets were sonicated at 10% output with 1s-on-1s-off for 1 min on ice (Sonifier W-250 D, G. Heinemann). The residual cell debris was removed by centrifugation at 18,000g for 1h at 4°C. The sample was then incubated for 2 h at room temperature for Benzonase digestion. The protein concentration was determined by the micro BCA™ protein assay kit (Thermo Fisher Scientific) according to the manufacturer's instructions.

4.2.14 Protein digestion and peptide labelling

For label-free mass spectrometry, 10 μg protein extracts were processed via tryptic in-gel digestion. Briefly, proteins were loaded on an SDS-PAGE-gel and ran 0.5 cm in the gel. After Coomassie staining, the sample underwent tryptic digestion as previously described(Shevchenko et al., 2006), adapted to a DigestPro MSi robotic system (INTAVIS Bioanalytical Instruments AG).

For phospho-enrichment, protein reduction and alkylation were done with 10 mM TCEP and 40 mM CAA for 30 min at RT. For each sample, 200 μg protein was digested first by Lys-C at 1:100 enzyme:protein ratio for 4 h at 37°C at pH 8.5. The solution was then diluted 1:5 with 50 mM TEAB (pH 8.5) and further digested with trypsin at 1:50 enzyme:protein ratio over night at 37°C. The digestion was stopped by adding TFA to 0.4% (vol/vol), then centrifuged at 2,500g for 10 min. The supernatants were collected and pH-verified to be below 2 and then processed with SepPak tC18 100 mg 1cc (Waters) for desalting and dimethyl labelling. Briefly, the cartridge was conditioned with 3 ml ACN followed by 1 ml 50% ACN 0.5% HAcO, then equilibrated with 3 ml 0.1% TFA before loading the acidified peptide samples. The samples were washed with 3 ml 0.1% TFA and then 500 µl light labelling reagent (50 mM sodium phosphate buffer pH 7.5, 4% Formaldehyde (CH_2O), 0.6 M Cyanoborohydride ($NaBH_3CN$)). Thereafter, the cartridges were again washed with 3 ml 0.1% TFA and the labelled peptides were eluted with 750 µl 50% ACN 0.5% HAcO. In parallel, an internal control (L-EC pooled from all sorting gates) was processed following the same protocol except labelled with medium labelling reagent (50 mM sodium phosphate buffer pH 7.5, 4% deuterated Formaldehyde (CD_2O), 0.6 M Cyanoborohydride ($NaBH_3CN$)). Equal amount of internal control was spiked into each sample and then the sample/spike mix was vacuum dried before processing for phosphopeptide enrichment.

4.2.15 Phosphopeptide enrichment

An automated phosphopeptide enrichment protocol based on Immobilized metal affinity chromatography (IMAC) using a nitrilotriacetic acid (NTA) chelating ligand functionalized with Fe(III) was applied to the mixture of labelled peptides and internal controls, with AssayMap Bravo platform (Agilent Technologies). Each sample was reconstituted with 110 µL 80% ACN, 0.1% TFA buffer. They were gently sonicated in water bath until complete dissolution and then they were transferred manually to the Greiner 96-well full skirt PolyPro PCR plate. The Agilent AssayMAP Phosphopeptide Enrichment v2.0 App, included with the Agilent AssayMAP Bravo Protein Sample Prep Workbench v2.0 software suite, was run using AssayMAP Fe(III)-NTA cartridges (Agilent Technologies). Briefly, the cartridges were firstly primed with 100 µL 50% ACN, 0.1% TFA, then equilibrated with 50 µL of 80% ACN, 0.1% TFA. Each sample was loaded onto the Fe(III)-NTA cartridges and then they were washed with 50 µL 80% ACN, 0.1% TFA buffer. Finally, phosphopeptides were eluted with 20 µL of 1% NH4OH buffer (pH ~11), acidified with 2 µl of formic acid (pH 3) and dried down for MS analysis.

4.2.16 LC-MS/MS analysis

Nanoflow LC-MS/MS was performed by coupling a Dionex 3000 (Thermo Fisher Scientific) to a QExactive Orbitrap HF-X (Thermo Fisher Scientific). Samples for the proteome or phosphoproteome analysis were re-suspended in loading buffer containing 2.5% 1,1,1,3,3,3-Hexafluoro-2-propanol, 0.1% TFA in water or 50 mM citrate and 0.1% TFA, respectively. Peptide loading and washing were done on a trapping cartridge (Acclaim PepMap300 C18, 5µm, 300Å wide pore, Thermo Fisher Scientific) and washed for 3 min with 0.1% TFA in water at a flow rate of 30 µl/min. Peptide separation was performed on an analytical column (nanoEase, 300Å, 1.7 µm, 75 µm x 200 mm, Waters) at a flow rate of 300 nl/min using a three step 210 min gradient consisting of the following steps: 2-8% solvent B (80% acetonitril, 20% water with 0.1% formic acid) in 15 min, 8-25% in 135 min and 25-40% in 30 min followed by a washing and an equilibration step with solvent A being 0.1% formic acid in water. In order to accompany for the more hydrophilic nature of phospho-peptides, the 210 min method was adjusted as follows: 2-25% solvent B in 150 min, 25-40% in 30 min followed by washing and an equilibration step. Peptides were ionized using a spray voltage of 2.2 kV and a capillary temperature of 275°C. The instrument was operated in data-dependent mode. For the full proteome samples, full scan MS spectra (m/z 375–1,500) were acquired with a maximum injection time of 54 ms at 120,000 resolution and an automatic gain control (AGC) target value of three million charges. MS/MS scans were triggered for the top 35 precursor ions, high-resolution MSMS spectra were acquired in the orbitrap with a maximum injection time of 22 ms at 15,000 resolution (isolation window 1.6 m/z), an AGC target value of 100 000 ions and normalized collision energy of 27. Dynamic exclusion was set to 60 s (16 s phospho samples). Undetermined charge states and single charged species were excluded from fragmentation.

4.2.17 Peptide and protein identification and quantification

Data analysis was carried out by MaxQuant (Tyanova et al., 2016a) v1.6.3.3. Carbamidomethylation of cysteines was set as fixed modification. Phosphorylation of serine, threonine or tyrosine as well as oxidation of methionines and N-terminal acetylation were set as variable modifications. Identification FDR cutoffs were 0.01 on peptide level and 0.01 on protein level.

The LFQ based full proteome analysis was carried out with organism specific UniProt database UP000000589 (*Mus musculus*; Dec, 2017; 60715 sequences) and enabled 'match-between-runs' function. The LFQ option was enabled and left at default parameters.

The phosphoproteome analysis samples was carried out with organism specific UniProt database UP000000589 (Mus musculus; Feb, 2020; 55421 sequences). The multiplicity was set to '2' with 'DimethLys0' and 'DimethNter0' as light labels and 'DimethLys4' and 'DimethNter4' as heavy labels. The 'match-between-runs' function was enabled and fractions were assigned so that the function applied separately within the phospho fractions (fraction 1) and the full proteome fraction (fraction 11). The 'Re-quantify' option was enabled.

4.2.18 Phospho-receptor tyrosine kinase (RTK) array

Mouse phospho-RTK array kits were purchased from R&D systems. Spatially sorted L-EC were lysed with the provided lysis buffer supplemented with phosphatase inhibitor and protease inhibitor mix. Protein concentration was quantified with Micro BCA™ Protein Assay Kit according to the manufacturer's instructions. Protein lysates (30 µg) were loaded for each membrane. The array was performed according to the manufacturer's instructions, except that the Chemi Reagent Mix was replaced with SuperSignal™ West Pico PLUS Chemiluminescent Substrate (Thermo Fisher Scientific). The images were acquired with Amersham™ Imager 600 (GE Healthcare).

4.2.19 RNA extraction, cDNA synthesis and qRT-PCR

RNA extraction from sorted cells was performed with PicoPure™ RNA Isolation Kit (Thermo Fisher Scientific) according to the manufacturer's instructions. Whole liver samples were homogenized by TissueLyzer (Retsch) in lysis solution and RNA extraction was performed with GenElute™ Mammalian Total RNA Purification Kit (Sigma) according to the manufacturer's instructions. Total RNA was reverse transcribed into cDNA using the QuantiTect Reverse transcription kit (Qiagen) according to the manufacturer's instructions. QRT-PCR reaction was performed with TaqMan® Fast Advanced PCR Master Mix (Thermo Fisher Scientific) and read by LightCycler® 480 (Roche). All TaqMan™ probes were purchased from Thermo Fisher Scientific. Gene expression levels were calculated based on the ΔΔCt relative quantification method, normalized to *Actb* expression.

4.2.20 Immunofluorescence and confocal microscopy

Paraffin sections (30 µm) were cut on a HM355S microtome (Thermo Fisher Scientific) and allowed to adhere to Superfrost Plus slides (Thermo Fisher Scientific). Sections were permeabilized and blocked in PBS containing 0.3% Triton X-100 (Sigma-Aldrich) and 10% FBS followed by staining in the same blocking buffer. Cultured cells were plated on coverslip slides, methanol-acetone fixed and blocked in PBS containing 10% FBS. The following primary antibodies were used for staining: goat anti-mouse CD31 (1:100, R&D Systems); rabbit anti-mouse LYVE1 (1:200, Novus Biologicals); rabbit anti-Na-K-ATPase (1:100, Abcam), goat anti-human Tie1 (1:100, R&D Systems). The following secondary antibodies were used for staining: Alexa Fluor 647 donkey anti-rabbit IgG (H+L), Alexa Fluor 568 donkey anti-goat IgG (H+L) (Thermo Fisher Scientific). Rabbit anti-mouse Glutamine Synthetase (Abcam) was directly conjugated with Zenon™ Alexa Fluor™ 488 Rabbit-IgG.

Stained slides were mounted with Fluorsave (Merck Millipore) and images were acquired on an inverted Leica microscope (TCS STED CW SP8, Leica Microsystems) with a motorized stage for tiled imaging. To minimize fluorophore spectral spillover, we used the Leica sequential laser excitation and detection modality. The bleed-through among sequential fluorophore emission was removed applying simple compensation correction algorithms to the acquired images. Lif files were imported into Imaris (Bitplane) for background adjustment and exported as tiff images.

4.2.21 Fluorescence *in situ* hybridization (FISH)

FISH of Wnt9b was performed using the ViewRNA ISH Tissue Assay Core Kit (Thermo Fisher Scientific). Cryosections (7 µm) were fixed with 4% paraformaldehyde overnight in the dark at 4°C. The sections were then washed with PBS, dehydrated in ethanol, baked for 1h at 60 ◦C, boiled for 15 min in pre-treatment solution from the kit, and digested for 15 min in protease solution provided by the manufacturer (Thermo Fisher Scientific). Following protease treatment, the sections were hybridized for 2 h at 40°C with the Wnt9b (VB1-15880-VT) probe (Thermo Fisher Scientific). The hybridized sections were pre-amplified and amplified according to the manufacturer's manual. For visualization of the FISH probe, the labelled probe conjugated to alkaline phosphatase type 1 and fast red substrate was treated to detect Wnt9b expression (Thermo Fisher Scientific). Immunofluorescent (IF) co-staining of glutamine synthetase was immediately performed after the initial FISH steps. Briefly, the sections were blocked, stained with rabbit anti-mouse Glutamine Synthetase antibody (AbCam) followed by AF647 goat anti-rabbit (Thermo Fisher Scientific) for secondary detection. Images were acquired as described before for the confocal microscopy.

4.2.22 Data analysis

4.2.22.1 Dataset filtering and processing

For gene expression out of 28,727 identified genes, we considered for further analysis (pathway enrichment, phylogenetic tree, PTR definition) only genes with a mean TPM of the four replicates above

5 in at least one of the four zones (PN, PP, PC, CV). In order to provide an overview of the transcriptome zonation, the TPM cut-off was maintained at 1 and the expression profiles were confirmed by qRT-PCR.

Of 5,015 detected proteins, only those quantified in at least two replicates in one of the zones were retained for imputation. The label-free quantification (LFQ) intensities were imputed with a constant (the minimal LFQ of each sample) for missing values. To normalize the variability among the experimental replicates, the values of each pool across the four zones were normalized to their mean. Finally, where protein abundance was required, the normalized value was multiplied for the mean LFQ of all the 16 samples before normalization.

Of 19,607 detected phospho-sites (p-site) corresponding to 3,447 proteins, only class I (localization probability > 0.75) were considered for analysis. Normalized ratio exported from MaxQuant was used for quantification. As described for proteins, only p-sites quantified in at least two replicates in one of the zones were retained for imputation. The sample/spike ratios were first log2 transformed and then imputed from normal distribution with Perseus v1.6.14.0 (Tyanova et al., 2016b). Finally, normalization between replicates was performed as described for protein analysis.

In order to compare multiple datasets, transcripts, proteins and p-sites were matched with their corresponding ENSEMBL gene ID.

4.2.22.2 Zonation pattern definition

To define if the expression of a specific transcript, protein or p-sites was zonated across zones, we performed Kruskal-Wallis (KW) test, followed by Benjamini–Hochberg (BH) procedure to correct for multiple hypotheses. Transcripts/proteins/p-sites with KW p-value <0.05 and BH FDR <0.25 were considered as zonated.

A zonation score was expressed by Centre-of-Mass (CoM) as described (Ben-Moshe et al., 2019). We defined sorting gate PN as gate1, PP as 2, PP as 3 and CV as 4. Thus, for each pool consisting of the 4 zones, taking mRNA as example,

$$CoM = \frac{1 * TPM[PN] + 2 * TPM[PP] + 3 * TPM[PC] + 4 * TPM[CV]}{TPM[PN] + TPM[PP] + TPM[PC] + TPM[CV]}$$

To calculate for the overall CoM, the mean of each zone was used.

The patterns of the zonation - portal, central, vessel and sinusoidal - for zonated genes were defined as follows: Considering the continuum of the vasculature, two gates were combined. Portal area combined PN and PP, central area combined CV and PC, vessel area combined PN and CV and sinusoidal area combined PP and PC. Thus, each of these areas contained 8 samples. The mean value for each combined area was calculated and the pattern was defined according to which area expressed the maximum mean value. To avoid the confoundment generated by combination of portal and central gates that are not neighbouring gates, thus masking the difference of these gates, we applied a further filtration for vessel and sinusoid pattern. As extreme low and high CoM is indicative for portal or central zonation, the genes CoM <2.2 or >2.8 were excluded for vessel and sinusoidal pattern.

To generate heat maps of the expression profiles, the expression was normalized to the maximum value across all 16 samples. Genes were sorted by their Centre-of-Mass, except for the heat maps for vessel/sinusoid patterns, where log2 fold change of vessel area to sinusoid area was used to order the genes. In order to compare the zonation profiles of different data sets (transcript, protein p-peptides), each zonation profile was represented by percentage of maximum expression. Graph was generated by Gitools (Perez-Llamas and Lopez-Bigas, 2011) v2.3.1.

4.2.22.3 Correlation of spatial sort RNAseq and published scRNAseq

For the comparison of spatial sorting RNAseq with previous scRNAseq of L-EC (Halpern et al., 2018), we matched the two datasets by gene name. Comparison was calculated on the mean fractions of the different repeats in each FACS gate and the mean fractions of all cells assigned to the same liver lobule layer in the scRNAseq data. Zonation FDR on Kruskal-Wallis test was recalculated for number of genes common to the both datasets (n=13,070 genes). We next filtered for zonated genes (FDR qval <0.25 in both datasets), whose dynamic range was greater than 1.2. Dynamic range was defined for each dataset as the ratio between the maximal and minimal expressions of the genes across the different liver lobule layers. To avoid noisy genes, we only considered genes with fraction higher than $5x10^{-6}$ in at least one lobule layer. This filter yielded 2,463 highly expressed zonated genes in the spatial sorting dataset and 76 in the scRNAseq, with common 48 genes intersecting. We then calculated the Centre-of-Mass (CoM) for these 48 genes in each of the data sets and calculated the Pearson correlation ($r_{Pearson}$ = 0.873, p-val = $5.746x10^{-16}$).

4.2.22.4 Correlation of Protein and mRNA abundance

To compare protein and mRNA abundance, we matched the two data sets by their Gene ID. We obtained 4,169 protein-mRNA pairs and protein-to-transcript ratio (PTR) was calculated by building the ratio between average protein and RNA abundance across the zones. The PTR values of the protein-mRNA pairs followed a Gaussian distribution. High PTR or low PTR genes were defined as PTR > median+SD or PTR < median-SD.

4.2.22.5 Comparison of RNA, protein and p-peptides zonation

To compare the zonation of protein and mRNA, data sets were matched by Gene ID. The 4 CoM values corresponding to the 4 replicates was calculated for each data set and unpaired two-sided Student's t test was performed between the 4 CoM relative to mRNA and the 4 CoM relative to protein. The extent of zonation shift was determined by calculating the ΔCoM for each protein-mRNA pair. Finally, the comparison is visualized by plotting the $-\log_{10}$ p-value against the ΔCoM, where genes with p <0.05 and ΔCoM > 0.1 is considering to be differentially zonated between protein and mRNA. The same approach was applied to compare the zonation between p-peptide and protein.

As CoM is not applicable to vessel/sinusoid patterns, when comparing protein and mRNA zonation correlation, portal/central and vessel/sinusoidal patterns were also considered separately, indicated by central or vessel fraction. For any gene (g), the portal fraction was calculated as follows:

$$Central\ fraction\ (g) = \frac{\max\ (PC, CV)}{\max(PN, PP) + \max\ (PC, CV)}$$

Similarly, the vessel fraction was calculated as follows:

$$Vessel\ fraction\ (g) = \frac{\max\ (PN, CV)}{\max(PP, PC) + \max\ (PN, CV)}$$

Spearman correlation was then calculated for the RNA and protein central fractions ($r_{Spearman}$ = 0.38, p-value = 3.02 x 10^{-139}) and vessel fractions ($r_{Spearman}$ = 0.26, p-value = 6.17 x 10^{-66}). For each gene, Spearman's correlation coefficient between protein and mRNA is determined by comparing their mean expression values of each zone, as indicated by the dot colour.

4.2.22.6 Pathway and protein domain analysis

Pathway or protein domain analysis for each indicated subset of genes was performed with STRING (Szklarczyk et al., 2019) v11.0, searching against KEGG (Kanehisa and Goto, 2000) or SMART (Letunic and Bork, 2018) database.

Selected pathways with FDR < 0.01 were represented as dot plot using ggplot2 package(Wickham, 2016) v3.3.1 in RStudio v1.2.5042. Circle size was proportional to gene count and colour indicating the -$\log_{10}$ fdr. Pathways were sorted accordingly to the median CoM, $\log_2$ fold change (FC) and PTR of the genes belonging to each pathway. SMART protein domains were represented as bar graph sorted by median CoM with the bar colour indicating the FDR range.

4.2.22.7 Protein network analysis

Protein-protein interaction networks for both high and low PTR proteins were obtained with STRING (Szklarczyk et al., 2019) v11.0. Network parameters, including the source and the target node defining the direction of the interaction and the combined interaction score defining the weight of the network edge, were imported into Gephi v0.9.2 (Bastian et al., 2009) for the network visualization. Networks were visualized as ForceAtlas 2 with the node size proportional to the LFQ value and edge thickness to the combined interaction score. Nodes and edges relative to specific pathways were coloured as indicated in the figures.

4.2.22.8 Phylogenetic tree analysis of L-EC kinome and phosphatome

Phylogenic analysis was performed with CORAL (Metz et al., 2018) or CORALp (Min et al., 2019) for the L-EC kinome and phosphatome, respectively. The circle size was proportional to the expression indicated by the mean TPM across zones. The colour represented the overall zonation score (CoM) from portal (blue) to central (red). In case of multiple p-peptides corresponding to the same gene, the one with the lowest Kruskal Wallis p-value was selected for the analysis.

4.2.22.9 Differential gene expression analysis

To investigate the gene regulation induced by the receptor tyrosine kinase Tie1 blockade, L-EC was spatially sorted from C57/B6 mice 2 hours after treatment with anti-Tie1 antibody, and processed for RNAseq as described above. To obtain the differentially expressed genes in each zone, the obtained gene counts from Tie1 treated samples and control samples were analysed with the DESeq2 (Yousif et al., 2020).

Gene regulation was visualized as volcano plot by plotting the $-\log_{10}$ q-val against the $\log_2$ fold change with the EnhancedVolcano (Blighe et al., 2019) v1.4.0 package in RStudio. To compare the regulatory effect of Tie1 on portal and central, genes that were significantly regulated in portal or in central, i.e., q-value < 0.05 in at least of one of the two DEseq2 output, were selected and their $-\log_{10}$ q-value was visualized as density plot using ggplot2 package. The difference was determined by Wilcoxon matched-pairs signed rank test (p-value < 2.2×10^{-16}).

4.2.22.10 Wnt9b promoter analysis

Searching for putative transcription factor binding sites in the promoter region of Wnt9b was performed by the Search Motif Tool from the Eukaryotic Promoter Database (SIB) (Dreos et al., 2015). The search was based on the library from Transcription Factor Motifs (JASPAR CORE 2018 vertebrates), retrieved from -1000 to 1000 bp relative to the *Wnt9b* transcription start site with a p-value cut-off at 0.001. Motif was selected for Foxo1 or STAT3, respectively. The retrieved putative binding sites for FoxO1 and STAT3 were indicated as shown in Figure 32a.

4.2.22.11 Phosphosite motif analysis

15-mer sequences were extracted from -7 to +7 position flanking the detected phosphosites. Motif analysis was performed using PhosphoSitePlus (Hornbeck et al., 2015) v6.5.9.2. Sequences for p-S, p-T, p-Y were loaded separately as foreground, searched against the corresponding background. Proline-directed, acidic, basic or other motif categories were classified as previously described (Villen et al., 2007). The sequences that could not be assigned to any aforementioned motif were designated as none. To visualize the consensus sequences flanking the phosphosites for each pattern, sequence logos were generated by PhosphoSitePlus v6.5.9.2. The sequences belonging to each category of each phosphosite were loaded separately as foreground and searched against the respective background of the specific phosphosite, using PST production algorithm.

4.2.23 Statistical analysis

Kruskal-Wallis tests followed by Benjamini–Hochberg correction were performed when comparing multiple groups. Wilcoxon matched-pairs signed rank test or unpaired two-sided Student's t tests were performed when comparing two groups. *, p-value <0.05; **, p-value < 0.01; ***, p-value < 0.001; ****, p-value < 0.0001. Data are expressed as mean $\pm$ SD except in Figure 8 (mean $\pm$ SEM).

5. ABBREVIATIONS

ABIN-2	A20 binding inhibitor of NF-kappaB activation-2
ACK	Ammonium chloride potassium
AF	Alexa Fluor
AFP	Alpha-fetoprotein
ALB	Albumin
Angpt	Angiopoietin
APC	Adenomatous polyposis coli
BBB	Blood-brain barrier
BH	Benjamini–Hochberg
BMP	Bone morphogenetic protein
CAM	Cell adhesion molecule
CaMKII	Calcium/calmodulin-dependent kinase II
CaN	Calcineurin
CCD	Coiled-coil domain
CDK	Cyclin-dependent kinases
CK1α	Casein kinase 1α
CMGC	CDK, MAPK, GSK and CDK-like kinases
CoM	Centre-of-Mass
CV	Central vein
DAG	Diacylglycerol
DLL-4	Delta-like ligand 4
Dvl	Dishevelled
EC	Endothelial cells
ECM	Extracellular matrix
ERK	Extracellular signal regulated kinase
ETS	ETS domain–binding factor
FACS	Fluorescence-activated cell sorting
FAK	Focal adhesion kinase
FBS	Fetal bovine serum
FGF	Fibroblast growth factor
FN	Fibronectin
FOX	Forkhead box
FReD	Fibrinogen-related domain
GATA	GATA-binding factor
GRP	G protein–coupled receptor

GS	Glutamine synthetase
GSK	Glycogen synthase kinase
HOX	Homeobox
HPSG	Heparan sulfate proteoglycans
HRP	Horseradish peroxidase
HSC	Hepatic stellate cells
Ig	Immnunoglobulin
IMAC	Immobilized metal affinity chromatography
IP3	Inositol 1,4,5-triphosphate
JNK	c-Jun N-terminal kinase
KLF	Krüppel-like factor
KW	Kruskal Wallis
L-EC	Liver endothelial cells
LBD	Ligand binding domain
LGR	Leucine-rich repeat-containing G protein–coupled receptor
LRP	Low-density lipoprotein receptor-related protein
LSEC	Liver sinusoidal endothelial cells
MAPK	Mitogen-activated protein kinase
MCM	Minichromosome Maintenance
MOAC	Metal-oxide affinity chromatography
MS	Mass spectrometry
NGF	Nerve growth factor
NICD	Notch intracellular domain
NPC	Non-parenchymal cells
PC	Peri-central
PDGF	Platelet-derived growth factor
PDGFR	PDGF receptor
PI3K	Phosphatidylinositol 3-kinase
PIP2	phosphatidylinositol 4,5 biphosphate
PKC	Protein kinase C
PLC	Phospholipase C
PlGF	Placenta growth factor
PMA	Phorbol-12-myristate-13-acetate
PN	Portal node
PP	Peri-portal
PTM	Post-translational modifications
PTR	Protein-to-Transcript-Rate

RNF43	Ring finger protein 43
ROCK	Rho-associated protein kinase
ROR2	Receptor Tyrosine Kinase Like Orphan Receptor 2
Rspo	R-spondins
RTK	Receptor tyrosine kinases
S1P	Sphingosine-1-phosphate
SCD	Super-clustering domain
scRNAseq	Single cell RNA sequencing
SMC	Smooth muscle cell
SOX	Sex-determining region Y box
TCF/LEF	T cell factor/lymphoid enhancer factor
TF	Transcription factors
TGF-β	Transforming growth factor beta
TK	Tyrosine kinase
TNF	Tumour necrosis factor
VE-PTP	Vascular endothelial phospho-Tyr phosphatase
VEGF	Vascular endothelial growth factor
ZNRF	Zinc and ring finger
βTRCP	β-transducin repeat-containing protein

6. PUBLICATIONS

Inverso, D.*, **Shi, J.***, Lee, K.H., Jakab, M., Ben-Moshe, S., Schneider, M., Wang, G., Kulkarni, S.R., Komeili, M., Argos Vélez, P., Riedel, M., Spegg, C., Ruppert, T., Schaeffer-Reiss, C., Helm, D., Singh, I., Boutros, M., Chintharlapalli, S., Heikenwalder, M., Itzkovitz, S., Augustin, H.G.. "Beyond scRNAseq: A vascular phosphoproteome atlas unveils an angiocrine Tie-Wnt signaling axis in the liver." Under review. ***co-first author**

Singhal, M., Gengenbacher, N., La Porta, S., Gehrs, S., **Shi, J.**, Kamiyama, M., Bodenmiller, D.M., Fischl, A., Schieb, B., Besemfelder, E., Chintharlapalli, S. and Augustin, H.G.. (2020). "Preclinical validation of a novel metastasis-inhibiting Tie1 function-blocking antibody." EMBO Mol Med 12, e11164.

7. REFERENCES

Afgan, E., Baker, D., Batut, B., van den Beek, M., Bouvier, D., Cech, M., Chilton, J., Clements, D., Coraor, N., Gruning, B.A.*, et al.* (2018). The Galaxy platform for accessible, reproducible and collaborative biomedical analyses: 2018 update. Nucleic Acids Res *46*, W537-W544.

Amatu, A., Sartore-Bianchi, A., Bencardino, K., Pizzutilo, E.G., Tosi, F., and Siena, S. (2019). Tropomyosin receptor kinase (TRK) biology and the role of NTRK gene fusions in cancer. Ann Oncol *30 Suppl 8*, viii5-viii15.

Anderson, K.D., Pan, L., Yang, X.M., Hughes, V.C., Walls, J.R., Dominguez, M.G., Simmons, M.V., Burfeind, P., Xue, Y., Wei, Y.*, et al.* (2011). Angiogenic sprouting into neural tissue requires Gpr124, an orphan G protein-coupled receptor. Proc Natl Acad Sci U S A *108*, 2807-2812.

Ang, C.H., Hsu, S.H., Guo, F., Tan, C.T., Yu, V.C., Visvader, J.E., Chow, P.K.H., and Fu, N.Y. (2019). Lgr5(+) pericentral hepatocytes are self-maintained in normal liver regeneration and susceptible to hepatocarcinogenesis. Proc Natl Acad Sci U S A *116*, 19530-19540.

Antoine, M., Wirz, W., Tag, C.G., Mavituna, M., Emans, N., Korff, T., Stoldt, V., Gressner, A.M., and Kiefer, P. (2005). Expression pattern of fibroblast growth factors (FGFs), their receptors and antagonists in primary endothelial cells and vascular smooth muscle cells. Growth Factors *23*, 87-95.

Augustin, H.G., and Koh, G.Y. (2017). Organotypic vasculature: From descriptive heterogeneity to functional pathophysiology. Science *357*.

Augustin, H.G., Koh, G.Y., Thurston, G., and Alitalo, K. (2009). Control of vascular morphogenesis and homeostasis through the angiopoietin-Tie system. Nat Rev Mol Cell Biol *10*, 165-177.

Barker, N., van Es, J.H., Kuipers, J., Kujala, P., van den Born, M., Cozijnsen, M., Haegebarth, A., Korving, J., Begthel, H., Peters, P.J.*, et al.* (2007). Identification of stem cells in small intestine and colon by marker gene Lgr5. Nature *449*, 1003-1007.

Bastian, M., Heymann, S., and Jacomy, M. (2009). Gephi: An open source software for exploring and manipulating networks. Third international AAAI conference on weblogs and social media *8*, 361-362.

Ben-Moshe, S., and Itzkovitz, S. (2019). Spatial heterogeneity in the mammalian liver. Nat Rev Gastroenterol Hepatol *16*, 395-410.

Ben-Moshe, S., Shapira, Y., Moor, A.E., Manco, R., Veg, T., Bahar Halpern, K., and Itzkovitz, S. (2019). Spatial sorting enables comprehensive characterization of liver zonation. Nat Metab *1*, 899-911.

Blache, P., van de Wetering, M., Duluc, I., Domon, C., Berta, P., Freund, J.N., Clevers, H., and Jay, P. (2004). SOX9 is an intestine crypt transcription factor, is regulated by the Wnt pathway, and represses the CDX2 and MUC2 genes. J Cell Biol *166*, 37-47.

Blighe, K., Rana, S., and Lewis, M. (2019). EnhancedVolcano: Publication-ready volcano plots with enhanced colouring and labeling. *DOI: 10.18129/B9.bioc.EnhancedVolcano*.

Browaeys, R., Saelens, W., and Saeys, Y. (2020). NicheNet: Modeling intercellular communication by linking ligands to target genes. Nat Methods *17*, 159-162.

Brunet, A., Bonni, A., Zigmond, M.J., Lin, M.Z., Juo, P., Hu, L.S., Anderson, M.J., Arden, K.C., Blenis, J., and Greenberg, M.E. (1999). Akt promotes cell survival by phosphorylating and inhibiting a Forkhead transcription factor. Cell *96*, 857-868.

Cao, Z., Ye, T., Sun, Y., Ji, G., Shido, K., Chen, Y., Luo, L., Na, F., Li, X., Huang, Z.*, et al.* (2017). Targeting the vascular and perivascular niches as a regenerative therapy for lung and liver fibrosis. Sci Transl Med *9*.

Cartier, A., and Hla, T. (2019). Sphingosine 1-phosphate: Lipid signaling in pathology and therapy. Science *366*.

Chae, W.J., and Bothwell, A.L.M. (2018). Canonical and non-canonical Wnt signaling in immune cells. Trends Immunol *39*, 830-847.

Chen-Konak, L., Guetta-Shubin, Y., Yahav, H., Shay-Salit, A., Zilberman, M., Binah, O., and Resnick, N. (2003). Transcriptional and post-translation regulation of the Tie1 receptor by fluid shear stress changes in vascular endothelial cells. FASEB J *17*, 2121-2123.

Cheng, M., and Qin, G. (2012). Progenitor cell mobilization and recruitment: SDF-1, CXCR4, alpha4-integrin, and c-kit. Prog Mol Biol Transl Sci *111*, 243-264.

Chung, A.S., and Ferrara, N. (2011). Developmental and pathological angiogenesis. Annu Rev Cell Dev Biol *27*, 563-584.

Clevers, H., and Nusse, R. (2012). Wnt/beta-catenin signaling and disease. Cell *149*, 1192-1205.

Collu, G.M., Hidalgo-Sastre, A., and Brennan, K. (2014). Wnt-Notch signalling crosstalk in development and disease. Cell Mol Life Sci *71*, 3553-3567.

Cullen, M., Elzarrad, M.K., Seaman, S., Zudaire, E., Stevens, J., Yang, M.Y., Li, X., Chaudhary, A., Xu, L., Hilton, M.B.*, et al.* (2011). GPR124, an orphan G protein-coupled receptor, is required for CNS-specific vascularization and establishment of the blood-brain barrier. Proc Natl Acad Sci U S A *108*, 5759-5764.

Daly, C., Wong, V., Burova, E., Wei, Y., Zabski, S., Griffiths, J., Lai, K.M., Lin, H.C., Ioffe, E., Yancopoulos, G.D.*, et al.* (2004). Angiopoietin-1 modulates endothelial cell function and gene expression via the transcription factor FKHR (FOXO1). Genes Dev *18*, 1060-1071.

Davis, S., Aldrich, T.H., Jones, P.F., Acheson, A., Compton, D.L., Jain, V., Ryan, T.E., Bruno, J., Radziejewski, C., Maisonpierre, P.C.*, et al.* (1996). Isolation of angiopoietin-1, a ligand for the TIE2 receptor, by secretion-trap expression cloning. Cell *87*, 1161-1169.

Denisenko, E., Guo, B.B., Jones, M., Hou, R., de Kock, L., Lassmann, T., Poppe, D., Clement, O., Simmons, R.K., Lister, R.*, et al.* (2020). Systematic assessment of tissue dissociation and storage biases in single-cell and single-nucleus RNA-seq workflows. Genome Biol *21*, 130.

Dijksterhuis, J.P., Petersen, J., and Schulte, G. (2014). WNT/Frizzled signalling: receptor-ligand selectivity with focus on FZD-G protein signalling and its physiological relevance: IUPHAR Review 3. Br J Pharmacol *171*, 1195-1209.

Ding, B.S., Nolan, D.J., Butler, J.M., James, D., Babazadeh, A.O., Rosenwaks, Z., Mittal, V., Kobayashi, H., Shido, K., Lyden, D.*, et al.* (2010). Inductive angiocrine signals from sinusoidal endothelium are required for liver regeneration. Nature *468*, 310-315.

Dobie, R., Wilson-Kanamori, J.R., Henderson, B.E.P., Smith, J.R., Matchett, K.P., Portman, J.R., Wallenborg, K., Picelli, S., Zagorska, A., Pendem, S.V*., et al.* (2019). Single-cell transcriptomics uncovers zonation of function in the mesenchyme during liver fibrosis. Cell Rep *29*, 1832-1847 e1838.

Dobin, A., Davis, C.A., Schlesinger, F., Drenkow, J., Zaleski, C., Jha, S., Batut, P., Chaisson, M., and Gingeras, T.R. (2013). STAR: Ultrafast universal RNA-seq aligner. Bioinformatics *29*, 15-21.

Dreos, R., Ambrosini, G., Perier, R.C., and Bucher, P. (2015). The eukaryotic promoter database: Expansion of EPDnew and new promoter analysis tools. Nucleic Acids Res *43*, D92-96.

Dumont, D.J., Yamaguchi, T.P., Conlon, R.A., Rossant, J., and Breitman, M.L. (1992). Tek, a novel tyrosine kinase gene located on mouse chromosome 4, is expressed in endothelial cells and their presumptive precursors. Oncogene *7*, 1471-1480.

Ekman, N., Lymboussaki, A., Västrik, I., Sarvas, K., Kaipainen, A., and Alitalo, K. (1997). Bmx tyrosine kinase is specifically expressed in the endocardium and the endothelium of large arteries. Circulation *96*, 1729-1732.

Eraslan, B., Wang, D., Gusic, M., Prokisch, H., Hallstrom, B.M., Uhlen, M., Asplund, A., Ponten, F., Wieland, T., Hopf, T*., et al.* (2019). Quantification and discovery of sequence determinants of protein-per-mRNA amount in 29 human tissues. Mol Syst Biol *15*, e8513.

Evans, P.M., Chen, X., Zhang, W., and Liu, C. (2010). KLF4 interacts with beta-catenin/TCF4 and blocks p300/CBP recruitment by beta-catenin. Mol Cell Biol *30*, 372-381.

Fagiani, E., and Christofori, G. (2013). Angiopoietins in angiogenesis. Cancer Lett *328*, 18-26.

Fan, J., Wei, Q., Liao, J., Zou, Y., Song, D., Xiong, D., Ma, C., Hu, X., Qu, X., Chen, L*., et al.* (2017). Noncanonical Wnt signaling plays an important role in modulating canonical Wnt-regulated stemness, proliferation and terminal differentiation of hepatic progenitors. Oncotarget *8*, 27105-27119.

Fang, S., Wei, J., Pentinmikko, N., Leinonen, H., and Salven, P. (2012). Generation of functional blood vessels from a single c-kit+ adult vascular endothelial stem cell. PLoS Biol *10*, e1001407.

Farhan, M., Wang, H., Gaur, U., Little, P.J., Xu, J., and Zheng, W. (2017). FOXO signaling pathways as therapeutic targets in cancer. Int J Biol Sci *13*, 815-827.

Fausto, N., Campbell, J.S., and Riehle, K.J. (2006). Liver regeneration. Hepatology *43*, S45-53.

Fila, J., and Honys, D. (2012). Enrichment techniques employed in phosphoproteomics. Amino Acids *43*, 1025-1047.

Fornes, O., Castro-Mondragon, J.A., Khan, A., van der Lee, R., Zhang, X., Richmond, P.A., Modi, B.P., Correard, S., Gheorghe, M., Baranasic, D*., et al.* (2020). JASPAR 2020: Update of the open-access database of transcription factor binding profiles. Nucleic Acids Res *48*, D87-D92.

Forsburg, S.L. (2004). Eukaryotic MCM proteins: Beyond replication initiation. Microbiol Mol Biol Rev *68*, 109-131.

Franco, C.A., Jones, M.L., Bernabeu, M.O., Geudens, I., Mathivet, T., Rosa, A., Lopes, F.M., Lima, A.P., Ragab, A., Collins, R.T*., et al.* (2015). Dynamic endothelial cell rearrangements drive developmental vessel regression. PLoS Biol *13*, e1002125.

Gebhardt, R. (1992). Metabolic zonation of the liver: Regulation and implications for liver function. Pharmacol Ther *53*, 275-354.

Gordillo, M., Evans, T., and Gouon-Evans, V. (2015). Orchestrating liver development. Development *142*, 2094-2108.

Goumans, M.J., Liu, Z., and ten Dijke, P. (2009). TGF-beta signaling in vascular biology and dysfunction. Cell Res *19*, 116-127.

Hagemann-Jensen, M., Ziegenhain, C., Chen, P., Ramskold, D., Hendriks, G.J., Larsson, A.J.M., Faridani, O.R., and Sandberg, R. (2020). Single-cell RNA counting at allele and isoform resolution using Smart-seq3. Nat Biotechnol *38*, 708-714.

Halpern, K.B., Shenhav, R., Massalha, H., Toth, B., Egozi, A., Massasa, E.E., Medgalia, C., David, E., Giladi, A., Moor, A.E*., et al.* (2018). Paired-cell sequencing enables spatial gene expression mapping of liver endothelial cells. Nat Biotechnol *36*, 962-970.

Halpern, K.B., Shenhav, R., Matcovitch-Natan, O., Toth, B., Lemze, D., Golan, M., Massasa, E.E., Baydatch, S., Landen, S., Moor, A.E*., et al.* (2017). Single-cell spatial reconstruction reveals global division of labour in the mammalian liver. Nature *542*, 352-356.

Han, X., Wang, R., Zhou, Y., Fei, L., Sun, H., Lai, S., Saadatpour, A., Zhou, Z., Chen, H., Ye, F*., et al.* (2018). Mapping the mouse cell atlas by microwell-Seq. Cell *172*, 1091-1107 e1017.

Hao, H.X., Xie, Y., Zhang, Y., Charlat, O., Oster, E., Avello, M., Lei, H., Mickanin, C., Liu, D., Ruffner, H*., et al.* (2012). ZNRF3 promotes Wnt receptor turnover in an R-spondin-sensitive manner. Nature *485*, 195-200.

Hashiramoto, A., Sakai, C., Yoshida, K., Tsumiyama, K., Miura, Y., Shiozawa, K., Nose, M., Komai, K., and Shiozawa, S. (2007). Angiopoietin 1 directly induces destruction of the rheumatoid joint by cooperative, but independent, signaling via ERK/MAPK and phosphatidylinositol 3-kinase/Akt. Arthritis Rheum *56*, 2170-2179.

Hausser, J., Mayo, A., Keren, L., and Alon, U. (2019). Central dogma rates and the trade-off between precision and economy in gene expression. Nat Commun *10*, 68.

Hornbeck, P.V., Zhang, B., Murray, B., Kornhauser, J.M., Latham, V., and Skrzypek, E. (2015). PhosphoSitePlus, 2014: mutations, PTMs and recalibrations. Nucleic Acids Res *43*, D512-520.

Hsu, J.L., and Chen, S.H. (2016). Stable isotope dimethyl labelling for quantitative proteomics and beyond. Philos Trans A Math Phys Eng Sci *374*.

Hu, J., Srivastava, K., Wieland, M., Runge, A., Mogler, C., Besemfelder, E., Terhardt, D., Vogel, M.J., Cao, L., Korn, C*., et al.* (2014). Endothelial cell-derived angiopoietin-2 controls liver regeneration as a spatiotemporal rheostat. Science *343*, 416-419.

Huch, M., Dorrell, C., Boj, S.F., van Es, J.H., Li, V.S., van de Wetering, M., Sato, T., Hamer, K., Sasaki, N., Finegold, M.J*., et al.* (2013). In vitro expansion of single Lgr5+ liver stem cells induced by Wnt-driven regeneration. Nature *494*, 247-250.

Hughes, D.P., Marron, M.B., and Brindle, N.P. (2003). The antiinflammatory endothelial tyrosine kinase Tie2 interacts with a novel nuclear factor-kappaB inhibitor ABIN-2. Circ Res *92*, 630-636.

Huttlin, E.L., Jedrychowski, M.P., Elias, J.E., Goswami, T., Rad, R., Beausoleil, S.A., Villen, J., Haas, W., Sowa, M.E., and Gygi, S.P. (2010). A tissue-specific atlas of mouse protein phosphorylation and expression. Cell *143*, 1174-1189.

Huynh, J., Chand, A., Gough, D., and Ernst, M. (2019). Therapeutically exploiting STAT3 activity in cancer - using tissue repair as a road map. Nat Rev Cancer *19*, 82-96.

Jain, R.K. (2003). Molecular regulation of vessel maturation. Nat Med *9*, 685-693.

Jakab, M., and Augustin, H.G. (2020). Understanding angiodiversity: Insights from single cell biology. Development *147*.

Jha, S.K., Rauniyar, K., and Jeltsch, M. (2018). Key molecules in lymphatic development, function, and identification. Ann Anat *219*, 25-34.

Jin, Y.R., Han, X.H., Nishimori, K., Ben-Avraham, D., Oh, Y.J., Shim, J.W., and Yoon, J.K. (2020). Canonical Wnt/beta-catenin signaling activated by Wnt9b and Rspo2 cooperation regulates facial morphogenesis in mice. Front Cell Dev Biol *8*, 264.

Jin, Y.R., Han, X.H., Taketo, M.M., and Yoon, J.K. (2012). Wnt9b-dependent FGF signaling is crucial for outgrowth of the nasal and maxillary processes during upper jaw and lip development. Development *139*, 1821-1830.

Jones, N., Master, Z., Jones, J., Bouchard, D., Gunji, Y., Sasaki, H., Daly, R., Alitalo, K., and Dumont, D.J. (1999). Identification of Tek/Tie2 binding partners. Binding to a multifunctional docking site mediates cell survival and migration. J Biol Chem *274*, 30896-30905.

Kalucka, J., de Rooij, L., Goveia, J., Rohlenova, K., Dumas, S.J., Meta, E., Conchinha, N.V., Taverna, F., Teuwen, L.A., Veys, K.*, et al.* (2020). Single-cell transcriptome atlas of murine endothelial cells. Cell *180*, 764-779 e720.

Kanehisa, M., and Goto, S. (2000). KEGG: Kyoto encyclopedia of genes and genomes. Nucleic Acids Res *28*, 27-30.

Karner, C.M., Chirumamilla, R., Aoki, S., Igarashi, P., Wallingford, J.B., and Carroll, T.J. (2009). Wnt9b signaling regulates planar cell polarity and kidney tubule morphogenesis. Nat Genet *41*, 793-799.

Karner, C.M., Das, A., Ma, Z., Self, M., Chen, C., Lum, L., Oliver, G., and Carroll, T.J. (2011). Canonical Wnt9b signaling balances progenitor cell expansion and differentiation during kidney development. Development *138*, 1247-1257.

Khan, A.A., Sandhya, V.K., Singh, P., Parthasarathy, D., Kumar, A., Advani, J., Gattu, R., Ranjit, D.V., Vaidyanathan, R., Mathur, P.P.*, et al.* (2014). Signaling network map of endothelial TEK tyrosine kinase. J Signal Transduct *2014*, 173026.

Kim, M., Allen, B., Korhonen, E.A., Nitschke, M., Yang, H.W., Baluk, P., Saharinen, P., Alitalo, K., Daly, C., Thurston, G.*, et al.* (2016). Opposing actions of angiopoietin-2 on Tie2 signaling and FOXO1 activation. J Clin Invest *126*, 3511-3525.

Klaus, A., and Birchmeier, W. (2008). Wnt signalling and its impact on development and cancer. Nat Rev Cancer *8*, 387-398.

Koch, P.S., Olsavszky, V., Ulbrich, F., Sticht, C., Demory, A., Leibing, T., Henzler, T., Meyer, M., Zierow, J., Schneider, S.*, et al.* (2017). Angiocrine Bmp2 signaling in murine liver controls normal iron homeostasis. Blood *129*, 415-419.

Koo, B.K., Spit, M., Jordens, I., Low, T.Y., Stange, D.E., van de Wetering, M., van Es, J.H., Mohammed, S., Heck, A.J., Maurice, M.M.*, et al.* (2012). Tumour suppressor RNF43 is a stem-cell E3 ligase that induces endocytosis of Wnt receptors. Nature *488*, 665-669.

Kopp, H.G., Avecilla, S.T., Hooper, A.T., and Rafii, S. (2005). The bone marrow vascular niche: Home of HSC differentiation and mobilization. Physiology (Bethesda) *20*, 349-356.

Korhonen, E.A., Lampinen, A., Giri, H., Anisimov, A., Kim, M., Allen, B., Fang, S., D'Amico, G., Sipila, T.J., Lohela, M.*, et al.* (2016). Tie1 controls angiopoietin function in vascular remodeling and inflammation. J Clin Invest *126*, 3495-3510.

Korn, C., and Augustin, H.G. (2015). Mechanisms of vessel pruning and regression. Dev Cell *34*, 5-17.

Korpelainen, E.I., Karkkainen, M., Gunji, Y., Vikkula, M., and Alitalo, K. (1999). Endothelial receptor tyrosine kinases activate the STAT signaling pathway: Mutant Tie-2 causing venous malformations signals a distinct STAT activation response. Oncogene *18*, 1-8.

Lan, Y., Ryan, R.C., Zhang, Z., Bullard, S.A., Bush, J.O., Maltby, K.M., Lidral, A.C., and Jiang, R. (2006). Expression of Wnt9b and activation of canonical Wnt signaling during midfacial morphogenesis in mice. Dev Dyn *235*, 1448-1454.

Lazar, C., Gatto, L., Ferro, M., Bruley, C., and Burger, T. (2016). Accounting for the multiple natures of missing values in label-free quantitative proteomics data sets to compare imputation strategies. J Proteome Res *15*, 1116-1125.

Leibing, T., Geraud, C., Augustin, I., Boutros, M., Augustin, H.G., Okun, J.G., Langhans, C.D., Zierow, J., Wohlfeil, S.A., Olsavszky, V.*, et al.* (2018). Angiocrine Wnt signaling controls liver growth and metabolic maturation in mice. Hepatology *68*, 707-722.

Leppanen, V.M., Saharinen, P., and Alitalo, K. (2017). Structural basis of Tie2 activation and Tie2/Tie1 heterodimerization. Proc Natl Acad Sci U S A *114*, 4376-4381.

Letunic, I., and Bork, P. (2018). 20 years of the SMART protein domain annotation resource. Nucleic Acids Res *46*, D493-D496.

Liang, J., Shi, J., Wang, N., Zhao, H., and Sun, J. (2019). Tuning the protein phosphorylation by receptor type protein tyrosine phosphatase epsilon (PTPRE) in normal and cancer cells. J Cancer *10*, 105-111.

Liao, Y., Smyth, G.K., and Shi, W. (2014). FeatureCounts: an efficient general purpose program for assigning sequence reads to genomic features. Bioinformatics *30*, 923-930.

Lin, S., Nascimento, E.M., Gajera, C.R., Chen, L., Neuhofer, P., Garbuzov, A., Wang, S., and Artandi, S.E. (2018). Distributed hepatocytes expressing telomerase repopulate the liver in homeostasis and injury. Nature *556*, 244-248.

Liu, Y., Beyer, A., and Aebersold, R. (2016). On the dependency of cellular protein levels on mRNA abundance. Cell *165*, 535-550.

Locard-Paulet, M., Lim, L., Veluscek, G., McMahon, K., Sinclair, J., van Weverwijk, A., Worboys, J.D., Yuan, Y., Isacke, C.M., and Jorgensen, C. (2016). Phosphoproteomic analysis of interacting tumor and endothelial cells identifies regulatory mechanisms of transendothelial migration. Sci Signal *9*, ra15.

Lorenz, L., Axnick, J., Buschmann, T., Henning, C., Urner, S., Fang, S., Nurmi, H., Eichhorst, N., Holtmeier, R., Bodis, K*., et al.* (2018). Mechanosensing by beta1 integrin induces angiocrine signals for liver growth and survival. Nature *562*, 128-132.

Mammoto, A., and Mammoto, T. (2019). Vascular niche in lung alveolar development, homeostasis, and regeneration. Front Bioeng Biotechnol *7*, 318.

Manning, G., Whyte, D.B., Martinez, R., Hunter, T., and Sudarsanam, S. (2002). The protein kinase complement of the human genome. Science *298*, 1912-1934.

Marron, M.B., Singh, H., Tahir, T.A., Kavumkal, J., Kim, H.Z., Koh, G.Y., and Brindle, N.P. (2007). Regulated proteolytic processing of Tie1 modulates ligand responsiveness of the receptor-tyrosine kinase Tie2. J Biol Chem *282*, 30509-30517.

Martin, M. (2011). Cutadapt removes adapter sequences from high-throughput sequencing reads. EMBnetjournal *v. 17, n. 1, p. pp. 10-12*.

Marx, V. (2019). A dream of single-cell proteomics. Nat Methods *16*, 809-812.

McCuskey, R.S. (2014). Liver vasculature and microvasculature. In: Encyclopedia of medical immunology: autoimmune diseases, I.R. Mackay, N.R. Rose, B. Diamond, and A. Davidson, eds. (New York, NY: Springer New York), pp. 659-665.

Mederacke, I., Dapito, D.H., Affo, S., Uchinami, H., and Schwabe, R.F. (2015). High-yield and high-purity isolation of hepatic stellate cells from normal and fibrotic mouse livers. Nat Protoc *10*, 305-315.

Meijer, L.A., Zhou, H., Chan, O.Y., Altelaar, A.F., Hennrich, M.L., Mohammed, S., Bos, J.L., and Heck, A.J. (2013). Quantitative global phosphoproteomics of human umbilical vein endothelial cells after activation of the Rap signaling pathway. Mol Biosyst *9*, 732-749.

Mergner, J., Frejno, M., List, M., Papacek, M., Chen, X., Chaudhary, A., Samaras, P., Richter, S., Shikata, H., Messerer, M*., et al.* (2020). Mass-spectrometry-based draft of the Arabidopsis proteome. Nature *579*, 409-414.

Metz, K.S., Deoudes, E.M., Berginski, M.E., Jimenez-Ruiz, I., Aksoy, B.A., Hammerbacher, J., Gomez, S.M., and Phanstiel, D.H. (2018). Coral: Clear and customizable visualization of human kinome data. Cell Syst *7*, 347-350 e341.

Min, A., Deoudes, E., Bond, M.L., Davis, E.S., and Phanstiel, D.H. (2019). CoralP: Flexible visualization of the human phosphatome. J Open Source Softw *4*.

Mitchell, C., and Willenbring, H. (2008). A reproducible and well-tolerated method for 2/3 partial hepatectomy in mice. Nat Protoc *3*, 1167-1170.

Mitchell, C., and Willenbring, H. (2014). Addendum: A reproducible and well-tolerated method for 2/3 partial hepatectomy in mice. Nat Protoc *9*.

Monga, S.P., Pediaditakis, P., Mule, K., Stolz, D.B., and Michalopoulos, G.K. (2001). Changes in WNT/beta-catenin pathway during regulated growth in rat liver regeneration. Hepatology *33*, 1098-1109.

Moore, J.O., Lemmon, M.A., and Ferguson, K.M. (2017). Dimerization of Tie2 mediated by its membrane-proximal FNIII domains. Proc Natl Acad Sci U S A *114*, 4382-4387.

Morse, M.A., Sun, W., Kim, R., He, A.R., Abada, P.B., Mynderse, M., and Finn, R.S. (2019). The role of angiogenesis in hepatocellular carcinoma. Clin Cancer Res *25*, 912-920.

Moscovitz, J.E., and Aleksunes, L.M. (2013). Establishment of metabolism and transport pathways in the rodent and human fetal liver. Int J Mol Sci *14*, 23801-23827.

Needham, E.J., Parker, B.L., Burykin, T., James, D.E., and Humphrey, S.J. (2019). Illuminating the dark phosphoproteome. Sci Signal *12*.

Neves, H., and Kwok, H.F. (2017). In sickness and in health: The many roles of the minichromosome maintenance proteins. Biochim Biophys Acta Rev Cancer *1868*, 295-308.

Niklason, L., and Dai, G. (2018). Arterial venous differentiation for vascular bioengineering. Annu Rev Biomed Eng *20*, 431-447.

Nusse, R., Fuerer, C., Ching, W., Harnish, K., Logan, C., Zeng, A., ten Berge, D., and Kalani, Y. (2008). Wnt signaling and stem cell control. Cold Spring Harb Symp Quant Biol *73*, 59-66.

Ohtani, O., and Ohtani, Y. (2014). Hepatic lymphatic system. In: Encyclopedia of medical immunology: autoimmune diseases, I.R. Mackay, N.R. Rose, B. Diamond, and A. Davidson, eds. (New York, NY: Springer New York), pp. 459-465.

Oladipupo, S.S., Smith, C., Santeford, A., Park, C., Sene, A., Wiley, L.A., Osei-Owusu, P., Hsu, J., Zapata, N., Liu, F*., et al.* (2014). Endothelial cell FGF signaling is required for injury response but not for vascular homeostasis. Proc Natl Acad Sci U S A *111*, 13379-13384.

Ovejero, C., Cavard, C., Perianin, A., Hakvoort, T., Vermeulen, J., Godard, C., Fabre, M., Chafey, P., Suzuki, K., Romagnolo, B*., et al.* (2004). Identification of the leukocyte cell-derived chemotaxin 2 as a direct target gene of beta-catenin in the liver. Hepatology *40*, 167-176.

Paik, J.H., Kollipara, R., Chu, G., Ji, H., Xiao, Y., Ding, Z., Miao, L., Tothova, Z., Horner, J.W., Carrasco, D.R*., et al.* (2007). FoxOs are lineage-restricted redundant tumor suppressors and regulate endothelial cell homeostasis. Cell *128*, 309-323.

Park, C., Kim, T.M., and Malik, A.B. (2013). Transcriptional regulation of endothelial cell and vascular development. Circ Res *112*, 1380-1400.

Payankaulam, S., Raicu, A.M., and Arnosti, D.N. (2019). Transcriptional regulation of INSR, the insulin receptor gene. Genes (Basel) *10*.

Perez-Llamas, C., and Lopez-Bigas, N. (2011). Gitools: analysis and visualisation of genomic data using interactive heat-maps. PLoS One *6*, e19541.

Potel, C.M., Lin, M.H., Heck, A.J.R., and Lemeer, S. (2018). Defeating major contaminants in Fe(3+)-immobilized metal Ion affinity chromatography (IMAC) phosphopeptide enrichment. Mol Cell Proteomics *17*, 1028-1034.

Potente, M., and Makinen, T. (2017). Vascular heterogeneity and specialization in development and disease. Nat Rev Mol Cell Biol *18*, 477-494.

Preziosi, M., Okabe, H., Poddar, M., Singh, S., and Monga, S.P. (2018). Endothelial Wnts regulate beta-catenin signaling in murine liver zonation and regeneration: A sequel to the Wnt-Wnt situation. Hepatol Commun *2*, 845-860.

Pu, W., Zhang, H., Huang, X., Tian, X., He, L., Wang, Y., Zhang, L., Liu, Q., Li, Y., Li, Y.*, et al.* (2016). Mfsd2a+ hepatocytes repopulate the liver during injury and regeneration. Nat Commun *7*, 13369.

Puri, M.C., Rossant, J., Alitalo, K., Bernstein, A., and Partanen, J. (1995). The receptor tyrosine kinase TIE is required for integrity and survival of vascular endothelial cells. EMBO J *14*, 5884-5891.

Qiu, W., Evans, C.A., Landels, A., Pham, T.K., and Wright, P.C. (2020). Phosphopeptide enrichment for phosphoproteomic analysis - A tutorial and review of novel materials. Anal Chim Acta *1129*, 158-180.

Qu, X., Tompkins, K., Batts, L.E., Puri, M., and Baldwin, H.S. (2010). Abnormal embryonic lymphatic vessel development in Tie1 hypomorphic mice. Development *137*, 1285-1295.

Raslan, A.A., and Yoon, J.K. (2019). R-spondins: Multi-mode WNT signaling regulators in adult stem cells. Int J Biochem Cell Biol *106*, 26-34.

Rocha, A.S., Vidal, V., Mertz, M., Kendall, T.J., Charlet, A., Okamoto, H., and Schedl, A. (2015). The angiocrine factor rspondin3 is a key determinant of liver zonation. Cell Rep *13*, 1757-1764.

Russell, J.O., and Monga, S.P. (2018). Wnt/beta-catenin signaling in liver development, homeostasis, and pathobiology. Annu Rev Pathol *13*, 351-378.

Sabin, F.R. (1902). On the origin of the lymphatic system from the veins and the development of the lymph hearts and thoracic duct in the pig. American Journal of Anatomy *1*, 367-389.

Saharinen, P., Eklund, L., and Alitalo, K. (2017a). Therapeutic targeting of the angiopoietin-TIE pathway. Nat Rev Drug Discov *16*, 635-661.

Saharinen, P., Leppanen, V.M., and Alitalo, K. (2017b). SnapShot: Angiopoietins and their functions. Cell *171*, 724-724 e721.

Sato, T.N., Tozawa, Y., Deutsch, U., Wolburg-Buchholz, K., Fujiwara, Y., Gendron-Maguire, M., Gridley, T., Wolburg, H., Risau, W., and Qin, Y. (1995). Distinct roles of the receptor tyrosine kinases Tie-1 and Tie-2 in blood vessel formation. Nature *376*, 70-74.

Savant, S., La Porta, S., Budnik, A., Busch, K., Hu, J., Tisch, N., Korn, C., Valls, A.F., Benest, A.V., Terhardt, D.*, et al.* (2015). The orphan receptor Tie1 controls angiogenesis and vascular remodeling by differentially regulating Tie2 in tip and stalk cells. Cell Rep *12*, 1761-1773.

Schwanhausser, B., Busse, D., Li, N., Dittmar, G., Schuchhardt, J., Wolf, J., Chen, W., and Selbach, M. (2011). Global quantification of mammalian gene expression control. Nature *473*, 337-342.

Seegar, T.C., Eller, B., Tzvetkova-Robev, D., Kolev, M.V., Henderson, S.C., Nikolov, D.B., and Barton, W.A. (2010). Tie1-Tie2 interactions mediate functional differences between angiopoietin ligands. Mol Cell *37*, 643-655.

Semo, J., Nicenboim, J., and Yaniv, K. (2016). Development of the lymphatic system: new questions and paradigms. Development *143*, 924-935.

Sharma, K., D'Souza, R.C., Tyanova, S., Schaab, C., Wisniewski, J.R., Cox, J., and Mann, M. (2014). Ultradeep human phosphoproteome reveals a distinct regulatory nature of Tyr and Ser/Thr-based signaling. Cell Rep *8*, 1583-1594.

Shevchenko, A., Tomas, H., Havlis, J., Olsen, J.V., and Mann, M. (2006). In-gel digestion for mass spectrometric characterization of proteins and proteomes. Nat Protoc *1*, 2856-2860.

Si-Tayeb, K., Lemaigre, F.P., and Duncan, S.A. (2010). Organogenesis and development of the liver. Dev Cell *18*, 175-189.

Singhal, M., Gengenbacher, N., La Porta, S., Gehrs, S., Shi, J., Kamiyama, M., Bodenmiller, D.M., Fischl, A., Schieb, B., Besemfelder, E.*, et al.* (2020). Preclinical validation of a novel metastasis-inhibiting Tie1 function-blocking antibody. EMBO Mol Med *12*, e11164.

Souma, T., Thomson, B.R., Heinen, S., Carota, I.A., Yamaguchi, S., Onay, T., Liu, P., Ghosh, A.K., Li, C., Eremina, V.*, et al.* (2018). Context-dependent functions of angiopoietin 2 are determined by the endothelial phosphatase VEPTP. Proc Natl Acad Sci U S A *115*, 1298-1303.

Sugiyama, N., Imamura, H., and Ishihama, Y. (2019). Large-scale discovery of substrates of the human kinome. Sci Rep *9*, 10503.

Sweet, D.R., Fan, L., Hsieh, P.N., and Jain, M.K. (2018). Kruppel-like factors in vascular inflammation: Mechanistic insights and therapeutic potential. Front Cardiovasc Med *5*, 6.

Szklarczyk, D., Gable, A.L., Lyon, D., Junge, A., Wyder, S., Huerta-Cepas, J., Simonovic, M., Doncheva, N.T., Morris, J.H., Bork, P.*, et al.* (2019). STRING v11: protein-protein association networks with increased coverage, supporting functional discovery in genome-wide experimental datasets. Nucleic Acids Res *47*, D607-D613.

Tabula Muris, C., Overall, c., Logistical, c., Organ, c., processing, Library, p., sequencing, Computational data, a., Cell type, a., Writing, g.*, et al.* (2018). Single-cell transcriptomics of 20 mouse organs creates a Tabula Muris. Nature *562*, 367-372.

Tadros, A., Hughes, D.P., Dunmore, B.J., and Brindle, N.P. (2003). ABIN-2 protects endothelial cells from death and has a role in the antiapoptotic effect of angiopoietin-1. Blood *102*, 4407-4409.

Takeda, K., Kaisho, T., Yoshida, N., Takeda, J., Kishimoto, T., and Akira, S. (1998). Stat3 activation is responsible for IL-6-dependent T cell proliferation through preventing apoptosis: Generation and characterization of T cell-specific Stat3-deficient mice. J Immunol *161*, 4652-4660.

Tanaka, M., and Iwakiri, Y. (2016). The Hepatic lymphatic vascular system: Structure, function, markers, and lymphangiogenesis. Cell Mol Gastroenterol Hepatol *2*, 733-749.

Thompson, L.J., Jiang, J., Madamanchi, N., Runge, M.S., and Patterson, C. (2001). PTP-epsilon, a tyrosine phosphatase expressed in endothelium, negatively regulates endothelial cell proliferation. Am J Physiol Heart Circ Physiol *281*, H396-403.

Trutmann, M., and Sasse, D. (1994). The lymphatics of the liver. Anat Embryol (Berl) *190*, 201-209.

Tyanova, S., Temu, T., and Cox, J. (2016a). The MaxQuant computational platform for mass spectrometry-based shotgun proteomics. Nat Protoc *11*, 2301-2319.

Tyanova, S., Temu, T., Sinitcyn, P., Carlson, A., Hein, M.Y., Geiger, T., Mann, M., and Cox, J. (2016b). The Perseus computational platform for comprehensive analysis of (prote)omics data. Nat Methods *13*, 731-740.

Valle-Encinas, E., and Dale, T.C. (2020). Wnt ligand and receptor patterning in the liver. Curr Opin Cell Biol *62*, 17-25.

van Amerongen, R., and Berns, A. (2006). Knockout mouse models to study Wnt signal transduction. Trends Genet *22*, 678-689.

van de Wetering, M., Sancho, E., Verweij, C., de Lau, W., Oving, I., Hurlstone, A., van der Horn, K., Batlle, E., Coudreuse, D., Haramis, A.P.*, et al.* (2002). The beta-catenin/TCF-4 complex imposes a crypt progenitor phenotype on colorectal cancer cells. Cell *111*, 241-250.

van den Brink, S.C., Sage, F., Vertesy, A., Spanjaard, B., Peterson-Maduro, J., Baron, C.S., Robin, C., and van Oudenaarden, A. (2017). Single-cell sequencing reveals dissociation-induced gene expression in tissue subpopulations. Nat Methods *14*, 935-936.

Vickovic, S., Eraslan, G., Salmen, F., Klughammer, J., Stenbeck, L., Schapiro, D., Aijo, T., Bonneau, R., Bergenstrahle, L., Navarro, J.F.*, et al.* (2019). High-definition spatial transcriptomics for in situ tissue profiling. Nat Methods *16*, 987-990.

Villen, J., Beausoleil, S.A., Gerber, S.A., and Gygi, S.P. (2007). Large-scale phosphorylation analysis of mouse liver. Proc Natl Acad Sci U S A *104*, 1488-1493.

Walker, S.R., Nelson, E.A., Zou, L., Chaudhury, M., Signoretti, S., Richardson, A., and Frank, D.A. (2009). Reciprocal effects of STAT5 and STAT3 in breast cancer. Mol Cancer Res *7*, 966-976.

Wang, B., Zhao, L., Fish, M., Logan, C.Y., and Nusse, R. (2015). Self-renewing diploid Axin2(+) cells fuel homeostatic renewal of the liver. Nature *524*, 180-185.

Wang, Y., Chang, H., Rattner, A., and Nathans, J. (2016). Frizzled receptors in development and disease. Curr Top Dev Biol *117*, 113-139.

Wang, Y., Nakayama, M., Pitulescu, M.E., Schmidt, T.S., Bochenek, M.L., Sakakibara, A., Adams, S., Davy, A., Deutsch, U., Luthi, U.*, et al.* (2010). Ephrin-B2 controls VEGF-induced angiogenesis and lymphangiogenesis. Nature *465*, 483-486.

Weber, L.W., Boll, M., and Stampfl, A. (2003). Hepatotoxicity and mechanism of action of haloalkanes: carbon tetrachloride as a toxicological model. Crit Rev Toxicol *33*, 105-136.

Wickham, H. (2016). ggplot2: Elegant graphics for data analysis. Springer-Verlag New York *ISBN 978-3-319-24277-4, https://ggplot2.tidyverse.org*.

Willert, K., Brown, J.D., Danenberg, E., Duncan, A.W., Weissman, I.L., Reya, T., Yates, J.R., 3rd, and Nusse, R. (2003). Wnt proteins are lipid-modified and can act as stem cell growth factors. Nature *423*, 448-452.

Wojtowicz, W.M., Vielmetter, J., Fernandes, R.A., Siepe, D.H., Eastman, C.L., Chisholm, G.B., Cox, S., Klock, H., Anderson, P.W., Rue, S.M*., et al.* (2020). A human IgSF cell-surface interactome reveals a complex network of protein-protein interactions. Cell *182*, 1027-1043 e1017.

Xiong, X., Kuang, H., Ansari, S., Liu, T., Gong, J., Wang, S., Zhao, X.Y., Ji, Y., Li, C., Guo, L*., et al.* (2019). Landscape of intercellular crosstalk in healthy and NASH liver revealed by single-cell secretome gene analysis. Mol Cell *75*, 644-660 e645.

Xu, M., Xu, H.H., Lin, Y., Sun, X., Wang, L.J., Fang, Z.P., Su, X.H., Liang, X.J., Hu, Y., Liu, Z.M*., et al.* (2019). LECT2, a ligand for Tie1, plays a crucial role in liver fibrogenesis. Cell *178*, 1478-1492 e1420.

Yabkowitz, R., Meyer, S., Black, T., Elliott, G., Merewether, L.A., and Yamane, H.K. (1999). Inflammatory cytokines and vascular endothelial growth factor stimulate the release of soluble tie receptor from human endothelial cells via metalloprotease activation. Blood *93*, 1969-1979.

Yabkowitz, R., Meyer, S., Yanagihara, D., Brankow, D., Staley, T., Elliott, G., Hu, S., and Ratzkin, B. (1997). Regulation of tie receptor expression on human endothelial cells by protein kinase C-mediated release of soluble tie. Blood *90*, 706-715.

Yin, L.M., Schnoor, M., and Jun, C.D. (2020). Structural characteristics, binding partners and related diseases of the calponin homology (CH) domain. Front Cell Dev Biol *8*, 342.

Yousif, A., Drou, N., Rowe, J., Khalfan, M., and Gunsalus, K.C. (2020). NASQAR: a web-based platform for high-throughput sequencing data analysis and visualization. BMC Bioinformatics *21*, 267.

Yu, L., Tanwar, D.K., Penha, E.D.S., Wolf, Y.I., Koonin, E.V., and Basu, M.K. (2019). Grammar of protein domain architectures. Proc Natl Acad Sci U S A *116*, 3636-3645.

Zhang, N., Zhang, J., Shuai, L., Zha, L., He, M., Huang, Z., and Wang, Z. (2012). Kruppel-like factor 4 negatively regulates beta-catenin expression and inhibits the proliferation, invasion and metastasis of gastric cancer. Int J Oncol *40*, 2038-2048.

Zhou, Y., and Nathans, J. (2014). Gpr124 controls CNS angiogenesis and blood-brain barrier integrity by promoting ligand-specific canonical wnt signaling. Dev Cell *31*, 248-256.